Data-model comparisons of the tropical hydroclimate response to the 8.2 ka Event with an isotope-enabled climate model

Andrea L. Moore[1], Alyssa R. Atwood[1], and Raquel E. Pauly[1]

[1]Department of Earth, Ocean, and Atmospheric Science, Florida State University, Tallahassee, Florida, USA

Correspondence to: Andrea L. Moore (andilee.moore@gmail.com) and Alyssa R. Atwood (aatwood@fsu.edu)

Abstract. The 8.2 ka Event was a prominent climate anomaly that occurred approximately 8,200 years before present (8.2 ka) with implications for understanding the mechanisms and characteristics of abrupt climate change. We characterize the tropical hydroclimate response to the 8.2 ka Event based on a multiproxy compilation of 61 tropical hydroclimate records and assess the consistency between the proxy synthesis and simulated hydroclimate anomalies in a new 8.2 ka Event experiment performed using the isotope-enabled Community Earth System Model (iCESM1.2). We calculate the timing and duration of the hydroclimate anomalies in our proxy reconstruction using two event detection methods, including a new changepoint detection algorithm that explicitly accounts for age uncertainty. Using these methods, we find significant hydroclimate anomalies associated with the 8.2 ka Event in 30% of our proxy compilation, with a mean onset age of 8.28±0.12 ka (1σ), mean termination age of 8.11±0.09 ka (1σ), and mean duration of 152±70 years (1σ), comparing well with previous estimates. Notably, these anomalies are not hemispherically uniform, but display a rich regional structure with pronounced drying and/or isotopic enrichment across South and East Asia, the Arabian Peninsula, and in southern Central America, with wetter conditions and/or isotopic depletion in northeastern South America. In contrast, we find no signature of the 8.2 ka Event over the Maritime Continent.

The simulated hydroclimate response to the 8.2 ka Event generally agrees with the proxy reconstructions. In iCESM, the North Atlantic meltwater forcing causes a southward shift of the tropical rain bands ~~in the zonal mean~~, resulting in a generally drier Northern Hemisphere and wetter Southern Hemisphere, but with large regional variations in precipitation response, including~~amount and~~ the isotopic composition of precipitation. Over the oceans, the tropical rainbands shift south and precipitation $\delta^{18}O$ ($\delta^{18}O_p$) anomalies are generally consistent with the ~~"~~"amount effect," wherein the change in $\delta^{18}O_p$ is inversely correlated with the change in precipitation amount. However, the $\delta^{18}O_p$ anomalies are more decoupled from changes in precipitation amount over land. iCESM captures many of the regional hydroclimate responses observed in the reconstructions, including the large-scale isotopic enrichment pattern in $\delta^{18}O_p$ in South and East Asia and the Arabian Peninsula, drying and isotopic enrichment in $\delta^{18}O_p$ in southern Central America, isotopic depletion in parts of northeastern South America, and a muted hydroclimate response over the Maritime Continent. We decompose the simulated precipitation $\delta^{18}O$ response to identify the cause of~~mechanisms driving~~ these isotopic anomalies ~~in the tropics~~, finding that changes in amount-weighted $\delta^{18}O_p$ arise primarily from seasonal changes in $\delta^{18}O_p$ ~~the isotopic composition of precipitation~~ rather than seasonal changes

in precipitation amountseasonality. However, the mechanisms of the seasonal changes in $\delta^{18}O_p$ isotope anomalies vary regionally, with the local amount effect dominant in northeastern South America and the northeastern tropical Pacific; while changes in the isotopic composition of the water vapor (via changes in moisture source, circulation, and/or upstream rainout) seem t omoisture source, circulation patterns, and/or upstream rainout control the response in East Asia. In the Caribbean, the ; and the addition of isotopically depleted meltwater to the North Atlantic directly contributes to reduced, but isotopicallysubstantially depleted, wet season precipitation through the Caribbean. Overall, this study provides new insights into the tropical hydroclimate response to the 8.2 ka Event, emphasizing the importance of accounting for age uncertainty in proxy-based hydroclimate reconstructions and the value of using isotope-enabled model simulations for data-model intercomparison.

1 Introduction

The tropics play a fundamental role in Earth's climate systemvariability, acting as a heat source that drives global weather patterns via complex atmospheric teleconnections. A key component of the tropical climate system is the Intertropical Convergence Zone (ITCZ). From a zonal mean perspective, the ITCZ represents the ascending branch of the Hadley cell, characterized by converging low-level trade winds, ascent, and heavy precipitation near the equator. Regionally, ITCZs exist over the Atlantic and eastern Pacific Ocean, where strong sea surface temperature (SST) gradients drive convergence, and ascent inascent, and narrow, well-defined rainbands. DifferentDistinct processes govern the large-scale circulation and precipitation in other regions of the tropics like monsoon systems and the Indian Ocean. Throughout the tropics, rainfall patterns migrate on a seasonal basis, following the warmer hemisphere. The migrations are regionally variable, with the Atlantic and Pacific ITCZs migrating between 9°N and 2°N in boreal summer/fall and winter/spring, respectively, while rainfall over the Indian Ocean and adjacent land masses swings more dramatically between 20°N and 8°S (Schneider et al., 2014). These fluctuations drive distinct wet and dry seasons through many regions of the tropics, providing critical access to water for roughly 40% of Earth's population (State of the Tropics, 2021). As the tropics comprise some of the most densely populated areas on Earth, it is essential to understand how tropical precipitation patterns may change in the near future. However, there is currently no agreement across models on how tropical rainfall patterns the ITCZ and monsoons will change with continued greenhouse gas forcing (Biasutti et al., 2018; Geen et al., 2020), in part due to persistent biases in the representation of the tropical mean state in global climate models (Li & Xie, 2014). Therefore, validating the response of improving our understanding of how tropical rainfall patterns respond to external forcing is a key target in the climate modeling community.

Our ability to make robust predictions about the climate system is also limited by the relatively short instrumental record. Paleoclimate proxy records can provide important model benchmarks for extend the observational record beyond the instrumental era, illuminating the linkages between climate forcings and the response of the climate system. Such data are crucial for ground-truthing climate models to observations outside of the short period of instrumental data. Past direct

observational data. Examining past periods of abrupt climate change provide also provides important context for evaluating future climate risk, as we lack modern analogues of these events and cannot preclude their occurrencethe occurrence of such events in the future. Evidence from paleoclimate records (Arbuszewski et al., 2013; Koutavas & Lynch-Stieglitz, 2004; Rhodes et al., 2015) and model simulations of past climates (Chiang & Bitz, 2005; Roberts and Hopcroft, 2020) suggest that the location of the tropical rain bands may have shifted significantly and abruptly in the past (upwards of 7° latitude in certain regions) associated with changes in ice sheet extent and meltwater forcing (e.g., during Heinrich Events). The most recent such period of rapid, global climate reorganization occurred approximately 8,200 years before present day (the 8.2 ka Event; Alley et al., 1997) and is thought to have lasted over a period of 100 to 200 years based on oxygen isotopic data from Greenland ice cores and tropical speleothems (Morrill et al., 2013). This event occurred during the otherwise stable Holocene epoch (11,700 years ago to present) and is thought to have been driven by the discharge of ~1.63×10^5 km^3 of meltwater from proglacial Lakes Ojibway and Agassiz into the North Atlantic, triggering a large-scale salinity anomaly and resultant reduction in the strength of the Atlantic Meridional Overturning Circulation (AMOC; e.g., Barber et al., 1999; Ellison et al., 2006). The precise source, routing, and strength of the freshwater perturbation are still under discussion (e.g. Törnqvist and Hijma, 2012), ranging from an upper limit of 27.1×10^5 km^3 of freshwater released from the retreating Laurentide Ice Sheet (LIS) between 9 ka and 8 ka (Peltier 2004), to a smaller but more abrupt discharge of 5.3×10^5 km^3 between 8.31 ka and 8.18 ka (Li et al., 2012). Recent data-model comparisons from Aguiar et al. (2021) suggest that an additional 8.2×10^5 km^3 of freshwater may have flowed into the Labrador Sea after the collapse of the Hudson Bay due to the routing of river discharge over the western Canadian Plains (Carlson et al., 2009). Proxy data and dynamical theory (e.g., Kang et al., 2008; Kang et al., 2009; Schneider et al., 2014) link this event to widespread cooling of the Northern Hemisphere (1 to 6°C; e.g., Ellison et al., 2006; Kobashi et al., 2007) and an associated southward shift of tropical rainfall patterns, with hydroclimate anomalies lasting anywhere from decades to centuries (e.g., Rohling and Palike, 2005; Morrill et al., 2013).

Morrill et al. (2013) published the most recent multiproxy compilation of high-resolution paleoclimate data related to the 8.2 ka Event, incorporating 262 paleoclimate records from 114 global sites. Their synthesis demonstrated a regionally variable hydroclimate response to the 8.2 ka Event characterized by drying in Greenland, the Mediterranean, the Maritime Continent (Ayliffe et al., 2013; Chawchai et al., 2021), and across Asia (Wang et al., 2005; Dykoski et al., 2005; Cheng et al., 2009; Liu et al., 2013); while wetter conditions prevailed over northern Europe, Madagascar (Voarintsoa et al., 2019), and northeastern South America (Aguiar et al., 2020). Together, these data provide evidence for an anti-phased hemispheric precipitation response, with a strengthening of the South American summer monsoon (SASM), and a weakening of the Asian (AM) and East Asian summer monsoons (EASM).

Building on this work, Parker and Harrison (2022) used a statistical technique called breakpoint analysis to identify the timing, duration, and magnitude of the 8.2 ka Event in 73 high-resolution, globally distributed speleothem $\delta^{18}O$ records from the Speleothem Isotope Synthesis and Analysis database (SISALv2; Comas-Bru et al., 2020). They identified

significant isotopic excursions near 8.2 ka in over 70% of their records and determined a median duration of global hydroclimate anomalies of approximately 159 years. Parker and Harrison (2022) inferred several regionally coherent tropical hydroclimate anomalies from their synthesis, based on broad patterns of isotopic depletion across South America and southern Africa and isotopic enrichment in Asia, from which they inferred a weakening of Northern Hemisphere monsoons, strengthening of Southern Hemisphere monsoons, and a mean southward shift of the ITCZ as the most plausible mechanism for transmitting the effects of the 8.2 ka Event throughout the tropics.

There are several limitations to these studies which are addressed in the updated proxy compilation presented here. Chiefly, Morrill et al. (2013) rely upon an a priori event window in classifying the climate response to the 8.2 ka Event, and do not take radiometric age uncertainty of the proxy records into account. While Parker and Harrison (2022) consider the effects of age uncertainties on their compilation, they did not propagate these uncertainties through their breakpoint analyses. Further, tropical records comprise less than half of each compilation and since the publication of those studies, many new records have been generated in data-sparse regions that are key to understanding the complexities of tropical precipitation variability. Finally, recent studies (e.g., Atwood et al., 2020) have demonstrated significant regional variability in the tropical precipitation response to a variety of forcings, including North Atlantic meltwater events, calling into question the usefulness of invoking a southward shift in the zonal mean ITCZ as the primary mechanism driving hydroclimate changes in response to the 8.2 ka Event, as invoked in the reconstructions of Morrill et al. (2013) and Parker and Harrison (2022).

This study seeks to provide new insights into the tropical hydroclimate response to the 8.2 ka Event, by compiling an updated set of hydroclimate-sensitive proxy records complete with age model uncertainty and integrating them with new statistical tools to quantitatively evaluate how tropical rainfall patterns responded to this period of abrupt global climate change. We further assess how well the proxy reconstructions compare to a new isotope-enabled model simulation of the 8.2 ka Event. Such model simulations provide dynamical context to the sparse proxy data and, by tracking water isotopes through the hydrologic cycle, enable more direct comparisons between proxy and model data than conventional climate models. Such data-model comparisons facilitate improved understanding of the tropical hydroclimate response to abrupt AMOC disruptions and provide a necessary benchmark for climate models that are used in projections of future climate change.

2 Methods

2.1 Synthesis of published datasets

To assess the tropical hydroclimate response to the 8.2 ka Event, we developed an updated compilation of published, high-resolution, continuous, and well-dated proxy datasets. We collated records spanning 7 ka-10 ka, covering latitudes from 30°N to 30°S, and which are sensitive to some aspect of hydroclimate variability. Records were identified through in-depth literature review, searches of public data repositories (e.g., NOAA National Centers for Environmental

Information and World Data Center PANGAEA databases), and incorporation of previous compilations (e.g., Morrill et al., 2013). All records were reformatted into the Linked Paleo Data framework (LiPD; McKay and Emile-Geay, 2016) to facilitate analyses of age uncertainty and quantitative event detection.

To constrain the timing and duration of the abrupt hydroclimate anomaly associated with the 8.2 ka Event, the datasets in this compilation were screened to meet the following criteria: (i) data resolution of 50 years or better over the period of 7 ka-10 ka; (ii) based on hydroclimate-sensitive proxy data interpreted by authors as reflecting precipitation amount or intensity, the isotopic compositions of environmental water (including precipitation, lake water, and seawater), effective moisture, lake level, fluvial discharge, or sea surface salinity (SSS); and (iii) contain at least three radiometric dates over the 7 ka-10 ka interval. Emphasis was placed on collecting water isotope-based records to enable more direct comparison with isotope-enabled climate model simulations.

The compilation was organized into three categories based on the climate interpretation of the various proxy records (Fig. 1): proxies which reflect the isotopic composition of precipitation (P_{iso}), proxies which reflect effective moisture (EM; P-E), and proxies which reflect precipitation amount and/or intensity (P_{amt}). This categorization scheme enables more robust interpretations of the proxy records and facilitates data-model comparison as our understanding of water isotopes and their manifestations in paleoclimate archives continues to advance (Konecky et al., 2020).

2.2 Age model development

Published radiometric age data were used to develop age-depth model ensembles for each dataset using Bayesian methods. Where available (Table A1), we employed age ensembles developed by the Past Global Changes (PAGES) Speleothem Isotope Synthesis and Analysis (SISAL) working group from version 2 of their database (Comas-Bru et al., 2020). For records for which these age ensembles were not available due to lack of inclusion in the SISALv2 database or comprising a lacustrine or marine sediment archive, we developed age-depth models using the geoChronR package in R version 4.2.1 (McKay et al., 2021). All radiometric dates were obtained from the original publications and screened for updated age data where available. For records originating from the Northern Hemisphere tropics, radiometric dates were calibrated using the Northern Hemisphere calibration curve, IntCal20. Dates of records originating from the Southern Hemisphere tropics were calibrated using the Southern Hemisphere calibration curve, SHCal20. For each record, 1000 age-depth model iterations were run to generate a Markov Chain Monte Carlo (MCMC) age ensemble, which produces median age values and quantile age ranges, enabling the propagation of age-model uncertainties through subsequent analyses.

To reduce uncertainty arising from the differences in age modeling algorithms offered through geoChronR, we prioritized the use of BACON (Blaauw and Christen, 2011) across our records, including those in the SISALv2 database, where available. If a BACON age ensemble was not constructed for a SISALv2 dataset, we employed the Bchron (Haslett and Parnel, 2008) or copRA (Breitenbach et al., 2012) ensembles instead.

2.3 Detection of the 8.2 ka Event

Two event detection methods were used in this study, as detailed below. The start, end, and duration of hydroclimate anomalies associated with the 8.2 ka Event were calculated for all records where both methods detected events of the same sign. This was done to leverage the strengths of each detection method and provide a more robust reconstruction of the hydroclimate response to the 8.2 ka Event.

2.3.1 Modified Morrill method

For each record's published time series, we applied a modified version of the event detection methods described in Morrill et al. (2013) as a control for comparison with our actR results (hereafter referred to as MM; Fig. B1). Using 7.4 ka-7.9 ka as a reference period, we calculate the mean and the standard deviation over that interval. From there~~Then~~, we define the upper and lower bounds by the two-sigma level. We repeat this process for a second reference period from 8.5 ka-9.0 ka. We take the final upper and lower bounds as the most extreme values between the two reference periods. Then we use the 7.9 ka-8.5 ka period as the 8.2 ka Event detection window.

Over this period, any values which exceed the upper or lower bound are marked as the 8.2 ka Event, with the timing of the event defined by the ages of the proxy values that exceed those bounds. For an excursion to be considered part of the 8.2 ka Event, the excursions must last at least 10 years. If multiple events are detected within the 7.9 ka-8.5 ka window, they are combined into a single event if there are no more than three data points~~,~~ or thirty years~~,~~ separating the different excursions. This modification is necessary to account for the varying sampling resolutions present within and between several of the records in our compilation. If multiple events of differing signs are detected within the 8.2 ka Event window, the event with the largest z-score is chosen as the representative hydroclimate response. The magnitude of the event is defined by the largest absolute value z-score within the event detection period.

~~The MM method differs from the methodology presented in Morrill et al. (2013) in two additional aspects: (i) we do not perform the "leave one out" standard deviation calculation that Morrill et al. (2013) employed to account for noisy data and outliers in each reference window, and (ii), while Morrill et al. (2013) use a moving two-tailed z-test to define the duration of their detected events, we consider only the time between the initial and final anomalous data point in our calculation. We elected to simplify this method as it is primarily intended to supplement results using our actR methodology.~~

2.3.2 actR method

A second event detection method was used to account for age model uncertainties in the proxy records. Past studies (e.g., Morrill et al., 2013) employed statistical techniques to detect excursions in proxy records using the a priori assumption that the North Atlantic meltwater perturbation propagated globally at exactly 8.2 ka and lasted no more than 200 years. To better constrain the timing, duration, and magnitude of the 8.2 ka Event in this study, we employed an event detection algorithm based on the changepoint package in the newly developed Abrupt Change Toolkit in R (actR; McKay and Emile-

Geay, 2022). This algorithm detects abrupt shifts in the mean of a time series based on a prescribed number of age model ensembles (generated in geoChronR), the minimum length of a segment (in years) over which mean shifts in the time series are detected, a user-defined changepoint detection method, and a weighting penalty function (Fig. 2). A minimum segment length of 50 or 100 years was assigned for each record in the proxy compilation to minimize short-lived transitions in the noisy proxy records, with the assumption that the 8.2 ka Event signal in each of the records lasts at least 50 years. For all but one record in our compilation, the 100-year minimum segment length optimally captured the major shifts in the data sets while minimizing the detection of spurious short-lived shifts. The exception was the speleothem record of Cheng et al. (2009; PAD07; Fig. C5), for which it was necessary to reduce the minimum segment length to 50 years to capture the clear isotopic depletion near 8.2 ka that was otherwise missed.

Detected changepoints were summarized over 10-year-long windows. The Pruned Exact Linear Time (PELT; Killick et al., 2012) changepoint detection method was chosen for its computational efficiency and dynamic programming approach to accurately identify the location and number of changepoints in time series data. The Modified Bayesian Information Criterion (MBIC; Zhang and Siegmund, 2007) was chosen as the penalty weighting function to balance the goodness of fit of the model to the data with the complexity of the model and the number of changepoints. These methods effectively minimize the detection of spurious changepoints within each ensemble. Each time series ensemble was tested against a robust null hypothesis using surrogate proxy data generated by an isospectral noise model. By construction, the surrogate data have the same power spectrum as the original data, but phase scrambling destroys any autocorrelation that was present in the original time series. If autocorrelation is detected in a segment of the original time series ensemble, it fails the null hypothesis test, and any changepoint detected within that segment is excluded from the result. This test helps to ensure that the detected changepoints are statistically significant and not just the result of random variation. Both age and proxy data uncertainties are propagated through each ensemble, improving the robustness of the result. For each record, 1000 age model ensembles were generated and tested against 100 surrogate time series.

The actR event detection algorithm can be compromised by variable sampling resolution. Therefore, for records with highly variable resolution, we used the MM method to determine event onset, termination, and duration. This applies to only two records: the speleothem record from Dykoski et al. (2005; D4Dykoski, Fig. C7) and the speleothem record from Neff et al. (2001; H5; Fig. C10).

Two types of events were characterized based on the actR results. ‘Significant events’ are defined by the presence of two consecutive changepoints with $p < 0.05$ over the 7.9 ka-8.3 ka window ("start" and "end"). If more than two consecutive changepoints exist over that window, the two with the lowest p-values and highest probability are used. The difference between "start" and "end" dates is used to calculate event duration, which we assume to be between a minimum of 20 and a maximum of 300 years. The magnitude of "events" is determined by the greatest absolute value z-score in each record's median age ensemble time series between the actR-derived "start" and "end" dates, with interpretation based on the sign of the z-score corresponding to the interpretation direction of the original authors. ‘Tentative events’ are defined by the

presence of two consecutive changepoints with $p < 0.1$ over an extended 7.7 ka-8.5 ka window. Events lasting more than 300 years are removed from consideration. If more than two events are detected within that window, the event with the start date closer to 8.2 ka is chosen as the final 8.2 ka Event.

2.4 iCESM simulations

The National Center for Atmospheric Research's (NCAR) water isotope-enabled Community Earth System Model (iCESM1.2; Brady et al., 2019) is a state-of-the-art, fully coupled GCM designed to simulate water isotopes across all stages of the global hydroclimate cycle. It employs the CAM5.3 atmospheric model, with a gridded resolution of 1.9° latitude x 2.5° longitude and 29 vertical levels. Land processes are modeled by CLM4, at the same nominal 2° resolution. CLM is coupled to a River Transport Model which routes runoff from the land into oceans and/or marginal seas. Both the POP2 ocean model and the CICE sea ice model have a common grid size of 320×~~x~~384 with a nominal 1° resolution near the equator and in the North Atlantic. While iCESM faithfully captures the broad quantitative and qualitative features of precipitation isotopes, it is known to have a global bias toward depleted precipitation $\delta^{18}O$ ($\delta^{18}O_p$; median bias of -2.5‰; Brady et al., 2019).

We performed a new 8.2 ka Event meltwater-forced ("hosing") simulation and an early Holocene control simulation ("ctrl") using iCESM1.2. iCESM enables explicit tracking of water isotopes throughout the global water cycle, facilitating quantitative comparisons between model output and water isotope-based proxy records. These simulations followed the Paleoclimate Modeling Intercomparison Project 4-Coupled Model Intercomparison Project 6 (PMIP4-CMIP6) 8.2 ka simulation parameters (Otto-Bliesner et al., 2017), with two exceptions: (i~~1~~) the freshwater flux was applied across the entire northern North Atlantic in our simulations (instead of just in the Labrador Sea as in PMIP4) in order to limit the sensitivity of the subsequent AMOC and climate response to poorly resolved deepwater formation regions in the model, and (ii~~2~~) our hosing experiment branches from 9 ka boundary conditions (instead of 9.5 ka as in PMIP4), and thus uses slightly different orbital and GHG configurations from PMIP4. However, the impact of these marginally different boundary conditions is expected to be minimal.

For the 9 ka control simulation, the model was forced with prescribed greenhouse gas concentrations (CH_4 = 658.5 ppb, CO_2 = 260.2 ppm, and N_2O = 255 ppb), orbital configurations (eccentricity = 0.019524°, obliquity = 24.2030°, and longitude of perihelion = 99.228°), and a reconstruction of the ice sheet extent (Peltier et al., 2015) representative of conditions at 9 ka. The orbital configuration is characterized by larger obliquity, slightly higher eccentricity, and a change in the longitude of perihelion relative to present day that resulted in increased seasonality of insolation in the Northern Hemisphere (Wu et al., 2018; Hu et al., 2019). These factors produced warmer Northern Hemisphere summers, especially in mid to high latitudes, which promoted the retreat of the remnant Laurentide Ice Sheet (LIS) (Otto-Bliesner et al., 2017 and references therein). The control simulation ("ctrl") was initialized from an earlier 400-year-long 9 ka simulation and run for 100 model years using these parameters.

The 8.2 ka Event simulation ("hose") was branched from year 100 of the 9 ka control run. Initially, a simulated 2.5Sv meltwater flux (meltwater $\delta^{18}O$ = -30‰; Zhu et al., 2017) was applied across the northern North Atlantic Ocean (50–70°N) for 1 year, followed by 0.13Sv flux for 99 years to approximate the abrupt drainage of Lakes Agassiz and Ojibway and eventual collapse of the LIS at Hudson Bay (Otto-Bliesner et al., 2017). Monthly surface air temperature, precipitation amount, and $\delta^{18}O_p$ variables were extracted from each simulation for analysis. To isolate the global response to the simulated 8.2 ka Event, yearly time series of temperature (°C), precipitation amount (mm day~~d~~$^{-1}$), and amount-weighted $\delta^{18}O_p$ (‰) were obtained. Anomalies for each variable were calculated by subtracting the final 50 years of the "ctrl" simulation from the final 50 years of the "hose" simulation.

2.5 Decomposition of changes in precipitation $\delta^{18}O$

We decomposed the changes in amount-weighted $\delta^{18}O_p$ into two components following Liu and Battisti (2015): (i) those resulting from changes in the amount of monthly precipitation and (ii) those resulting from changes ~~to assess whether the changes arise from variations~~ in the monthly isotopic composition of precipitation. The latter component may be due to changes in local precipitation intensity and/or to ~~or~~ changes in the isotopic composition of the water vapor which forms the condensate~~seasonality of precipitation (i.e., changes in monthly precipitation amount)~~. The difference in amount-weighted $\delta^{18}O_p$ between the hosing and control simulations is equal to:

$$\delta^{18}O_{p,hose} - \delta^{18}O_{p,ctrl} = \frac{\sum_j \delta^{18}O_{j,hose} P_{j,hose}}{\sum_j P_{j,hose}} - \frac{\sum_j \delta^{18}O_{j,ctrl} P_{j,ctrl}}{\sum_j P_{j,ctrl}}, \quad (1)$$

where $\delta^{18}O_j$ is the monthly isotopic composition of precipitation and P_j is the monthly precipitation rate (in mm day^{-1}), with j representing the values for each sequential month over the full simulation period rather than monthly climatology. The importance of changes in precipitation seasonality to changes in $\delta^{18}O_p$ is then given by:

$$\frac{\sum_j \delta^{18}O_{j,ctrl} P_{j,hose}}{\sum_j P_{j,hose}} - \frac{\sum_j \delta^{18}O_{j,ctrl} P_{j,ctrl}}{\sum_j P_{j,ctrl}} \quad (2)$$

and the importance of changes in the monthly isotopic composition of precipitation to changes in total $\delta^{18}O_p$ is given by:

$$\frac{\sum_j \delta^{18}O_{j,hose} P_{j,ctrl}}{\sum_j P_{j,ctrl}} - \frac{\sum_j \delta^{18}O_{j,ctrl} P_{j,ctrl}}{\sum_j P_{j,ctrl}} \quad (3)$$

$$\frac{\sum_j \delta^{18}O_{j,ctrl} P_{j,hose}}{\sum_j P_{j,hose}} - \frac{\sum_j \delta^{18}O_{j,ctrl} P_{j,ctrl}}{\sum_j P_{j,ctrl}}, \quad (2)$$

and the importance of changes in the monthly isotopic composition of precipitation to changes in total $\delta^{18}O_p$ is given by:

$$\frac{\sum_j \delta^{18}O_{j,hose} P_{j,ctrl}}{\sum_j P_{j,ctrl}} - \frac{\sum_j \delta^{18}O_{j,ctrl} P_{j,ctrl}}{\sum_j P_{j,ctrl}}. \quad (3)$$

Note that Eqs. (2) and (3) do not sum to the total change in $\delta^{18}O_p$ due to nonlinearity in the definition of $\delta^{18}O_p$.

3 Results

3.1 Data compilation

This study compiled 61 tropical hydroclimate proxy records covering 17 IPCC-designated climate regions (Fig. B2; Iturbide et al., 2020). Compared to Morrill et al. (2013), our compilation substantially improves hydroclimate proxy data coverage across the Caribbean, Central America, South America, South and East Asia, and the Maritime Continent. The compilation comprises 42 speleothem records (~69%), 14 lacustrine records (~23%), and 5 marine records (~8%; Table 2). When categorized by hydroclimate interpretation, the compilation includes 43 P_{iso} records (70.5%), 11 EM records (18%), and 7 P_{amt} records (11.5%; Fig. 1; Table 2). For the purpose of this study, records which fully meet all inclusion criteria are designated as Tier 1 records (n = 50, 82%), forming the basis for the data-model intercomparison. Records which fail to meet either the minimum paleodata resolution or radiometric date requirements are classified as Tier 2 records and are included as supporting datasets (n = 10, 16%). One record (MWS1; Dutt et al., 2015) failed to meet both requirements, thus it is designated as a Tier 3 record, and has been excluded from further analysis.

3.2 Timing, magnitude, and duration of the 8.2 ka Event in the proxy compilation

The approximate start, end, and duration of hydroclimate anomalies associated with the 8.2 ka event were calculated for all records where both our MM and actR event detection methods detected events of the same sign (wetter, drier, or no change). This approach provides a more robust reconstruction of the hydroclimate response to the 8.2 ka Event than either method would achieve in isolation. This final set of records comprises 30 of the 61 records (49%) in our compilation exhibited such agreement between the two detection methods. The remaining 31 records displayed disagreement between the two detection methods and were thus excluded from further analysis.

Of the 30 records that exhibit agreement between the two detection methods, significant hydroclimate events were detected in 18 records (34% of all Tier 1 and 10% of all Tier 2 records), with the remaining 12 records showing no event in either detection method (14% of all Tier 1 records and 50% of all Tier 2 records). The lower event detection frequency in

Tier 2 compared to Tier 1 records highlights the importance of using high resolution records with good age constraints for the detection of abrupt climate events, as the threshold for event detection is rarely exceeded in records that are low resolution and/or have large age uncertainty (i.e., Tier 2 records).

Globally, detected hydroclimate anomalies had average onset at 8.28 ka, average termination at 8.13 ka, and average duration of 152 years. The longest events occurred in the Gulf of Mexico sedimentary foraminifera $\delta^{18}O$ record (LoDico et al., 2006; MD022550; Fig. C4; 289 years) and the Chongqing, China speleothem record (Yang et al., 2019; HF01; Fig. C11; 259 years). The Chinese lacustrine magnetic susceptibility record of Hillman et al. (2021; F14; Fig. C8) has the earliest event onset age of 8.49 ka, with a termination at 8.34 ka, for a total duration of 152 years, while the Chinese speleothem record of Dykoski et al. (2005; D4Dykoski; Fig. C7) has the latest event onset age at roughly 8.11 ka, terminating near 8.04 ka, for an event duration of 62 years.

In the final set of 30 records (that agree on the sign of the event between the MM and actR methods), drier and/or isotopically enriched events were detected in 13 of those 30 records (Table 5), including six records from East Asia (Fig. 5), with the largest events (+3.0σ, +5.8σ) detected in the speleothem record of Yang et al. (2019; HF01; Fig. C11) and the magnetic susceptibility record of Hillman et al. (2021; F14; Fig. C8). Similarly, drying/isotopic enrichment was seen in three speleothem records from the Arabian Peninsula, with the largest event (+3.5σ) detected in the record of Cheng et al. (2009; H14; Fig. C9) between 8.08 ka and 8.21 ka. The two speleothem records of Chawchai et al. (2021) from Klang Cave, Thailand (TK07, Fig. C15; TK20, Fig. C16) showed similarly high levels of isotopic enrichment (+3.1σ and +2.5σ) between approximately 8.16 ka and 8.30 ka. Two large drying/enrichment events were also detected in central America, including a positive isotopic excursion of +3.4σ in the Costa Rican speleothem record of Lachniet et al. (2004; V1; Fig. C17) from 8.05 ka and 8.19 ka and a negative excursion (-4.0σ) in titanium content (indicative of a drying event) in the Guatemalan lake sediment record of Duarte et al. (2021; Core5LI; Fig. C6) from 8.09 ka and 8.16 ka, suggesting a regional hydroclimate response to the 8.2 ka Event in southern Central America, south of the Yucatan Peninsula (Fig. 7).

Wetter and/or isotopically depleted events were detected in five of the 30 records in the final compilation. Namely, the Madagascar speleothem records of Voarintsoa et al. (2017; ANJB2; Fig. C2) and Duan et al. (2021; ABC1; Fig. C1) showed negative isotopic excursions of -3.0σ and -2.5σ, respectively, while the two Brazilian speleothem records from Lapa Grande Cave (Strikis et al., 2011; LG11; Fig. C3) and Padre Cave (Cheng et al., 2009; PAD07; Fig. C5) exhibited negative isotopic excursions of -2.9σ and -2.7σ, respectively (Table 5). In addition, a large isotopic depletion event (-3.8σ) was detected in the foraminifera $\delta^{18}O$ record from the Gulf of Mexico (LoDico et al., 2006; MD022550; Fig. C4).

We found no significant hydroclimate response in the remaining 12 records of our compilation, with both the MM and actR event detection methods in agreement that no event occurred. This category included three lake sediment records from the Yucatan Peninsula (Fig. 7c and Fig. B7c; LC1 [Hodell et al., 1995; Fig. C25], Curtis6VII93 [Curtis et al., 1998; Fig. C20], LagoPuertoArturo [Wahl et al., 2014; Fig. C24]), two speleothem records from Southeast Asia/the Maritime Continent (Fig. 8 and Fig. B8; KMA [Berkelhammer et al., 2012; Fig. C23], SSC01 [Carolin et al., 2016; Fig. C29]), and

two speleothem records from Brazil (Fig. 6 and Fig. B6; RN1 [Cruz et al., 2009; Fig. C28], TM6 [Ward et al., 2019; Fig. C30]).

3.3 Regional coherency of the reconstructed hydroclimate changes

The spatial pattern of reconstructed hydroclimate anomalies shows substantial regional coherency (Fig. 3), though it does not strictly conform to the hemispheric dipole pattern associated with the 8.2 ka Event (i.e., a generally drier/isotopically enriched Northern Hemisphere and wetter/isotopically depleted Southern Hemisphere). Both the MM and actR event detection methods indicate prominent drying/enrichment across East and Southeast Asia, as well as the Arabian Peninsula. These dry conditions are interspersed with areas of no change in parts of the Maritime Continent and eastern India/Tibetan Plateau. No robust signatures of the 8.2 ka Event are observed over the Maritime Continent. Central and South America display more of a hemispheric dipole pattern, with dry/enrichment events occurring north of the equator in Costa Rica and Guatemala, contrasting with wet/depletion events south of the equator in central/eastern Brazil. However, there are also regions in northern and central Brazil that exhibit no hydroclimate response. The proxy records thus present a far more complex, regionally specific hydroclimate response to the 8.2 ka Event than a simple hemispheric dipole pattern.

In several regions (including East Asia, Fig. 5; and northeastern South America, Fig. 6), records with no detected change are located near records with clear event signals. These regional differences could arise from several factors, including localized hydroclimate responses to the event, age uncertainty, and proxy interpretation uncertainties. For example, speleothem $\delta^{18}O$ records have been interpreted as representing a range of different climate processes, often within the same region, including changes in regional precipitation amount, monsoon strength, moisture source location, upstream rainout, seasonal frontal shifts, and temperature (e.g. Hu et al., 2019), reflecting the complexity of processes that impact $\delta^{18}O_p$ and speleothem $\delta^{18}O$. Because of the inherently regional nature of rainfall patterns and the uncertainties in the proxy records, we focus our interpretation on regional hydroclimate signals that are supported by multiple records, often across different aspects of hydroclimate. In this way, we focus on the most robust aspects of the tropical hydroclimate response to the 8.2 ka Event.

3.4 Global signature of the 8.2 ka Event in iCESM

We now compare these reconstructed hydroclimate patterns to those simulated by iCESM under 8.2 ka meltwater forcing. The surface temperature response in iCESM exhibits the characteristic "bipolar seesaw" pattern (i.e., a colder northern hemisphere and warmer southern hemisphere, most pronounced in the Atlantic Ocean), consistent with reduced northward heat transport by AMOC (Fig. B3). Anomalously cool surface temperatures, reaching as low as -20°C where the freshwater forcing was applied, stretch across the northern North Atlantic Ocean, southward along the western coasts of Europe and North Africa, and into the tropical Atlantic via the North Atlantic Subtropical Gyre. Surface air temperatures across the Southern Hemisphere show a positive anomaly of up to 3°C, with the largest warming occurring in the South

Atlantic. Over the continents, surface air temperatures cool in all regions except localized parts of northern South America, West Africa, and the southernmost regions of South America and Australia.

Accompanying these temperature anomalies are notable anomalies in precipitation amount, $\delta^{18}O_p$, and effective moisture (Fig. 4). Precipitation decreases while effective moisture increases throughout much of the North Atlantic, with the responses most pronounced in the regions with greatest cooling. The increase in effective moisture in this region indicates that the evaporation reduction outpaces the precipitation reduction (Fig. 4c). In the tropics, the largest precipitation anomalies appear in the tropical Pacific and Atlantic basins, with a southward shift of the Pacific and Atlantic ITCZs occurring in response to the freshwater forcing (Fig. 4b). These shifts are characterized by a weakening of the northern extent of the ITCZs and an enhancement of the southern extent. The most pronounced drying occurs over central America and the northeastern tropical Pacific, including Costa Rica and Panama, while the largest wet anomalies occur across the southern tropical Pacific. A notable hemispheric dry/wet dipole pattern is also observed in the tropical Atlantic, extending over northeastern South America. This pattern is less pronounced but still present over the tropical Indian Ocean and Africa. In contrast, no such dipole occurs over the western Pacific or Maritime Continent. Notably, the simulated pattern in $\delta^{18}O_p$ in iCESM under 8.2 ka meltwater forcing is remarkably similar to that in GISS ModelE-R under Heinrich forcing (Fig. 4a), indicating a robust inter-model response in $\delta^{18}O_p$ to North Atlantic meltwater forcing (aside from Africa and Antarctica, where the inter-model agreement breaks down).

These temperature and precipitation anomalies project strongly onto the amount-weighted $\delta^{18}O_p$ values (Fig. 4a). The greatest $\delta^{18}O_p$ anomalies occur in the northern reaches of the North Atlantic Ocean, reaching up to -8‰ in association with the strong regional cooling of the North Atlantic, as well as the addition of highly depleted (-30‰) meltwater to the surface ocean of the "hosing" site, and subsequent evaporation and rainout. In the tropics, $\delta^{18}O_p$ anomalies closely follow the changes in precipitation amount over the tropical Atlantic and central/eastern Pacific Oceans, with negative $\delta^{18}O_p$ anomalies south of the equator and positive $\delta^{18}O_p$ anomalies north of the equator. A pronounced dipole pattern is also evident over northern South America, where anomalously increased (decreased) rainfall amounts correspond to negative (positive) $\delta^{18}O_p$ anomalies in the southeastern (northwestern) region of South America. In the Middle East, India, Tibetan Plateau, and parts of Southeast Asia, modest drying is accompanied by pronounced positive $\delta^{18}O_p$ anomalies. However, not all regions are well described by the amount effect. In the Caribbean and Central America, there is a positive relationship between $\delta^{18}O_p$ and precipitation amount, characterized by strong drying and isotopic depletion (associated with the strong upwind cooling and meltwater addition in the North Atlantic). There also appears to be no clear relationship between precipitation amount and $\delta^{18}O_p$ anomalies over Africa, East Asia, the Western Pacific, and Maritime Continent.

3.4.1 Mechanisms driving the response of precipitation $\delta^{18}O$ to North Atlantic freshwater forcing

To assess whether the simulated hydroclimate changes are due to changes in the seasonality of $\delta^{18}O_p$ or changes in the seasonality of precipitation amount, we decomposed the changes in amount-weighted $\delta^{18}O_p$ following Liu and Battisti

(2015; Fig. 9). In East Asia, the change in amount-weighted $\delta^{18}O_p$, including the east-west dipole pattern with isotopic depletion off the coast of China into the North Pacific and isotopic enrichment inland, is driven by the seasonal changes in the isotopic composition of precipitation (Fig. 10b,c). Under meltwater forcing, $\delta^{18}O_p$ inland is more enriched throughout the year, particularly in the dry season from December to April (Fig. 12c). While $\delta^{18}O_p$ off the coast is more depleted throughout the year, particularly during the wet season from June to November (Fig. 12d). Consistent with previous studies on Heinrich events, these results suggest that the meltwater-induced enrichment in Chinese speleothem $\delta^{18}O$ records is not driven by changes in local precipitation and/or the strength of the EASM, but rather driven by changes in moisture source, circulation, and/or upstream rainout (Chiang et al., 2020; Pausata et al., 2011, Lewis et al., 2010). That the largest changes in $\delta^{18}O_p$ over China occur during the winter season is consistent with the results from Lewis et al. (2010), which found that increased moisture provenance in the Bay of Bengal during winter yielded enriched $\delta^{18}O_p$ over China during Heinrich events. The large zonal asymmetry observed in the $\delta^{18}O_p$ response to meltwater forcing between China and the North Atlantic was also identified in the Heinrich simulations of Lewis et al. (2010) and Pausata et al. (2011).

In northeastern South America and southern Central America, the change in amount-weighted $\delta^{18}O_p$ is also dominated by the seasonal changes in $\delta^{18}O_p$ and not the seasonality of precipitation (Fig. 10e-f,h-i), however the mechanisms of the response seem to differ from those in East Asia. In northeastern Brazil, precipitation increases under meltwater forcing and becomes more isotopically depleted during the wet season from December to July (Fig. 11c,d). These changes are consistent with a Type-1 control on $\delta^{18}O_p$ (Lewis et al., 2010), wherein the local amount effect dominates the $\delta^{18}O_p$ response. In southern Central America, the change in amount-weighted $\delta^{18}O_p$ is characterized by a distinct SW-NE dipole with isotopic enrichment in the northeastern tropical Pacific and over Panama and isotopic depletion over the Caribbean and the remainder of southern Central America. This pattern is also driven by the seasonal changes in $\delta^{18}O_p$ under meltwater forcing (Fig. 10h,i). In the northeastern tropical Pacific, wet season precipitation is substantially weakened and isotopically enriched (Fig. 13a,c), consistent with a Type-1 site (Lewis et al., 2010), wherein the local amount effect dominates the $\delta^{18}O_p$ response. Past studies on the hydroclimate response to Heinrich events have shown that regional precipitation changes in northeastern Brazil and the eastern Pacific are associated with a southward shift of the Atlantic and northeastern tropical Pacific ITCZs (Lewis et al., 2010; Roberts et al., 2020; Atwood et al., 2020). However, the $\delta^{18}O_p$ response over the Caribbean and southern Central America is notably different. In this region, the wet season precipitation decreases under hosing, essentially eliminating the wet season, while the precipitation becomes substantially more isotopically depleted throughout the year (Fig. 13b,d), in association with the strong surface cooling of the tropical Atlantic Ocean and the addition of isotopically depleted meltwater into the North Atlantic. Thus, the $\delta^{18}O_p$ response in this region would be classified as Type-5 according to the categorization of Lewis et al. (2010), with the mechanisms driving the $\delta^{18}O_p$ response governed by processes outside of the local or nonlocal amount effect, moisture source, or seasonality of precipitation.

3.5 Data-model comparisons

The proxy locations span 17 IPCC scientific regions (Fig. B2). The regions with densest Tier 1 proxy data coverage are southern Central America, northeastern South America, East Asia, and Southeast Asia/Maritime Continent. These four regions were therefore targeted for data-model comparisons. The proxy records within each region were compared to model-simulated anomalies in annual mean precipitation amount, amount-weighted $\delta^{18}O_p$, and effective moisture (P-E) to investigate data-model agreement in the four target regions.

In East Asia (Fig. 5; Tables 3 and 4), five speleothem records display isotopic enrichment events broadly corresponding to the large-scale enrichment pattern in $\delta^{18}O_p$ simulated by iCESM across South Asia and the Arabian Peninsula (Fig. 5a,b). This modeled enrichment pattern corresponds well with the broad isotopic enrichment found in proxy reconstructions spanning East Asia, the Arabian Peninsula, and southern Thailand. In iCESM, the Chinese speleothem records are located near the node of an east-west dipole pattern in $\delta^{18}O_p$ in eastern China, which is part of a larger zonal pattern of $\delta^{18}O_p$ anomalies, characterized by isotopic enrichment in the Middle East and Asia, and isotopic enrichment in the subtropics and extratropics of the North Pacific, extending into the eastern coast of China (Fig. 4a). This pattern was also noted in the 8.2 ka and Heinrich meltwater events performed with GISS ModelE-R (LeGrande and Schmidt, 2008; Lewis et al., 2010). Using vapor source distribution tracers, Lewis et al. (2010) identified changes in circulation, moisture source, and upwind processes as the dominant processes underpinning the $\delta^{18}O_p$ response in the East Asian monsoon region in their Heinrich simulations. In agreement with their results, the enriched $\delta^{18}O_p$ anomalies over Asia in the iCESM meltwater simulations do not appear to be driven by a weakened monsoon via a local amount effect, as the rainfall changes in the region are weak and spatially variable.

Northeastern South America displays only moderate proxy-model agreement (Fig. 6). Two of the four speleothem records there contain large $\delta^{18}O$ depletion events, corresponding with the large-scale isotopic depletion signal in $\delta^{18}O_p$ in iCESM across northeastern South America. However, two other speleothem records in the region–one in the Nordeste region of Brazil and one in central Brazil–show no significant hydroclimate anomalies during the 8.2 ka Event, in contrast with the results from iCESM.

In southern Central America, the simulated and reconstructed hydroclimate anomalies broadly agree (Fig. 7), with the dry event in the Guatemalan lake sediment record of Core5LI (Duarte et al., 2021) corresponding with the reduced precipitation throughout southern Central America simulated in iCESM. The lack of a detected event in three lake sediment records from the Yucatan Peninsula (LagoPuertoArturo, Curtis6VII93, LC1) also agrees with the simulated weak EM response in that region in iCESM. While a positive $\delta^{18}O_p$ event in the Costa Rican speleothem record (V1; Lachniet et al., 2004) contrasts with the weak simulated change in $\delta^{18}O_p$ at the overlapping model grid box, it is notable that the cave site sits at the nodal point of a pronounced east-west dipole pattern in $\delta^{18}O_p$ in iCESM, with widespread isotopic enrichment in $\delta^{18}O_p$ in the eastern tropical Pacific and widespread isotopic depletion in the tropical North Atlantic that stretches into the

Caribbean and Mesoamerica. Using this regional context, the isotopic enrichment event in Costa Rica is consistent with the simulated enrichment in $\delta^{18}O_p$ that extends from southernmost Central America to the northeastern tropical Pacific.

Broad data-model agreement is also found in Southeast Asia and the Maritime Continent (Fig. 8), where one speleothem record in the Thailand peninsula contains a notable isotopic enrichment event, in agreement with the simulated large scale enrichment signal in $\delta^{18}O_p$ in South Asia (Fig. 8 and Fig. B8). Two other speleothem records in Sumatra and Borneo show no significant hydroclimate anomalies, in general agreement with the weak simulated $\delta^{18}O_p$ anomalies in iCESM in this region, which reflect the weak response in $\delta^{18}O_p$ throughout the western Pacific and Maritime Continent (Fig. 4a).

These results suggest that iCESM captures many of the regional hydroclimate responses observed in the reconstructions, including the large-scale isotopic enrichment pattern in $\delta^{18}O_p$ in South and East Asia and the Arabian Peninsula, the muted hydroclimate response in the Maritime Continent, the drying and isotopic enrichment in southern Central America, and the isotopic depletion in $\delta^{18}O_p$ in parts of northeastern South America. Similar hydroclimate features also appear in simulations of the Younger Dryas cold event from Renssen et al (2018). While qualitative, these areas of agreement between the proxies and model demonstrate that the tropical hydroclimate response to North Atlantic meltwater forcing during the 8.2 ka Event was not a simple hemispheric dipole pattern, but is instead characterized by rich regional structure.

While qualitative agreement exists between many of the reconstructed and simulated regional hydroclimate anomalies during the 8.2 ka Event, our data-model comparisons are subject to several limitations. First, our regional analyses are limited by small sample sizes. In some regions like East Asia, point-to-point agreement between proxy and model data is low even though regional hydroclimate patterns offer more nuanced context. In addition, our data-model comparisons are necessarily qualitative as many of the proxy records in our compilation are carbonate $\delta^{18}O$ records, which do not solely reflect changes in $\delta^{18}O_p$. Rather, these archives incorporate a combination of the isotopic composition of groundwater (for speleothem $\delta^{18}O$ records; Lachniet, 2009) or seawater (for marine $\delta^{18}O$ records; Konecky et al., 2020) as well as the environmental temperature, among other factors (LeGrande and Schmidt, 2009; Bowen et al., 2019; Konecky et al., 2019). Thus, future work should integrate proxy system models with water isotope-enabled climate model simulations to develop more quantitative data-model comparisons of the 8.2 ka Event. In addition, quantitative metrics like the weighted Cohen's kappa statistic could be used to quantitatively compare the proxy reconstructions to the pseudoproxy data derived from climate models (Cohen, 1960; Cohen, 1968; Landis and Koch, 1977; DiNezio and Tierney, 2013).

However, even when attempting to bridge the gap between models and proxy data using proxy system models and quantitative metrics, robust comparisons remain challenging. Characterizing the point-to-point agreement between the observed and simulated climate anomalies fails to address the well-known hydroclimate biases that exist in GCMs, which arise from factors like course model resolution, idealized topography, and the unresolved physics of cloud formation and convection. Furthermore, proxy data often capture localized climate signals which may not be representative of regional

conditions. In contrast, model data are averaged over the area of a grid cell, which can be large in coarse-resolution models. This can lead to non-trivial biases, particularly in coastal regions and regions of complex topography. Ultimately, these data-model comparisons would be improved by the integration of additional well-dated proxy records that resolve different aspects of hydroclimate, and employing ensembles of high-resolution water isotope-enabled climate model simulations of the 8.2 ka Event paired with proxy system models.

4 Discussion

4.1 Comparison to previous hydroclimate compilations

The spatial pattern of hydroclimate responses to the 8.2 ka Event presented in this study broadly agrees with Morrill et al. (2013) and Parker and Harrison (2022). All three studies document large-scale drying across East Asia and the Arabian Peninsula, alongside robust wet and/or isotopic depletion signals in central and eastern Brazil. These signals coincide with drying and/or isotopic enrichment events in northern South America, aligning with the simulated hydroclimate response in iCESM (Fig. 4). All three reconstructions also agree on drying/enrichment in southern Central America, while both the present study and Parker and Harrison (2022) find a dipole pattern of wet/isotopically depleted conditions in the Caribbean/Gulf of Mexico and dry/isotopically enriched conditions in southern Central America (Fig. 4a-c).

Timing and duration estimates also show reasonable agreement across compilations. Our age ensembles yield a mean start age of 8.28±0.12 ka (1σ), a termination age of 8.11±0.09 ka (1σ), and an average duration of 152±70 years (1σ; 50-289 years). These results agree, within age uncertainty, to the initiation and termination of the global event estimated from northern Greenland ice core data (8.09 ka-8.25 ka; Thomas et al., 2007). Previous studies report comparable findings. Using eight absolutely dated speleothems from China, Oman, and Brazil, Cheng et al. (2009) estimated the onset of the 8.2 ka Event at 8.21 ka, termination at 8.08 ka, and a total duration of 130-150 years. Parker and Harrison (2022) refined these estimates using 275 absolutely dated speleothems, calculating the global onset at 8.22±0.01 ka, termination at 8.06±0.01 ka, and a duration of 159-166 years. While our range of event durations exceeds those in Cheng et al. (2009) and Parker and Harrison (2022), it is consistent with the estimated range of 40-270 years from the multiproxy compilation of Morrill et al. (2013). Importantly, the present study is the first to comprehensively account for age uncertainty by propagating age ensembles through all phases of event detection. Our larger uncertainties and duration range likely stem from this explicit treatment of age uncertainty, combined with the inclusion of lower-resolution lake and marine sediment records alongside higher-resolution speleothems in our compilation. In all cases, the average event duration in the hydroclimate records closely resembles that in the layer-counted Greenland ice core records (160.5±5.5 years; Thomas et al., 2007), providing further support of the global and synchronous nature of the 8.2 ka Event.

One striking difference between our compilation and previous studies is the relatively low percentage of records with detected 8.2 ka Events (e.g., only 30% of our records, compared to 70% in Parker and Harrison's [2022] global

speleothem compilation). This difference may arise from several factors. We focus exclusively on tropical proxy data, which are likely to record weaker anomalies than proxies from the North Atlantic and Europe, regions more directly impacted by proximity to the meltwater forcing. More importantly, our explicit accounting of age uncertainty reveals that many records lack sufficient age constraints, precluding the generation of age ensembles to pass the robust null hypothesis test in actR, and thereby fail to identify abrupt anomalies attributable to the 8.2 ka Event.

4.2 Comparison of the simulated 8.2 ka Event across models

Two lower-resolution isotope-enabled GCM simulations have previously been conducted to investigate the 8.2 ka Event. LeGrande and Schmidt (2008) used the Goddard Institute for Space Studies ModelE-R (GISS ModelE-R) to evaluate the response of global temperatures, precipitation amount, and $\delta^{18}O_p$ values to a slowdown of the AMOC. GISS ModelIE-R is a fully coupled GCM from the IPCC AR4 era, featuring a 4° x 5° horizontal resolution atmosphere model coupled with an ocean model of the same resolution, comprising 20 and 13 vertical layers, respectively. LeGrande and Schmidt (2008) performed a 1,000-year preindustrial control simulation and a suite of twelve meltwater forced experiments, applying a range of forcings (1.25 Sv to 10 Sv) over the Hudson Bay for 0.25 to 2 years. They found that this range of meltwater forcings inhibited North Atlantic Deep Water (NADW) formation and reduced the strength of the AMOC for up to 180 years.

In agreement with the results from iCESM, LeGrande and Schmidt (2008) found large $\delta^{18}O_p$ anomalies over the meltwater source area in the North Atlantic in the decade following the meltwater forcing, which they similarly attributed to the evaporation and rainout of the isotopically depleted meltwater in the region. They observed reasonable agreement between their simulations and proxy records of temperature and hydroclimate, with the simulations containing larger meltwater forcing exhibiting better agreement with the proxies (emphasizing the importance of considering an ensemble of simulations to find the best fit to proxy reconstructions). Regarding the tropical hydroclimate response, they identified bands of enriched (depleted) $\delta^{18}O_p$ anomalies in the northern (southern) tropics as a result of a southward shift in tropical rainfall. Notable patterns of $\delta^{18}O$ enrichment were identified in northeastern Africa, through the Middle East, South Asia, and the Thailand peninsula, which they attributed to large-scale changes in the hydrologic cycle, including shifts in moisture source and moisture transport pathways.

In a more recent set of simulations, Aguiar et al. (2021) used the University of Victoria Earth System Climate Model version 2.9 (UVic ESCM2.9) with the addition of oxygen isotopes to test proxy-model agreement under a range of empirically derived freshwater forcing scenarios. UVic ESCM2.9 uses the Modular Ocean Model version 2, with a horizontal resolution of 3.6° longitude x1.8° latitude and 19 vertical levels. The version of the UVic ESCM2.9 model used in this study possesses a simple two-dimensional atmospheric energy moisture balance model, which limits its ability to accurately represent $\delta^{18}O_p$ values. Aguiar et al. (2021) compared the sea surface temperatures and seawater $\delta^{18}O$ values from 28 simulations with 35 proxy records to place new constraints on the amount and rate of freshwater forcing in the North Atlantic. Their analysis revealed that a two-stage meltwater experiment with a background flux of 0.066 Sv over 1,000 years

(8 ka-9 ka), followed by an intensification to 0.19 Sv over 130 years (8.18 ka-8.31 ka), best replicated the anomalies observed in the proxy records.

The iCESM simulation illustrates clear signatures of the global 8.2 ka Event that, at the largest scales, are broadly consistent with the GISS and UVic simulations described above, including the hemispheric dipole pattern in temperature and associated southward shift of the tropical rainbands. On regional scales, the tropical rainfall patterns display substantial regional heterogeneity, with a southward shift of the tropical ocean rain bands, drying in the major NH monsoon regions of South Asia and West Africa, and wetting in parts of the South American Summer Monsoon. Tropical $\delta^{18}O_p$ values display strong signatures of the 8.2 ka Event, including opposing patterns of $\delta^{18}O_p$ values between northern South America and northeastern Brazil (e.g., Zhu et al., 2017) and large $\delta^{18}O_p$ anomalies over the meltwater region (e.g., LeGrande and Schmidt, 2008; Bowen et al., 2019). Dry (wet) anomalies correspond with enriched (depleted) $\delta^{18}O_p$ values in some tropical regions, implicating the "amount effect" as the driving force behind the isotopic signal, but a decoupling of precipitation amount and $\delta^{18}O_p$ anomalies occurs over many tropical continental regions, indicating that other processes such as changes in moisture source, moisture transport pathways, water recycling over land, and/or changes in precipitation seasonality, dominate the isotopic signal in those regions. The model simulations lend support to the proxy reconstructions in demonstrating that the tropical hydroclimate response to the 8.2 ka Event cannot be described as a simple hemispheric dipole pattern, particularly over continental regions, and that the rich regional structure of the precipitation amount and $\delta^{18}O_p$ responses must be considered in order to understand the full picture of the tropical hydroclimate response to this event.

5 Conclusions

This study has investigated the tropical hydroclimate response to the 8.2 ka Event in a new multi-proxy data compilation and ~~state-of-the-art~~ isotope-enabled model simulation. Two event detection methods were used in this study. The first method relies on the original age model of each record while the~~and uses the 7.9 ka-8.5 ka period as the detection window. The~~ second method implements a changepoint detection algorithm that explicitly accounts for age uncertainties in each proxy record. In order to leverage the strengths of each method and provide a more robust reconstruction of the hydroclimate response to the 8.2 ka Event, only records in which events were detected in both event detection methods were used to characterize the hydroclimate response to the 8.2 ka Event.

Robust hydroclimate anomalies were detected in 18 records across the 7.9 ka-8.5 ka interval while 12 records showed no evidence of a hydroclimate anomaly associated with the 8.2 ka Event. Across the records with a detected hydroclimate event, a mean onset age of 8.28±0.12 ka (1σ), mean termination age of 8.11±0.09 ka (1σ), and mean duration of 152±70 years (1σ; with a range of 50 to 289 years) was found, comparing well with previous estimates. Importantly, this work is the first to explicitly account for age uncertainty through all phases of the event detection analysis.

The results demonstrate that the tropical hydroclimate response to the North Atlantic meltwater forcing was not a simple hemispherically uniform dipole pattern but is better characterized by rich regional structure. Coherent regional

hydroclimate changes identified in the proxy records include pronounced isotopic enrichment across East Asia, South Asia, and the Arabian Peninsula. In the Americas, drying and isotopic enrichment occurred in southern Central America, contrasting with isotopic depletion in central/eastern Brazil. In contrast, no signatures of the 8.2 ka Event were found over the Maritime Continent.

The isotope-enabled model simulation with iCESM illustrates clear signatures of the global 8.2 ka Event that are largely consistent with the proxy records. Large-scale cooling in the Northern Hemisphere and warming in the Southern Hemisphere drives a southward shift of tropical rainfall but with highly variable regional patterns. Major features include a southward shift of the tropical ocean rain bands in the tropical Atlantic, Central and Eastern Pacific, and Indian Oceans (characterized by a weakening of the northern extent and enhancement of the southern extent of the rainbands), as well as drying in Central America and northern South America and wetter conditions in northeastern Brazil. Modest drying also occurs in the Northern Hemisphere monsoon regions of South Asia and West Africa. The simulated isotopic composition of tropical precipitation also displays strong signatures of the 8.2 ka Event. Over land, $\delta^{18}O_p$ displays a pronounced dipole pattern in South America, with isotopic enrichment in northern South America and isotopic depletion in northeastern Brazil. Large-scale isotopic depletion also occurs over the Arabian Peninsula and South Asia. Over the tropical oceans (excluding the western tropical Pacific~~namely the tropical Atlantic, Central and Eastern Pacific, and Indian Oceans~~), a pronounced north-south dipole pattern occurs in $\delta^{18}O_p$, with isotopic enrichment corresponding with drier conditions north of the equator and isotopic depletion corresponding with wetter conditions south of the equator. Precipitation amount and $\delta^{18}O_p$ anomalies are more muted in the Western Pacific, Maritime Continent, and Africa. We decompose the simulated $\delta^{18}O_p$ response to identify the causes of~~mechanisms driving~~ these isotopic anomalies in the tropics, finding that changes in amount-weighted $\delta^{18}O_p$ arise primarily from seasonal changes in the isotopic composition of precipitation rather than changes in precipitation seasonality. However, the mechanisms of the seasonal changes in $\delta^{18}O_p$ vary regionally, with the local amount effect dominant in northeastern South America and the northeastern tropical Pacific; while changes in the isotopic composition of the water vapor (via changes in moisture source, circulation~~ patterns~~, and/or upstream rainout) seem to control the response in East Asia; and the addition of isotopically depleted meltwater to the North Atlantic directly contributes to reduced, but isotopically depleted, wet season precipitation through the Caribbean.

The proxy records were compared to simulated $\delta^{18}O_p$, precipitation amount, and effective moisture (P-E) from co-located sites in four regions with the densest coverage of proxy data: southern Central America, northeastern South America, East Asia, and Southeast Asia. Subject to the small sample sizes found in the regional data-model comparisons, the results suggest that iCESM captures many of the regional hydroclimate responses observed in the reconstructions, including the large-scale isotopic enrichment pattern in $\delta^{18}O_p$ in South and East Asia and the Arabian Peninsula, the drying and isotopic enrichment in $\delta^{18}O_p$ in southern Central America, the isotopic depletion in parts of northeastern South America, and the muted hydroclimate response in the Maritime Continent.

These results serve as a first step toward more quantitative data-model comparison studies. Recommendations for future studies include adding more well-dated proxy records that resolve different aspects of hydroclimate during the 8.2 ka Event, and quantitatively comparing these records with ensembles of water isotope-enabled climate model simulations of the 8.2 ka Event paired with proxy system models. Future work should also investigate the physical mechanisms of the simulated hydroclimate responses and their isotopic signatures to improve our understanding of the tropical hydroclimate response to abrupt climate change events.

Author contributions. ARA and ALM conceptualized the study, with ARA securing funding and providing supervision. ALM performed proxy data curation and led the proxy data analysis with contributions from RP. ALM performed the iCESM simulations and led the writing of the manuscript and the design of figures with contributions from ARA.

Competing interests. The authors declare that they have no conflict of interest.

Acknowledgements. This work was supported by NSF-EAR 2002444 to ARA. Computing resources were provided to ALM by the Climate Simulation Laboratory at NCAR's Computational and Information Systems Laboratory (CISL). We gratefully acknowledge Julian Sachs for providing early inspiration for the project as well as Jiang Zhu at NCAR for his assistance setting up the iCESM simulations. We also gratefully acknowledge the PMIP4 Community and the Linked Earth team, including Nick McKay and Julien Emile-Geay, for providing access to and invaluable assistance with actR (https://github.com/LinkedEarth/actR).

References

Aguiar, W., Prado, L. F., Wainer, I., Liu, Z., Montenegro, A., Meissner, K. J., and Mata, M. M.: Freshwater forcing control on early-Holocene South American monsoon, Quaternary Science Reviews, 245, 106498, https://doi.org/10.1016/j.quascirev.2020.106498, 2020.

Aguiar, W., Meissner, K. J., Montenegro, A., Prado, L., Wainer, I., Carlson, A. E., and Mata, M. M.: Magnitude of the 8.2 ka event freshwater forcing based on stable isotope modelling and comparison to future Greenland melting, Scientific Reports, 11, 5473, https://doi.org/10.1038/s41598-021-84709-5, 2021.

Alley, R. B., Mayewski, P. A., Sowers, T., Stuiver, M., Taylor, K. C., and Clark, P. U.: Holocene climatic instability: A prominent, widespread event 8200 yr ago, Geology, 25, 483–486, https://doi.org/10.1130/0091-7613(1997)025<0483:HCIAPW>2.3.CO;2, 1997.

Arbuszewski, J. A., deMenocal, P. B., Cléroux, C., Bradtmiller, L., and Mix, A.: Meridional shifts of the Atlantic intertropical convergence zone since the Last Glacial Maximum, Nature Geosci, 6, 959–962, https://doi.org/10.1038/ngeo1961, 2013.

Atwood, A. R., Donohoe, A., Battisti, D. S., Liu, X., and Pausata, F. S. R.: Robust Longitudinally Variable Responses of the ITCZ to a Myriad of Climate Forcings, Geophysical Research Letters, 47, e2020GL088833, https://doi.org/10.1029/2020GL088833, 2020.

Ayliffe, L. K., Gagan, M. K., Zhao, J., Drysdale, R. N., Hellstrom, J. C., Hantoro, W. S., Griffiths, M. L., Scott-Gagan, H., Pierre, E. S., Cowley, J. A., and Suwargadi, B. W.: Rapid interhemispheric climate links via the Australasian monsoon during the last deglaciation, Nat Commun, 4, 2908, https://doi.org/10.1038/ncomms3908, 2013.

Azevedo, V., Strikis, N. M., Novello, V. F., Roland, C. L., Cruz, F. W., Santos, R. V., Vuille, M., Utida, G., De Andrade, F. R. D., Cheng, H., and Edwards, R. L.: Paleovegetation seesaw in Brazil since the Late Pleistocene: A multiproxy study of two biomes, Earth and Planetary Science Letters, 563, 116880, https://doi.org/10.1016/j.epsl.2021.116880, 2021.

Barber, D. C., Dyke, A., Hillaire-Marcel, C., Jennings, A. E., Andrews, J. T., Kerwin, M. W., Bilodeau, G., McNeely, R., Southon, J., Morehead, M. D., and Gagnon, J.-M.: Forcing of the cold event of 8,200 years ago by catastrophic drainage of Laurentide lakes, Nature, 400, 344–348, https://doi.org/10.1038/22504, 1999.

Berkelhammer, M., Sinha, A., Stott, L., Cheng, H., Pausata, F. S. R., and Yoshimura, K.: An Abrupt Shift in the Indian Monsoon 4000 Years Ago, in: Geophysical Monograph Series, edited by: Giosan, L., Fuller, D. Q., Nicoll, K., Flad, R. K., and Clift, P. D., American Geophysical Union, Washington, D. C., 75–88, https://doi.org/10.1029/2012GM001207, 2013.

Bernal, J. P., Cruz, F. W., Stríkis, N. M., Wang, X., Deininger, M., Catunda, M. C. A., Ortega-Obregón, C., Cheng, H., Edwards, R. L., and Auler, A. S.: High-resolution Holocene South American monsoon history recorded by a speleothem from Botuverá Cave, Brazil, Earth and Planetary Science Letters, 450, 186–196, https://doi.org/10.1016/j.epsl.2016.06.008, 2016.

Biasutti, M., Voigt, A., Boos, W. R., Braconnot, P., Hargreaves, J. C., Harrison, S. P., Kang, S. M., Mapes, B. E., Scheff, J., Schumacher, C., Sobel, A. H., and Xie, S.-P.: Global energetics and local physics as drivers of past, present and future monsoons, Nature Geosci, 11, 392–400, https://doi.org/10.1038/s41561-018-0137-1, 2018.

Bird, B. W., Abbott, M. B., Rodbell, D. T., and Vuille, M.: Holocene tropical South American hydroclimate revealed from a decadally resolved lake sediment $\delta^{18}O$ record, Earth and Planetary Science Letters, 310, 192–202, https://doi.org/10.1016/j.epsl.2011.08.040, 2011.

Bird, B. W., Polisar, P. J., Lei, Y., Thompson, L. G., Yao, T., Finney, B. P., Bain, D. J., Pompeani, D. P., and Steinman, B. A.: A Tibetan lake sediment record of Holocene Indian summer monsoon variability, Earth and Planetary Science Letters, 399, 92–102, https://doi.org/10.1016/j.epsl.2014.05.017, 2014.

Blaauw, M. and Christen, J. A.: Flexible paleoclimate age-depth models using an autoregressive gamma process, Bayesian Analysis, 6, 457–474, https://doi.org/10.1214/11-BA618, 2011.

Bowen, G. J., Cai, Z., Fiorella, R. P., and Putman, A. L.: Isotopes in the Water Cycle: Regional- to Global-Scale Patterns and Applications, Annu. Rev. Earth Planet. Sci., 47, 453–479, https://doi.org/10.1146/annurev-earth-053018-060220, 2019.

Brady, E., Stevenson, S., Bailey, D., Liu, Z., Noone, D., Nusbaumer, J., Otto-Bliesner, B. L., Tabor, C., Tomas, R., Wong, T., Zhang, J., and Zhu, J.: The Connected Isotopic Water Cycle in the Community Earth System Model Version 1, J Adv Model Earth Syst, 11, 2547–2566, https://doi.org/10.1029/2019MS001663, 2019.

Breitenbach, S. F. M., Rehfeld, K., Goswami, B., Baldini, J. U. L., Ridley, H. E., Kennett, D. J., Prufer, K. M., Aquino, V. V., Asmerom, Y., Polyak, V. J., Cheng, H., Kurths, J., and Marwan, N.: COnstructing Proxy Records from Age models (COPRA), Clim. Past, 8, 1765–1779, https://doi.org/10.5194/cp-8-1765-2012, 2012.

Bustamante, M. G., Cruz, F. W., Vuille, M., Apaéstegui, J., Strikis, N., Panizo, G., Novello, F. V., Deininger, M., Sifeddine, A., Cheng, H., Moquet, J. S., Guyot, J. L., Santos, R. V., Segura, H., and Edwards, R. L.: Holocene changes in monsoon precipitation in the Andes of NE Peru based on $\delta^{18}O$ speleothem records, Quaternary Science Reviews, 146, 274–287, https://doi.org/10.1016/j.quascirev.2016.05.023, 2016.

Cai, Y., Fung, I. Y., Edwards, R. L., An, Z., Cheng, H., Lee, J.-E., Tan, L., Shen, C.-C., Wang, X., Day, J. A., Zhou, W., Kelly, M. J., and Chiang, J. C. H.: Variability of stalagmite-inferred Indian monsoon precipitation over the past 252,000 y, Proc. Natl. Acad. Sci. U.S.A., 112, 2954–2959, https://doi.org/10.1073/pnas.1424035112, 2015.

Carlson, A. E., Clark, P. U., Haley, B. A., and Klinkhammer, G. P.: Routing of western Canadian Plains runoff during the 8.2 ka cold event, Geophysical Research Letters, 36, 2009GL038778, https://doi.org/10.1029/2009GL038778, 2009.

Carolin, S. A., Cobb, K. M., Lynch-Stieglitz, J., Moerman, J. W., Partin, J. W., Lejau, S., Malang, J., Clark, B., Tuen, A. A., and Adkins, J. F.: Northern Borneo stalagmite records reveal West Pacific hydroclimate across MIS 5 and 6, Earth and Planetary Science Letters, 439, 182–193, https://doi.org/10.1016/j.epsl.2016.01.028, 2016.

Chawchai, S., Tan, L., Löwemark, L., Wang, H.-C., Yu, T.-L., Chung, Y.-C., Mii, H.-S., Liu, G., Blaauw, M., Gong, S.-Y., Wohlfarth, B., and Shen, C.-C.: Hydroclimate variability of central Indo-Pacific region during the Holocene, Quaternary Science Reviews, 253, 106779, https://doi.org/10.1016/j.quascirev.2020.106779, 2021.

Chen, J., Rao, Z., Liu, J., Huang, W., Feng, S., Dong, G., Hu, Y., Xu, Q., and Chen, F.: On the timing of the East Asian summer monsoon maximum during the Holocene—Does the speleothem oxygen isotope record reflect monsoon rainfall variability?, Sci. China Earth Sci., 59, 2328–2338, https://doi.org/10.1007/s11430-015-5500-5, 2016a.

Chen, S., Hoffmann, S. S., Lund, D. C., Cobb, K. M., Emile-Geay, J., and Adkins, J. F.: A high-resolution speleothem record of western equatorial Pacific rainfall: Implications for Holocene ENSO evolution, Earth and Planetary Science Letters, 442, 61–71, https://doi.org/10.1016/j.epsl.2016.02.050, 2016b.

Cheng, H., Fleitmann, D., Edwards, R. L., Wang, X., Cruz, F. W., Auler, A. S., Mangini, A., Wang, Y., Kong, X., Burns, S. J., and Matter, A.: Timing and structure of the 8.2 kyr B.P. event inferred from $\delta^{18}O$ records of stalagmites from China, Oman, and Brazil, Geology, 37, 1007–1010, https://doi.org/10.1130/G30126A.1, 2009.

Cheng, H., Sinha, A., Cruz, F. W., Wang, X., Edwards, R. L., d'Horta, F. M., Ribas, C. C., Vuille, M., Stott, L. D., and Auler, A. S.: Climate change patterns in Amazonia and biodiversity, Nat Commun, 4, 1411, https://doi.org/10.1038/ncomms2415, 2013.

Chiang, J. C. H. and Bitz, C. M.: Influence of high latitude ice cover on the marine Intertropical Convergence Zone, Climate Dynamics, 25, 477–496, https://doi.org/10.1007/s00382-005-0040-5, 2005.

Chiang, J. C. H., Herman, M. J., Yoshimura, K., and Fung, I. Y.: Enriched East Asian oxygen isotope of precipitation indicates reduced summer seasonality in regional climate and westerlies, Proc. Natl. Acad. Sci. U.S.A., 117, 14745–14750, https://doi.org/10.1073/pnas.1922602117, 2020.

Cohen, J.: A Coefficient of Agreement for Nominal Scales, Educational and Psychological Measurement, 20, 37–46, https://doi.org/10.1177/001316446002000104, 1960.

Cohen, J.: Weighted kappa: Nominal scale agreement provision for scaled disagreement or partial credit., Psychological Bulletin, 70, 213–220, https://doi.org/10.1037/h0026256, 1968.

Comas-Bru, L., Rehfeld, K., Roesch, C., Amirnezhad-Mozhdehi, S., Harrison, S. P., Atsawawaranunt, K., Ahmad, S. M., Brahim, Y. A., Baker, A., Bosomworth, M., Breitenbach, S. F. M., Burstyn, Y., Columbu, A., Deininger, M., Demény, A., Dixon, B., Fohlmeister, J., Hatvani, I. G., Hu, J., Kaushal, N., Kern, Z., Labuhn, I., Lechleitner, F. A., Lorrey, A., Martrat, B., Novello, V. F., Oster, J., Pérez-Mejías, C., Scholz, D., Scroxton, N., Sinha, N., Ward, B. M., Warken, S., Zhang, H., and SISAL Working Group members: SISALv2: a comprehensive speleothem isotope database with multiple age–depth models, Earth Syst. Sci. Data, 12, 2579–2606, https://doi.org/10.5194/essd-12-2579-2020, 2020.

Conroy, J. L., Overpeck, J. T., Cole, J. E., Shanahan, T. M., and Steinitz-Kannan, M.: Holocene changes in eastern tropical Pacific climate inferred from a Galápagos lake sediment record, Quaternary Science Reviews, 27, 1166–1180, https://doi.org/10.1016/j.quascirev.2008.02.015, 2008.

Cruz, F. W., Vuille, M., Burns, S. J., Wang, X., Cheng, H., Werner, M., Lawrence Edwards, R., Karmann, I., Auler, A. S., and Nguyen, H.: Orbitally driven east–west antiphasing of South American precipitation, Nature Geosci, 2, 210–214, https://doi.org/10.1038/ngeo444, 2009.

Curtis, J. H., Brenner, M., Hodell, D. A., Balser, R. A., Islebe, G. A., and Hooghiemstra, H.: A multi-proxy study of Holocene environmental change in the Maya Lowlands of Peten, Guatemala, Journal of Paleolimnology, 19, 139–159, https://doi.org/10.1023/A:1007968508262, 1998.

Denniston, R. F., Wyrwoll, K.-H., Polyak, V. J., Brown, J. R., Asmerom, Y., Wanamaker, A. D., LaPointe, Z., Ellerbroek, R., Barthelmes, M., Cleary, D., Cugley, J., Woods, D., and Humphreys, W. F.: A Stalagmite record of Holocene Indonesian–Australian summer monsoon variability from the Australian tropics, Quaternary Science Reviews, 78, 155–168, https://doi.org/10.1016/j.quascirev.2013.08.004, 2013.

DiNezio, P. N. and Tierney, J. E.: The effect of sea level on glacial Indo-Pacific climate, Nature Geosci, 6, 485–491, https://doi.org/10.1038/ngeo1823, 2013.

Duan, P., Li, H., Sinha, A., Voarintsoa, N. R. G., Kathayat, G., Hu, P., Zhang, H., Ning, Y., and Cheng, H.: The timing and structure of the 8.2 ka event revealed through high-resolution speleothem records from northwestern Madagascar, Quaternary Science Reviews, 268, 107104, https://doi.org/10.1016/j.quascirev.2021.107104, 2021.

Duarte, E., Obrist-Farner, J., Correa-Metrio, A., and Steinman, B. A.: A progressively wetter early through middle Holocene climate in the eastern lowlands of Guatemala, Earth and Planetary Science Letters, 561, 116807, https://doi.org/10.1016/j.epsl.2021.116807, 2021.

Dutt, S., Gupta, A. K., Clemens, S. C., Cheng, H., Singh, R. K., Kathayat, G., and Edwards, R. L.: Abrupt changes in Indian summer monsoon strength during 33,800 to 5500 years B.P.: INDIAN SUMMER MONSOON, Geophys. Res. Lett., 42, 5526–5532, https://doi.org/10.1002/2015GL064015, 2015.

Dykoski, C., Edwards, R., Cheng, H., Yuan, D., Cai, Y., Zhang, M., Lin, Y., Qing, J., An, Z., and Revenaugh, J.: A high-resolution, absolute-dated Holocene and deglacial Asian monsoon record from Dongge Cave, China, Earth and Planetary Science Letters, 233, 71–86, https://doi.org/10.1016/j.epsl.2005.01.036, 2005.

Ellison, C. R. W., Chapman, M. R., and Hall, I. R.: Surface and Deep Ocean Interactions During the Cold Climate Event 8200 Years Ago, Science, 312, 1929–1932, https://doi.org/10.1126/science.1127213, 2006.

Escobar, J., Hodell, D. A., Brenner, M., Curtis, J. H., Gilli, A., Mueller, A. D., Anselmetti, F. S., Ariztegui, D., Grzesik, D. A., Pérez, L., Schwalb, A., and Guilderson, T. P.: A ~43-ka record of paleoenvironmental change in the Central American lowlands inferred from stable isotopes of lacustrine ostracods, Quaternary Science Reviews, 37, 92–104, https://doi.org/10.1016/j.quascirev.2012.01.020, 2012.

Fensterer, C., Scholz, D., Hoffmann, D. L., Spötl, C., Schröder-Ritzrau, A., Horn, C., Pajón, J. M., and Mangini, A.: Millennial-scale climate variability during the last 12.5 ka recorded in a Caribbean speleothem, Earth and Planetary Science Letters, 361, 143–151, https://doi.org/10.1016/j.epsl.2012.11.019, 2013.

Fleitmann, D., Burns, S. J., Mangini, A., Mudelsee, M., Kramers, J., Villa, I., Neff, U., Al-Subbary, A. A., Buettner, A., Hippler, D., and Matter, A.: Holocene ITCZ and Indian monsoon dynamics recorded in stalagmites from Oman and Yemen (Socotra), Quaternary Science Reviews, 26, 170–188, https://doi.org/10.1016/j.quascirev.2006.04.012, 2007.

Geen, R., Bordoni, S., Battisti, D. S., and Hui, K.: Monsoons, ITCZs, and the Concept of the Global Monsoon, Reviews of Geophysics, 58, https://doi.org/10.1029/2020RG000700, 2020.

Haslett, J. and Parnell, A.: A Simple Monotone Process with Application to Radiocarbon-Dated Depth Chronologies, Journal of the Royal Statistical Society Series C: Applied Statistics, 57, 399–418, https://doi.org/10.1111/j.1467-9876.2008.00623.x, 2008.

Hillman, A. L., Yao, A., Finkenbinder, M. S., and Abbott, M. B.: A 17,000-year multi-proxy study of the Indian Summer Monsoon from Lake Dian, Yunnan, China, Palaeogeography, Palaeoclimatology, Palaeoecology, 567, 110292, https://doi.org/10.1016/j.palaeo.2021.110292, 2021.

Hodell, D. A., Curtis, J. H., and Brenner, M.: Possible role of climate in the collapse of Classic Maya civilization, Nature, 375, 391–394, https://doi.org/10.1038/375391a0, 1995.

Holmgren, K., Lee-Thorp, J. A., Cooper, G. R. J., Lundblad, K., Partridge, T. C., Scott, L., Sithaldeen, R., Siep Talma, A., and Tyson, P. D.: Persistent millennial-scale climatic variability over the past 25,000 years in Southern Africa, Quaternary Science Reviews, 22, 2311–2326, https://doi.org/10.1016/S0277-3791(03)00204-X, 2003.

Hu, J., Emile-Geay, J., Tabor, C., Nusbaumer, J., and Partin, J.: Deciphering Oxygen Isotope Records From Chinese Speleothems With an Isotope-Enabled Climate Model, Paleoceanography and Paleoclimatology, 34, 2098–2112, https://doi.org/10.1029/2019PA003741, 2019.

Huang, W., Wang, Y., Cheng, H., Edwards, R. L., Shen, C.-C., Liu, D., Shao, Q., Deng, C., Zhang, Z., and Wang, Q.: Multi-scale Holocene Asian monsoon variability deduced from a twin-stalagmite record in southwestern China, Quat. res., 86, 34–44, https://doi.org/10.1016/j.yqres.2016.05.001, 2016.

Huguet, C., Routh, J., Fietz, S., Lone, M. A., Kalpana, M. S., Ghosh, P., Mangini, A., Kumar, V., and Rangarajan, R.: Temperature and Monsoon Tango in a Tropical Stalagmite: Last Glacial-Interglacial Climate Dynamics, Sci Rep, 8, 5386, https://doi.org/10.1038/s41598-018-23606-w, 2018.

Iturbide, M., Gutiérrez, J. M., Alves, L. M., Bedia, J., Cerezo-Mota, R., Cimadevilla, E., Cofiño, A. S., Di Luca, A., Faria, S. H., Gorodetskaya, I. V., Hauser, M., Herrera, S., Hennessy, K., Hewitt, H. T., Jones, R. G., Krakovska, S., Manzanas, R., Martínez-Castro, D., Narisma, G. T., Nurhati, I. S., Pinto, I., Seneviratne, S. I., Van Den Hurk, B., and Vera, C. S.: An update of IPCC climate reference regions for subcontinental analysis of climate model data: definition and aggregated datasets, Earth Syst. Sci. Data, 12, 2959–2970, https://doi.org/10.5194/essd-12-2959-2020, 2020.

Jiang, X., He, Y., Shen, C., Kong, X., Li, Z., and Chang, Y.: Stalagmite-inferred Holocene precipitation in northern Guizhou Province, China, and asynchronous termination of the Climatic Optimum in the Asian monsoon territory, Chin. Sci. Bull., 57, 795–801, https://doi.org/10.1007/s11434-011-4848-6, 2012.

Johnson, T. C., Brown, E. T., McManus, J., Barry, S., Barker, P., and Gasse, F.: A High-Resolution Paleoclimate Record Spanning the Past 25,000 Years in Southern East Africa, Science, 296, 113–132, https://doi.org/10.1126/science.1070057, 2002.

Kang, S. M., Held, I. M., Frierson, D. M. W., and Zhao, M.: The Response of the ITCZ to Extratropical Thermal Forcing: Idealized Slab-Ocean Experiments with a GCM, Journal of Climate, 21, 3521–3532, https://doi.org/10.1175/2007JCLI2146.1, 2008.

Kang, S. M., Frierson, D. M. W., and Held, I. M.: The Tropical Response to Extratropical Thermal Forcing in an Idealized GCM: The Importance of Radiative Feedbacks and Convective Parameterization, Journal of the Atmospheric Sciences, 66, 2812–2827, https://doi.org/10.1175/2009JAS2924.1, 2009.

Killick, R., Fearnhead, P., and Eckley, I. A.: Optimal Detection of Changepoints With a Linear Computational Cost, Journal of the American Statistical Association, 107, 1590–1598, https://doi.org/10.1080/01621459.2012.737745, 2012.

Kobashi, T., Severinghaus, J. P., Brook, E. J., Barnola, J.-M., and Grachev, A. M.: Precise timing and characterization of abrupt climate change 8200 years ago from air trapped in polar ice, Quaternary Science Reviews, 26, 1212–1222, https://doi.org/10.1016/j.quascirev.2007.01.009, 2007.

Konecky, B. L., Noone, D. C., and Cobb, K. M.: The Influence of Competing Hydroclimate Processes on Stable Isotope Ratios in Tropical Rainfall, Geophys. Res. Lett., 46, 1622–1633, https://doi.org/10.1029/2018GL080188, 2019.

Konecky, B. L., McKay, N. P., Churakova (Sidorova), O. V., Comas-Bru, L., Dassié, E. P., DeLong, K. L., Falster, G. M., Fischer, M. J., Jones, M. D., Jonkers, L., Kaufman, D. S., Leduc, G., Managave, S. R., Martrat, B., Opel, T., Orsi, A. J., Partin, J. W., Sayani, H. R., Thomas, E. K., Thompson, D. M., Tyler, J. J., Abram, N. J., Atwood, A. R., Cartapanis, O., Conroy, J. L., Curran, M. A., Dee, S. G., Deininger, M., Divine, D. V., Kern, Z., Porter, T. J., Stevenson, S. L., von Gunten, L., and Iso2k Project Members: The Iso2k database: a global compilation of paleo-$\delta^{18}O$ and $\delta^{2}H$ records to aid understanding of Common Era climate, Earth Syst. Sci. Data, 12, 2261–2288, https://doi.org/10.5194/essd-12-2261-2020, 2020.

Koutavas, A. and Lynch-Stieglitz, J.: Variability of the Marine ITCZ over the Eastern Pacific during the Past 30,000 Years, in: The Hadley Circulation: Present, Past and Future, vol. 21, edited by: Diaz, H. F. and Bradley, R. S., Springer Netherlands, Dordrecht, 347–369, https://doi.org/10.1007/978-1-4020-2944-8_13, 2004.

Lachniet, M. S.: Climatic and environmental controls on speleothem oxygen-isotope values, Quaternary Science Reviews, 28, 412–432, https://doi.org/10.1016/j.quascirev.2008.10.021, 2009.

Lachniet, M. S., Asmerom, Y., Burns, S. J., Patterson, W. P., Polyak, V. J., and Seltzer, G. O.: Tropical response to the 8200 yr B.P. cold event? Speleothem isotopes indicate a weakened early Holocene monsoon in Costa Rica, Geol, 32, 957, https://doi.org/10.1130/G20797.1, 2004.

Landis, J. R. and Koch, G. G.: The Measurement of Observer Agreement for Categorical Data, Biometrics, 33, 159, https://doi.org/10.2307/2529310, 1977.

Lechleitner, F. A., Breitenbach, S. F. M., Cheng, H., Plessen, B., Rehfeld, K., Goswami, B., Marwan, N., Eroglu, D., Adkins, J., and Haug, G.: Climatic and in-cave influences on δ 18 O and δ 13 C in a stalagmite from northeastern India through the last deglaciation, Quat. res., 88, 458–471, https://doi.org/10.1017/qua.2017.72, 2017.

LeGrande, A. N. and Schmidt, G. A.: Ensemble, water isotope–enabled, coupled general circulation modeling insights into the 8.2 ka event, Paleoceanography, 23, n/a-n/a, https://doi.org/10.1029/2008PA001610, 2008.

LeGrande, A. N. and Schmidt, G. A.: Sources of Holocene variability of oxygen isotopes in paleoclimate archives, Clim. Past, 15, 2009.

Lewis, S. C., LeGrande, A. N., Kelley, M., and Schmidt, G. A.: Water vapour source impacts on oxygen isotope variability in tropical precipitation during Heinrich events, Clim. Past, 6, 325–343, https://doi.org/10.5194/cp-6-325-2010, 2010.

Li, G. and Xie, S.-P.: Tropical Biases in CMIP5 Multimodel Ensemble: The Excessive Equatorial Pacific Cold Tongue and Double ITCZ Problems, Journal of Climate, 27, 1765–1780, https://doi.org/10.1175/JCLI-D-13-00337.1, 2014.

Li, T.-Y., Shen, C.-C., Li, H.-C., Li, J.-Y., Chiang, H.-W., Song, S.-R., Yuan, D.-X., Lin, C. D.-J., Gao, P., Zhou, L., Wang, J.-L., Ye, M.-Y., Tang, L.-L., and Xie, S.-Y.: Oxygen and carbon isotopic systematics of aragonite speleothems and water in Furong Cave, Chongqing, China, Geochimica et Cosmochimica Acta, 75, 4140–4156, https://doi.org/10.1016/j.gca.2011.04.003, 2011.

Li, Y.-X., Törnqvist, T. E., Nevitt, J. M., and Kohl, B.: Synchronizing a sea-level jump, final Lake Agassiz drainage, and abrupt cooling 8200 years ago, Earth and Planetary Science Letters, 315–316, 41–50, https://doi.org/10.1016/j.epsl.2011.05.034, 2012.

Liu, Y.-H., Henderson, G. M., Hu, C.-Y., Mason, A. J., Charnley, N., Johnson, K. R., and Xie, S.-C.: Links between the East Asian monsoon and North Atlantic climate during the 8,200 year event, Nature Geosci, 6, 117–120, https://doi.org/10.1038/ngeo1708, 2013.

LoDico, J. M., Flower, B. P., and Quinn, T. M.: Subcentennial-scale climatic and hydrologic variability in the Gulf of Mexico during the early Holocene: HOLOCENE CLIMATE CHANGE, Paleoceanography, 21, https://doi.org/10.1029/2005PA001243, 2006.

McKay, N. and Emile-Geay, J.: The Abrupt Change Toolkit in R, https://doi.org/10.5281/ZENODO.6926612, 2022.

McKay, N. P. and Emile-Geay, J.: Technical note: The Linked Paleo Data framework –\hack\newline a common tongue for paleoclimatology, Climate of the Past, 12, 1093–1100, https://doi.org/10.5194/cp-12-1093-2016, 2016.

McKay, N. P., Emile-Geay, J., and Khider, D.: geoChronR – an R package to model, analyze, and visualize age-uncertain data, Geochronology, 3, 149–169, https://doi.org/10.5194/gchron-3-149-2021, 2021.

Morrill, C., Anderson, D. M., Bauer, B. A., Buckner, R., Gille, E. P., Gross, W. S., Hartman, M., and Shah, A.: Proxy benchmarks for intercomparison of 8.2 ka simulations, Clim. Past, 9, 423–432, https://doi.org/10.5194/cp-9-423-2013, 2013.

Neff, U., Burns, S. J., Mangini, A., Mudelsee, M., Fleitmann, D., and Matter, A.: Strong coherence between solar variability and the monsoon in Oman between 9 and 6 kyr ago, Nature, 411, 290–293, https://doi.org/10.1038/35077048, 2001.

Novello, V. F., Cruz, F. W., Vuille, M., Stríkis, N. M., Edwards, R. L., Cheng, H., Emerick, S., De Paula, M. S., Li, X., Barreto, E. D. S., Karmann, I., and Santos, R. V.: A high-resolution history of the South American Monsoon from Last Glacial Maximum to the Holocene, Sci Rep, 7, 44267, https://doi.org/10.1038/srep44267, 2017.

Otto-Bliesner, B. L., Braconnot, P., Harrison, S. P., Lunt, D. J., Abe-Ouchi, A., Albani, S., Bartlein, P. J., Capron, E., Carlson, A. E., Dutton, A., Fischer, H., Goelzer, H., Govin, A., Haywood, A., Joos, F., LeGrande, A. N., Lipscomb, W. H., Lohmann, G., Mahowald, N., Nehrbass-Ahles, C., Pausata, F. S. R., Peterschmitt, J.-Y., Phipps, S. J., Renssen, H., and Zhang, Q.: The PMIP4 contribution to CMIP6 – Part 2: Two interglacials, scientific objective and experimental design for Holocene and \hack\newline Last Interglacial simulations, Geoscientific Model Development, 10, 3979–4003, https://doi.org/10.5194/gmd-10-3979-2017, 2017.

Parker, S. E. and Harrison, S. P.: The timing, duration and magnitude of the 8.2 ka event in global speleothem records, Sci Rep, 12, 10542, https://doi.org/10.1038/s41598-022-14684-y, 2022.

Pausata, F. S. R., Battisti, D. S., Nisancioglu, K. H., and Bitz, C. M.: Chinese stalagmite $\delta^{18}O$ controlled by changes in the Indian monsoon during a simulated Heinrich event, Nature Geosci, 4, 474–480, https://doi.org/10.1038/ngeo1169, 2011.

Peltier, W. R.: Global glacial isostasy and the surface of the ice-age Earth: The ICE-5G (VM2) model and GRACE, Annu. Rev. Earth Planet. Sci., 32, 111–149, https://doi.org/10.1146/annurev.earth.32.082503.144359, 2004.

Peltier, W. R., Argus, D. F., and Drummond, R.: Space geodesy constrains ice age terminal deglaciation: The global ICE-6G_C (VM5a) model: Global Glacial Isostatic Adjustment, J. Geophys. Res. Solid Earth, 120, 450–487, https://doi.org/10.1002/2014JB011176, 2015.

Penny, A.: State of the Tropics (2021) The Digital Divide in the Tropics, James Cook University, Townsville, Australia, 2021.

Polissar, P. J., Abbott, M. B., Wolfe, A. P., Vuille, M., and Bezada, M.: Synchronous interhemispheric Holocene climate trends in the tropical Andes, Proc. Natl. Acad. Sci. U.S.A., 110, 14551–14556, https://doi.org/10.1073/pnas.1219681110, 2013.

R Core Team: R: A Language and Environment for Statistical Computing, 2021.

Renssen, H., Goosse, H., Roche, D. M., and Seppä, H.: The global hydroclimate response during the Younger Dryas event, Quaternary Science Reviews, 193, 84–97, https://doi.org/10.1016/j.quascirev.2018.05.033, 2018.

Rhodes, R. H., Brook, E. J., Chiang, J. C. H., Blunier, T., Maselli, O. J., McConnell, J. R., Romanini, D., and Severinghaus, J. P.: Enhanced tropical methane production in response to iceberg discharge in the North Atlantic, Science, 348, 1016–1019, https://doi.org/10.1126/science.1262005, 2015.

Roberts, W. H. G. and Hopcroft, P. O.: Controls on the Tropical Response to Abrupt Climate Changes, Geophys. Res. Lett., 47, https://doi.org/10.1029/2020GL087518, 2020.

Rohling, E. J. and Pälike, H.: Centennial-scale climate cooling with a sudden cold event around 8,200 years ago, Nature, 434, 975–979, https://doi.org/10.1038/nature03421, 2005.

Russell, J. M., Vogel, H., Konecky, B. L., Bijaksana, S., Huang, Y., Melles, M., Wattrus, N., Costa, K., and King, J. W.: Glacial forcing of central Indonesian hydroclimate since 60,000 y B.P., Proc. Natl. Acad. Sci. U.S.A., 111, 5100–5105, https://doi.org/10.1073/pnas.1402373111, 2014.

Schmidt, M. W., Weinlein, W. A., Marcantonio, F., and Lynch-Stieglitz, J.: Solar forcing of Florida Straits surface salinity during the early Holocene: HOLOCENE TROPICAL HYDROLOGIC CYCLE, Paleoceanography, 27, n/a-n/a, https://doi.org/10.1029/2012PA002284, 2012.

Schneider, T., Bischoff, T., and Haug, G. H.: Migrations and dynamics of the intertropical convergence zone, Nature, 513, 45–53, https://doi.org/10.1038/nature13636, 2014.

Staubwasser, M., Sirocko, F., Grootes, P. M., and Segl, M.: Climate change at the 4.2 ka BP termination of the Indus valley civilization and Holocene south Asian monsoon variability: SOUTH ASIAN HOLOCENE CLIMATE CHANGE, Geophys. Res. Lett., 30, https://doi.org/10.1029/2002GL016822, 2003.

Strikis, N. M., Cruz, F. W., Cheng, H., Karmann, I., Edwards, R. L., Vuille, M., Wang, X., De Paula, M. S., Novello, V. F., and Auler, A. S.: Abrupt variations in South American monsoon rainfall during the Holocene based on a speleothem record from central-eastern Brazil, Geology, 39, 1075–1078, https://doi.org/10.1130/G32098.1, 2011.

Sullivan, R. M., van Hengstum, P. J., Coats, S. J., Donnelly, J. P., Tamalavage, A. E., Winkler, T. S., and Albury, N. A.: Hydroclimate Dipole Drives Multi-Centennial Variability in the Western Tropical North Atlantic Margin During the Middle and Late Holocene, Paleoceanog and Paleoclimatol, 36, https://doi.org/10.1029/2020PA004184, 2021.

Thirumalai, K., Richey, J. N., and Quinn, T. M.: Holocene Evolution of Sea-Surface Temperature and Salinity in the Gulf of Mexico, Paleoceanogr Paleoclimatol, 36, https://doi.org/10.1029/2021PA004221, 2021.

Thomas, E. R., Wolff, E. W., Mulvaney, R., Steffensen, J. P., Johnsen, S. J., Arrowsmith, C., White, J. W. C., Vaughn, B., and Popp, T.: The 8.2ka event from Greenland ice cores, Quaternary Science Reviews, 26, 70–81, https://doi.org/10.1016/j.quascirev.2006.07.017, 2007.

Törnqvist, T. E. and Hijma, M. P.: Links between early Holocene ice-sheet decay, sea-level rise and abrupt climate change, Nature Geosci, 5, 601–606, https://doi.org/10.1038/ngeo1536, 2012.

Van Breukelen, M. R., Vonhof, H. B., Hellstrom, J. C., Wester, W. C. G., and Kroon, D.: Fossil dripwater in stalagmites reveals Holocene temperature and rainfall variation in Amazonia, Earth and Planetary Science Letters, 275, 54–60, https://doi.org/10.1016/j.epsl.2008.07.060, 2008.

Voarintsoa, N. R. G., Railsback, L. B., Brook, G. A., Wang, L., Kathayat, G., Cheng, H., Li, X., Edwards, R. L., Rakotondrazafy, A. F. M., and Madison Razanatseheno, M. O.: Three distinct Holocene intervals of stalagmite deposition and nondeposition revealed in NW Madagascar, and their paleoclimate implications, Clim. Past, 13, 1771–1790, https://doi.org/10.5194/cp-13-1771-2017, 2017.

Voarintsoa, N. R. G., Matero, I. S. O., Railsback, L. B., Gregoire, L. J., Tindall, J., Sime, L., Cheng, H., Edwards, R. L., Brook, G. A., Kathayat, G., Li, X., Michel Rakotondrazafy, A. F., and Madison Razanatseheno, M. O.: Investigating the 8.2 ka event in northwestern Madagascar: Insight from data–model comparisons, Quaternary Science Reviews, 204, 172–186, https://doi.org/10.1016/j.quascirev.2018.11.030, 2019.

Wahl, D., Byrne, R., and Anderson, L.: An 8700 year paleoclimate reconstruction from the southern Maya lowlands, Quaternary Science Reviews, 103, 19–25, https://doi.org/10.1016/j.quascirev.2014.08.004, 2014.

Wang, L., Sarnthein, M., Grootes, P. M., and Erlenkeuser, H.: Millennial reoccurrence of century-scale abrupt events of East Asian Monsoon: A possible heat conveyor for the global deglaciation, Paleoceanography, 14, 725–731, https://doi.org/10.1029/1999PA900028, 1999.

Wang, Y., Cheng, H., Edwards, R. L., He, Y., Kong, X., An, Z., Wu, J., Kelly, M. J., Dykoski, C. A., and Li, X.: The Holocene Asian Monsoon: Links to Solar Changes and North Atlantic Climate, Science, 308, 854–857, https://doi.org/10.1126/science.1106296, 2005.

Ward, B. M., Wong, C. I., Novello, V. F., McGee, D., Santos, R. V., Silva, L. C. R., Cruz, F. W., Wang, X., Edwards, R. L., and Cheng, H.: Reconstruction of Holocene coupling between the South American Monsoon System and local moisture variability from speleothem $\delta^{18}O$ and $^{87}Sr/^{86}Sr$ records, Quaternary Science Reviews, 210, 51–63, https://doi.org/10.1016/j.quascirev.2019.02.019, 2019.

Warken, S. F., Scholz, D., Spötl, C., Jochum, K. P., Pajón, J. M., Bahr, A., and Mangini, A.: Caribbean hydroclimate and vegetation history across the last glacial period, Quaternary Science Reviews, 218, 75–90, https://doi.org/10.1016/j.quascirev.2019.06.019, 2019.

Winter, A., Zanchettin, D., Lachniet, M., Vieten, R., Pausata, F. S. R., Ljungqvist, F. C., Cheng, H., Edwards, R. L., Miller, T., Rubinetti, S., Rubino, A., and Taricco, C.: Initiation of a stable convective hydroclimatic regime in Central America circa 9000 years BP, Nature Communications, 11, 716, https://doi.org/10.1038/s41467-020-14490-y, 2020.

Woods, A., Rodbell, D. T., Abbott, M. B., Hatfield, R. G., Chen, C. Y., Lehmann, S. B., McGee, D., Weidhaas, N. C., Tapia, P. M., Valero-Garcés, B. L., Bush, M. B., and Stoner, J. S.: Andean drought and glacial retreat tied to Greenland warming during the last glacial period, Nat Commun, 11, 5135, https://doi.org/10.1038/s41467-020-19000-8, 2020.

Wu, C.-H., Lee, S.-Y., and Chiang, J. C. H.: Relative influence of precession and obliquity in the early Holocene: Topographic modulation of subtropical seasonality during the Asian summer monsoon, Quaternary Science Reviews, 191, 238–255, https://doi.org/10.1016/j.quascirev.2018.05.021, 2018.

Wurtzel, J. B., Abram, N. J., Lewis, S. C., Bajo, P., Hellstrom, J. C., Troitzsch, U., and Heslop, D.: Tropical Indo-Pacific hydroclimate response to North Atlantic forcing during the last deglaciation as recorded by a speleothem from Sumatra, Indonesia, Earth and Planetary Science Letters, 492, 264–278, https://doi.org/10.1016/j.epsl.2018.04.001, 2018.

Yang, X., Yang, H., Wang, B., Huang, L.-J., Shen, C.-C., Edwards, R. L., and Cheng, H.: Early-Holocene monsoon instability and climatic optimum recorded by Chinese stalagmites, The Holocene, 29, 1059–1067, https://doi.org/10.1177/0959683619831433, 2019.

Zhang, H.-L., Yu, K.-F., Zhao, J.-X., Feng, Y.-X., Lin, Y.-S., Zhou, W., and Liu, G.-H.: East Asian Summer Monsoon variations in the past 12.5ka: High-resolution $\delta^{18}O$ record from a precisely dated aragonite stalagmite in central China, Journal of Asian Earth Sciences, 73, 162–175, https://doi.org/10.1016/j.jseaes.2013.04.015, 2013.

Zhang, N. R. and Siegmund, D. O.: A Modified Bayes Information Criterion with Applications to the Analysis of Comparative Genomic Hybridization Data, Biometrics, 63, 22–32, https://doi.org/10.1111/j.1541-0420.2006.00662.x, 2007.

Zhu, J., Liu, Z., Brady, E. C., Otto-Bliesner, B. L., Marcott, S. A., Zhang, J., Wang, X., Nusbaumer, J., Wong, T. E., Jahn, A., and Noone, D.: Investigating the Direct Meltwater Effect in Terrestrial Oxygen-Isotope Paleoclimate Records Using an Isotope-Enabled Earth System Model, Geophys. Res. Lett., 44, https://doi.org/10.1002/2017GL076253, 2017.

980

985

Figures

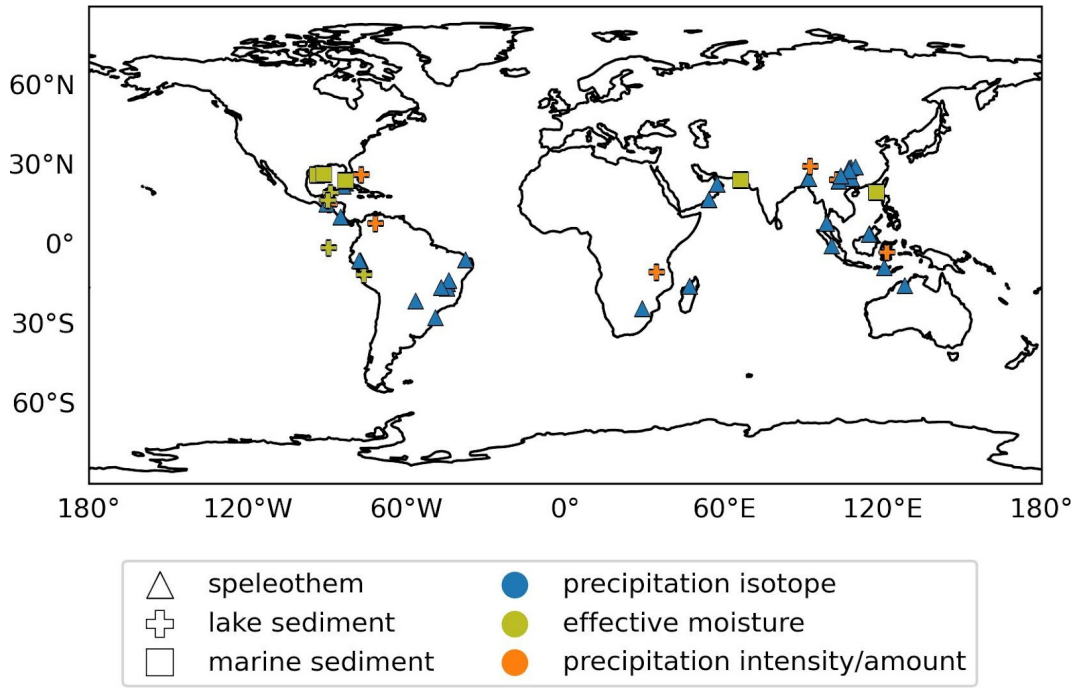

Figure 1. The location of the proxy records comprising each hydroclimate interpretation group included in this study.

990

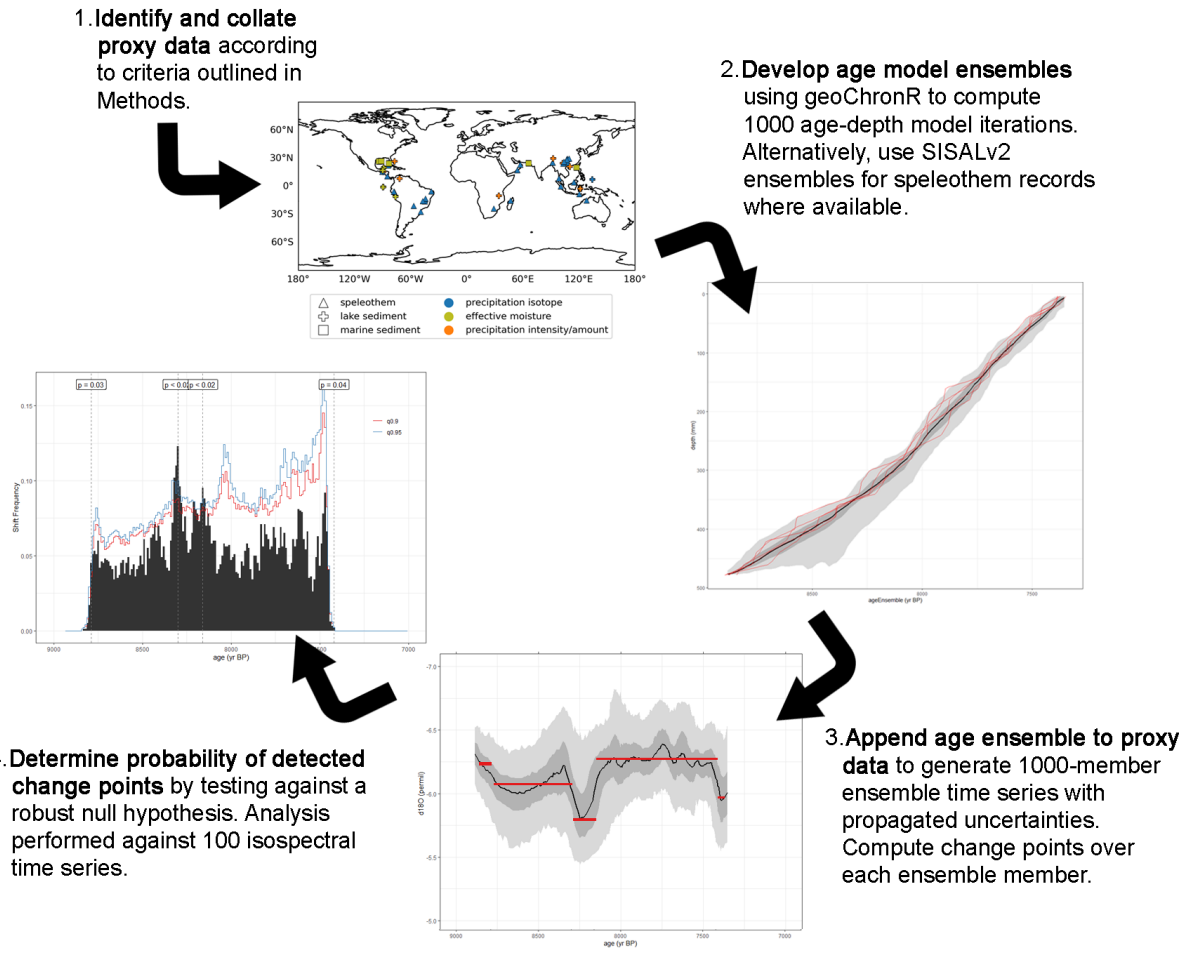

Figure 2. A schematic illustration of the actR analysis process. Step 1: Relevant records are identified and collated into our compilation based on the criteria outlined in the Methods (see Tables 1 and 2). Records are then converted to the LiPD file format for analysis. Step 2: A 1000-member age model ensemble is developed using geoChronR, or, where available for the speleothem records, drawn from the ensembles presented in version 2 of the SISAL database (Comas-Bru et al., 2020). This allows us to propagate age uncertainties through each successive analysis step. Step 3: The resulting 1000-member ensemble time series is then plotted, where at each time step, the median

is represented by the black line, the outermost (lighter) bands represent extreme quantile values (0.025, 0.975) and the innermost (darker) bands the central quantile values (0.25, 0.75). The data are fit to a Gaussian distribution, and the change point analyses are conducted across this ensemble to determine the timing of change points in the proxy data. The red horizontal lines represent the mean proxy values calculated between those points. Step 4: The significance of the detected change points is tested by performing the same ~~change point~~ analyses against 100 isospectral surrogate time series, and the frequency of shifts is plotted as a black histogram summarized in 10-year-long bins. The 90% and 95% confidence intervals are plotted as red and blue ~~light and dark orange~~ lines, respectively, and the p-value is indicated when the frequency of shifts exceeds the 90% confidence interval.

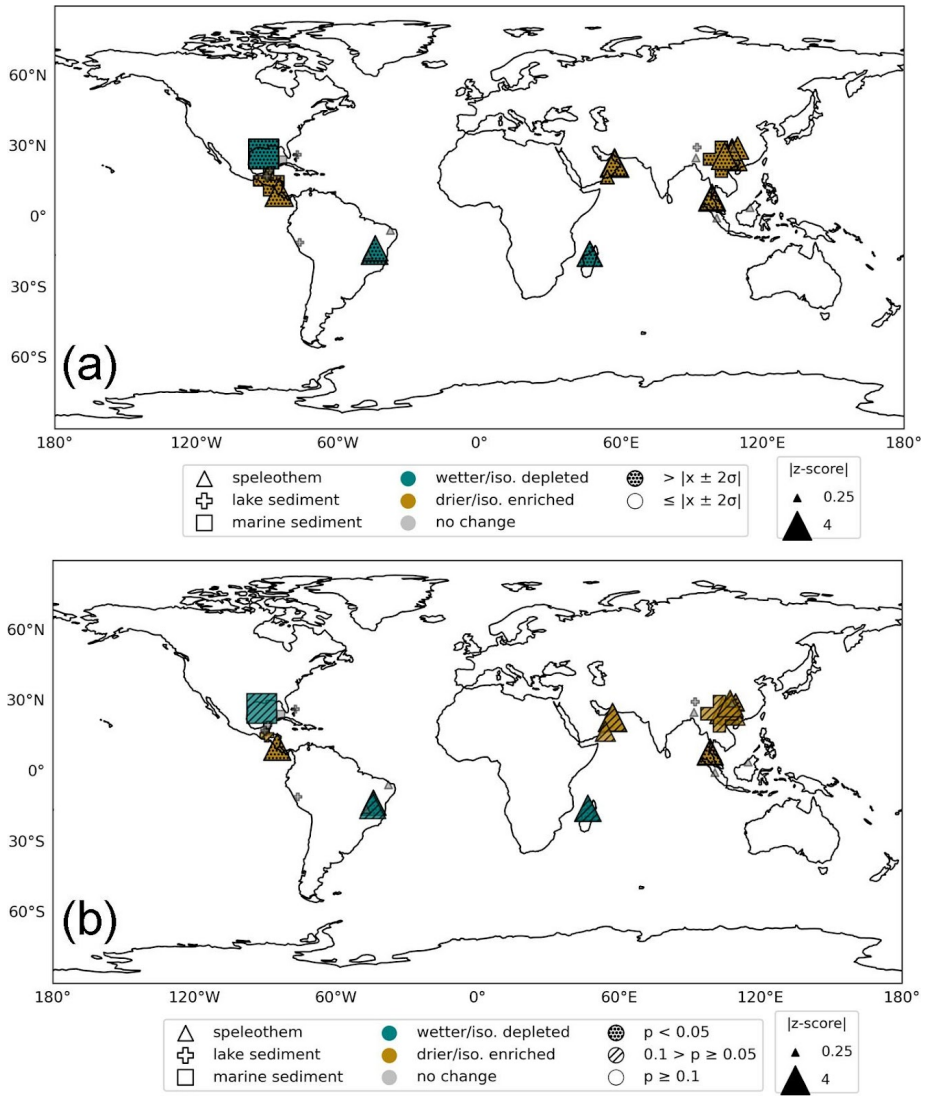

Figure 3. (a) Map of the detected 8.2 ka hydroclimate events using the modified Morrill et al. (2013) method (MM). Blue symbols represent wetter (and/or isotopically depleted) conditions while brown symbols represent drier (and/or isotopically enriched) conditions.

Grey symbols indicate the locations of proxy data where no significant change was detected. Archive type is indicated by the symbol shape, and symbol size is scaled by 250ln(1+|z-score|), calculated from the per-record mean and standard deviation over the 7 ka-10 ka interval. Stippling indicates an event detected over the 7.9 ka-8.5 ka detection window. (b) Same as for (a) but using the actR event detection method. Here, stippling indicates that a "significant" event was detected in each record by actR with event "start" and "end" times within the 7.9 ka-8.3 ka interval at the $p < 0.05$ significance level. Slashed hatching indicates the presence of a "tentative" hydroclimate anomaly, defined by two consecutive changepoints with $p < 0.1$ over an extended 7.7 ka-8.5 ka window (see Methods).

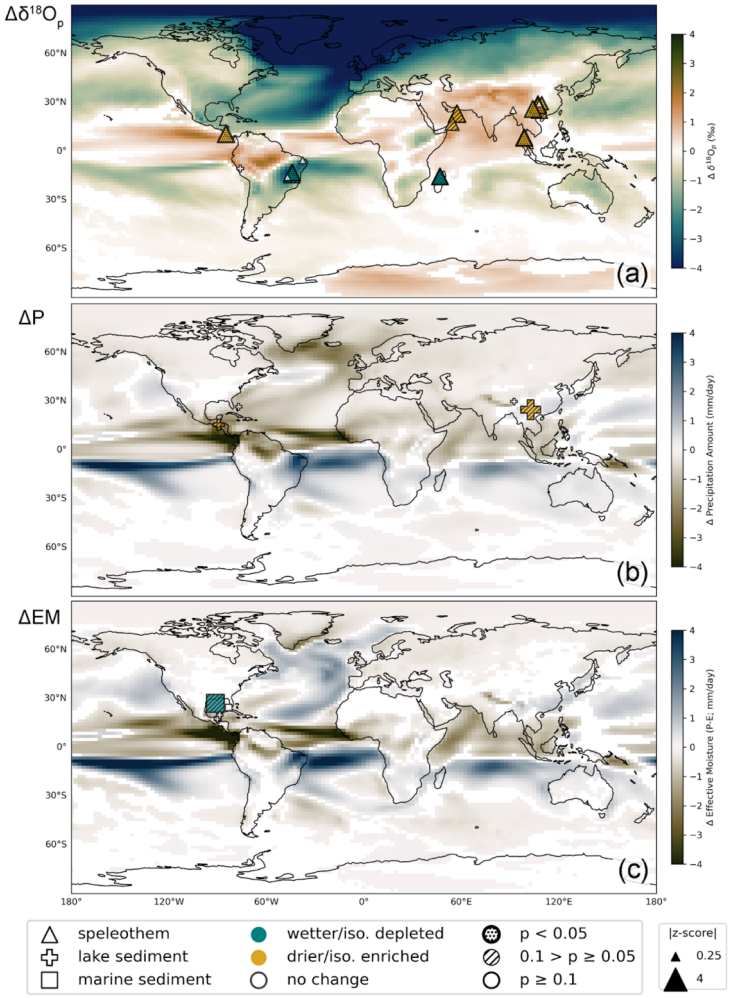

Figure 4. As in Fig. 3b, but with the proxy symbols overlaid on contour maps of the simulated anomalous (a) amount-weighted $\delta^{18}O_p$, (b) precipitation amount, and (c) effective moisture (P-E), calculated from the difference between the last 50 years of the iCESM "hose" and "ctrl" experiments, where only anomalies that exceed the 95% confidence level ($p < 0.05$) are plotted.

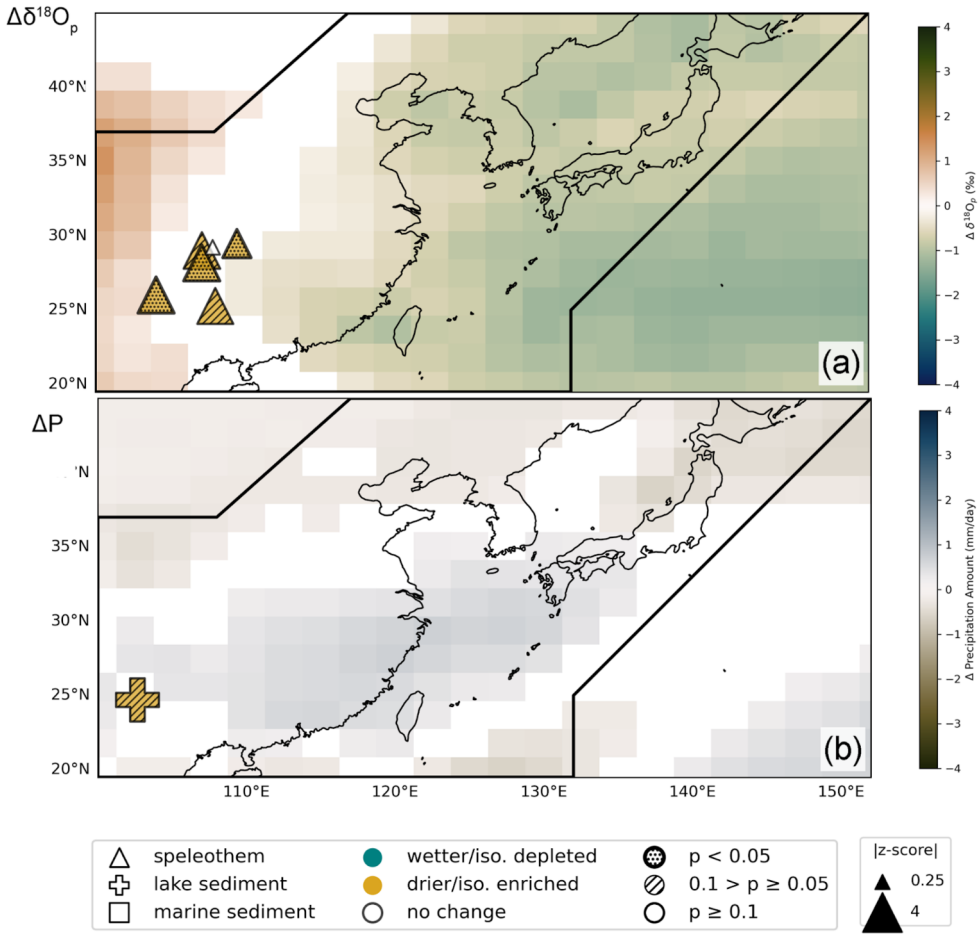

Figure 5. Data-model comparison of IPCC region 35: East Asia (box). Model shading represents (a) the precipitation amount-weighted $\delta^{18}O$ anomaly, and (b) the precipitation amount anomaly between the last 50 years of the "hose" and "ctrl" simulations that exceed the 95% confidence level ($p < 0.05$) using an unpaired two sample Student's t-test. Symbols represent paleoclimate proxy archives within the region corresponding to each respective climate variable, where the brown shaded triangles indicate speleothem records with recorded dry hydroclimate/enriched isotopic anomalies during the 8.2 ka Event and grey symbols indicate records with no hydroclimate anomalies ("no change") over the 7.9 ka-8.3 ka interval. For symbols showing an anomaly associated with the 8.2 ka Event, size is scaled by 400ln(1+|z-score|) relative to each record's mean and standard deviation.

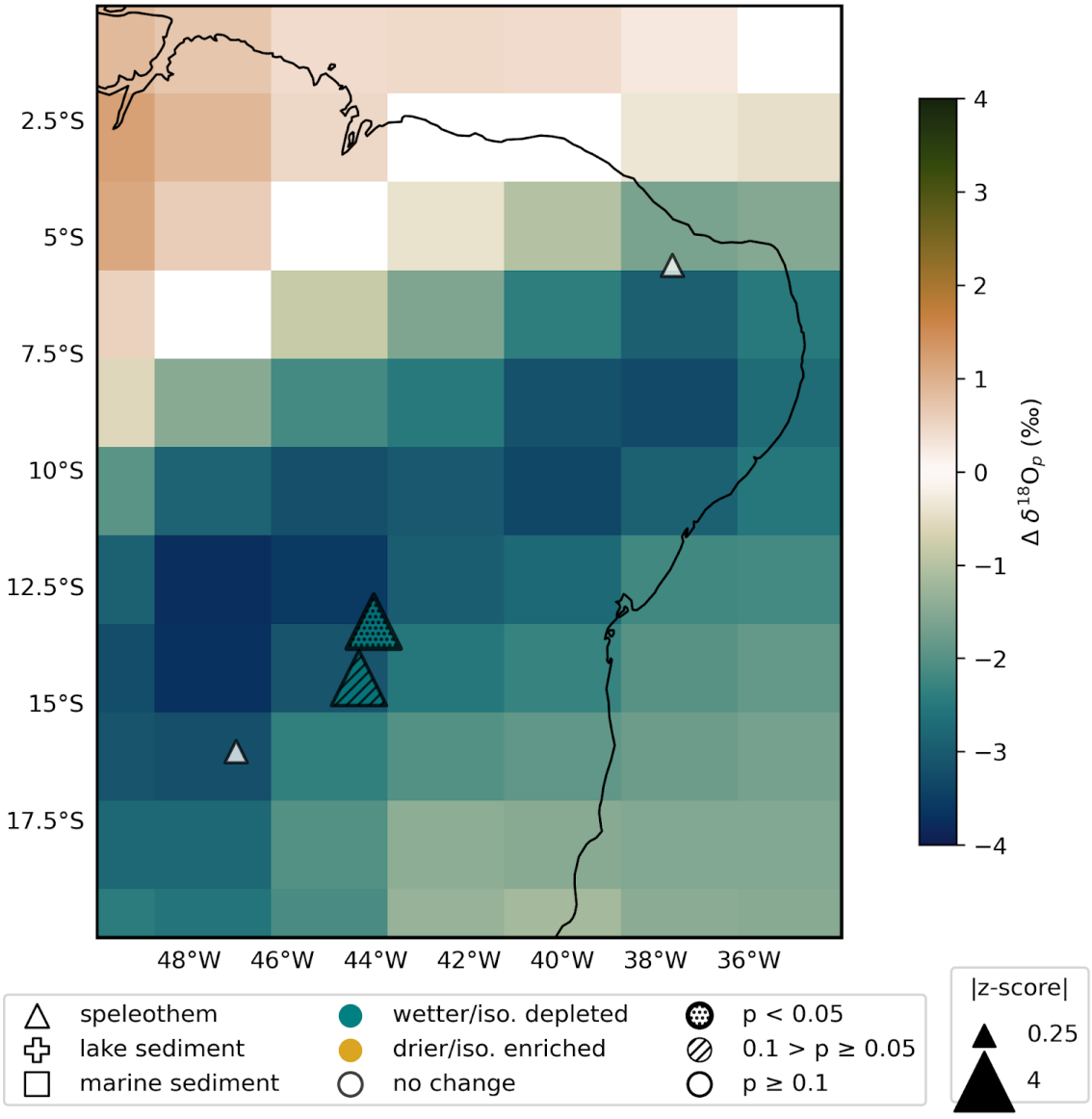

Figure 6. As in Fig. 5, but for IPCC region 11: northeastern South America (box). Model shading represents the precipitation amount-weighted $\delta^{18}O$ anomaly between the last 50 years of the "hose" and "ctrl" simulations.

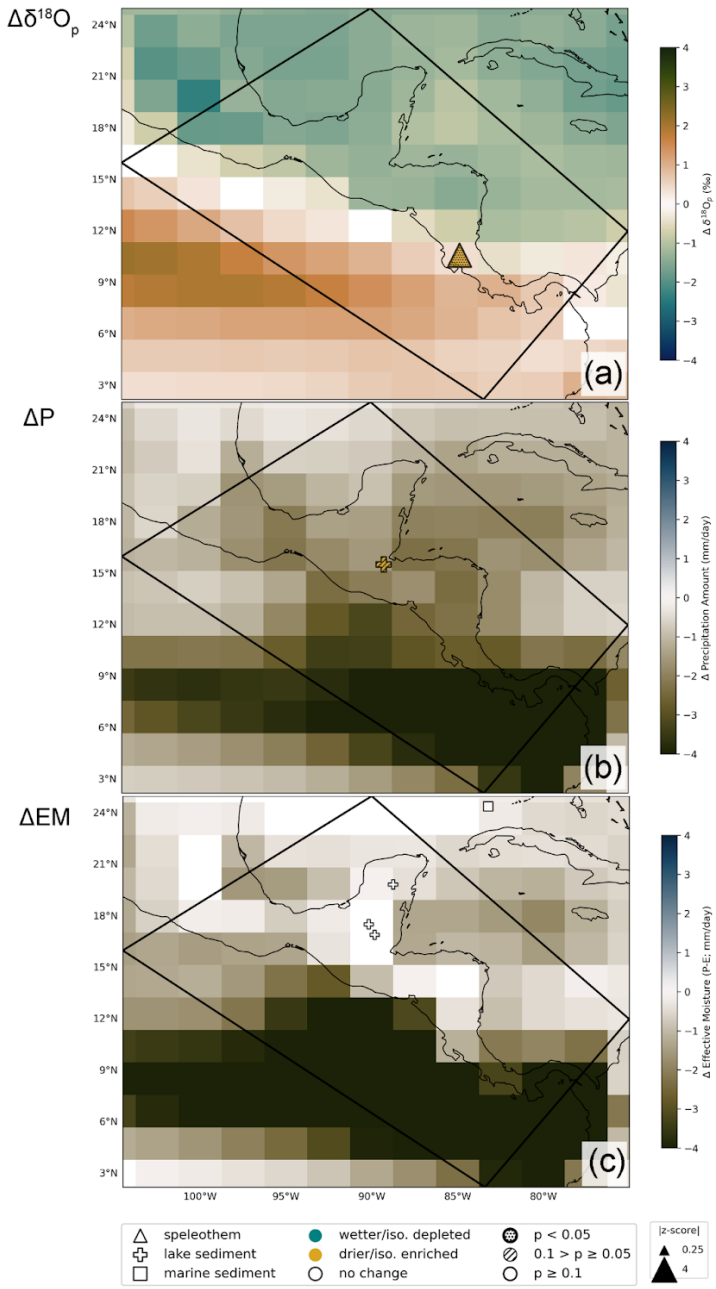

1045

Figure 7. As in Fig. 5, but for IPCC region 7: southern Central America (box), with the addition of (c) the effective moisture (precipitation minus evaporation) anomaly between the last 50 years of the "hose" and "ctrl" simulations.

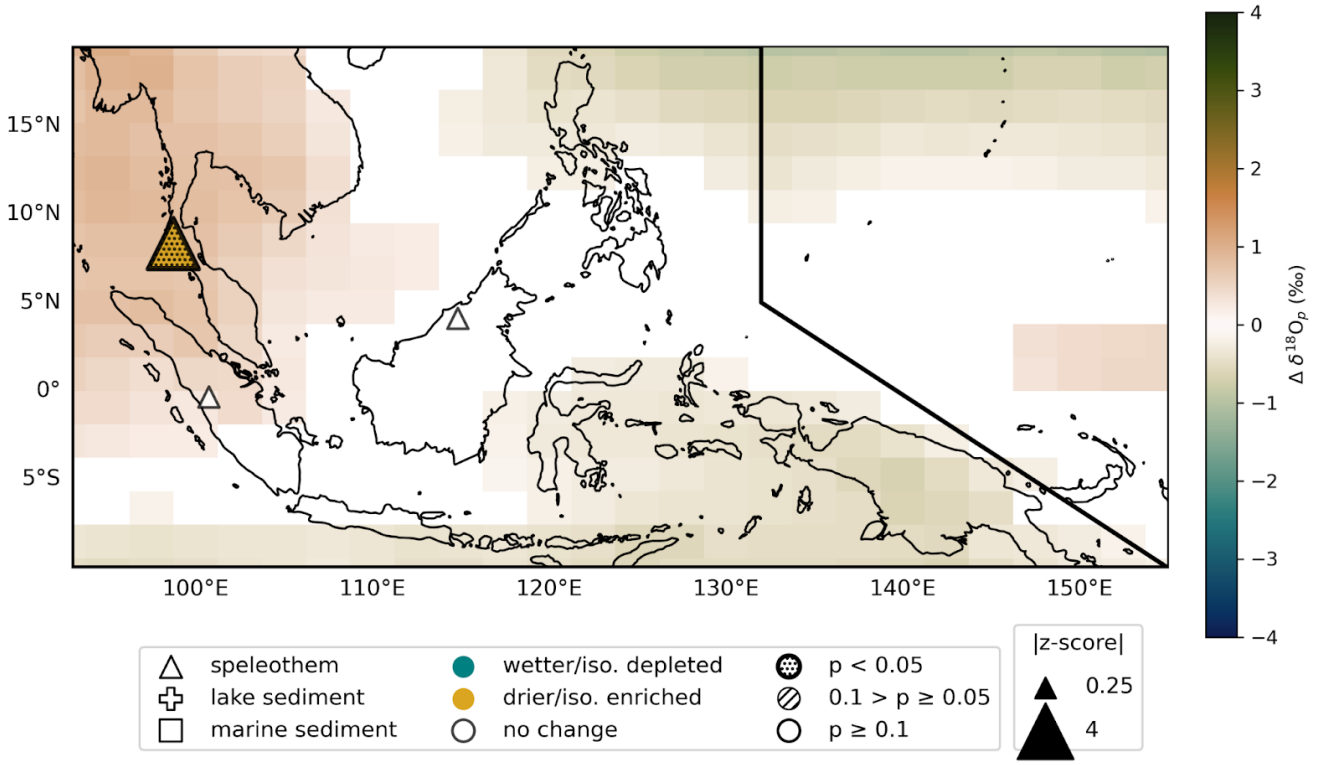

Figure 8. As in Fig. 5, but for IPCC region 38: Southeast Asia (box). Model shading represents the precipitation amount-weighted $\delta^{18}O$ anomaly between the last 50 years of the "hose" and "ctrl" simulations.

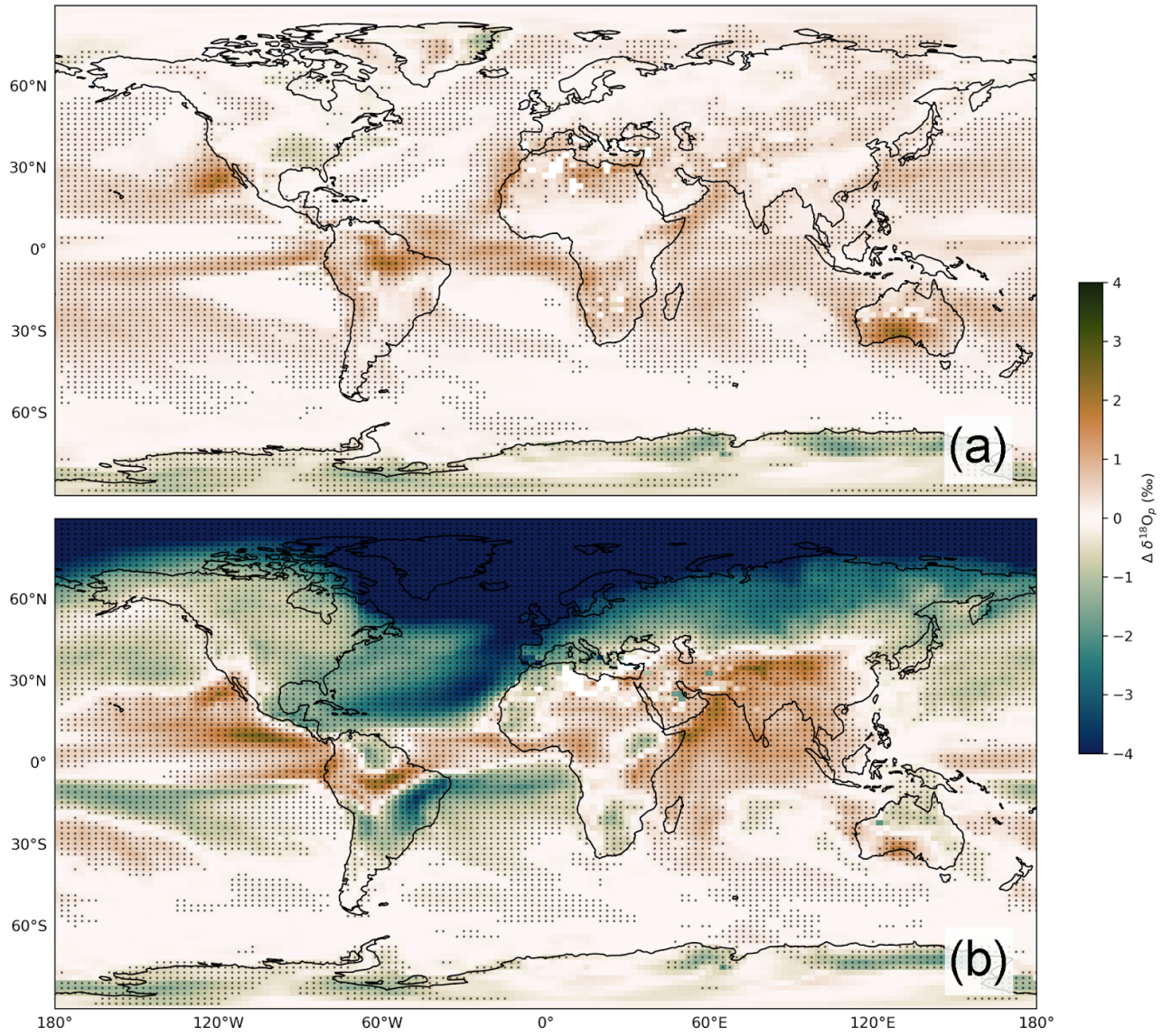

Figure 9. The contribution of (a) the changes in the amount of monthly precipitation and (b) the monthly changes in $\delta^{18}O_p$ to the total change in mean annual amount-weighted $\delta^{18}O_p$ between the last 50 years of the "hose" and "ctrl" simulations. Stippling represents data plotted at the 95% confidence level ($p < 0.05$).

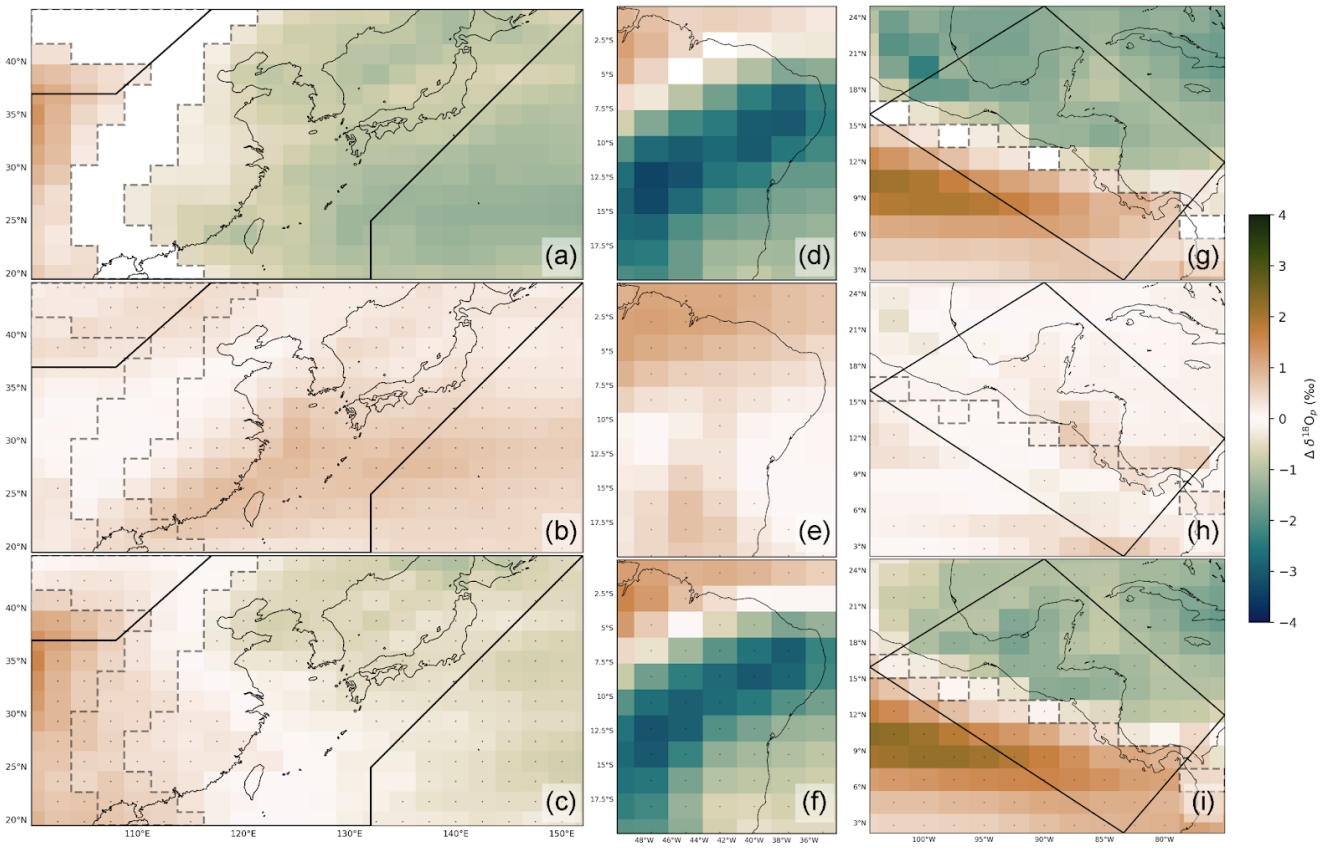

Figure 10. As in Fig. 9, but for East Asia (left column; a,b,c), northeast South America (middle column; d,e,f), and southern Central America (right column; g,h,i). The panels in the upper row show the annual amount-weighted $\delta^{18}O_p$ anomaly of each region, as plotted in Fig. 4a. The panels in the middle and bottom rows depict the same data as in Fig. 9a and b, respectively, at the regional level. The unfilled black polygons (exterior) represent the boundaries of each region defined by the IPCC. The grey dotted lines subdivide East Asia and southern Central America into E-W and N-S subregions defined by the distinct $\pm\Delta\_\delta^{18}O_p$ dipoles shown in panels a and g~~(a) and (g)~~, respectively.

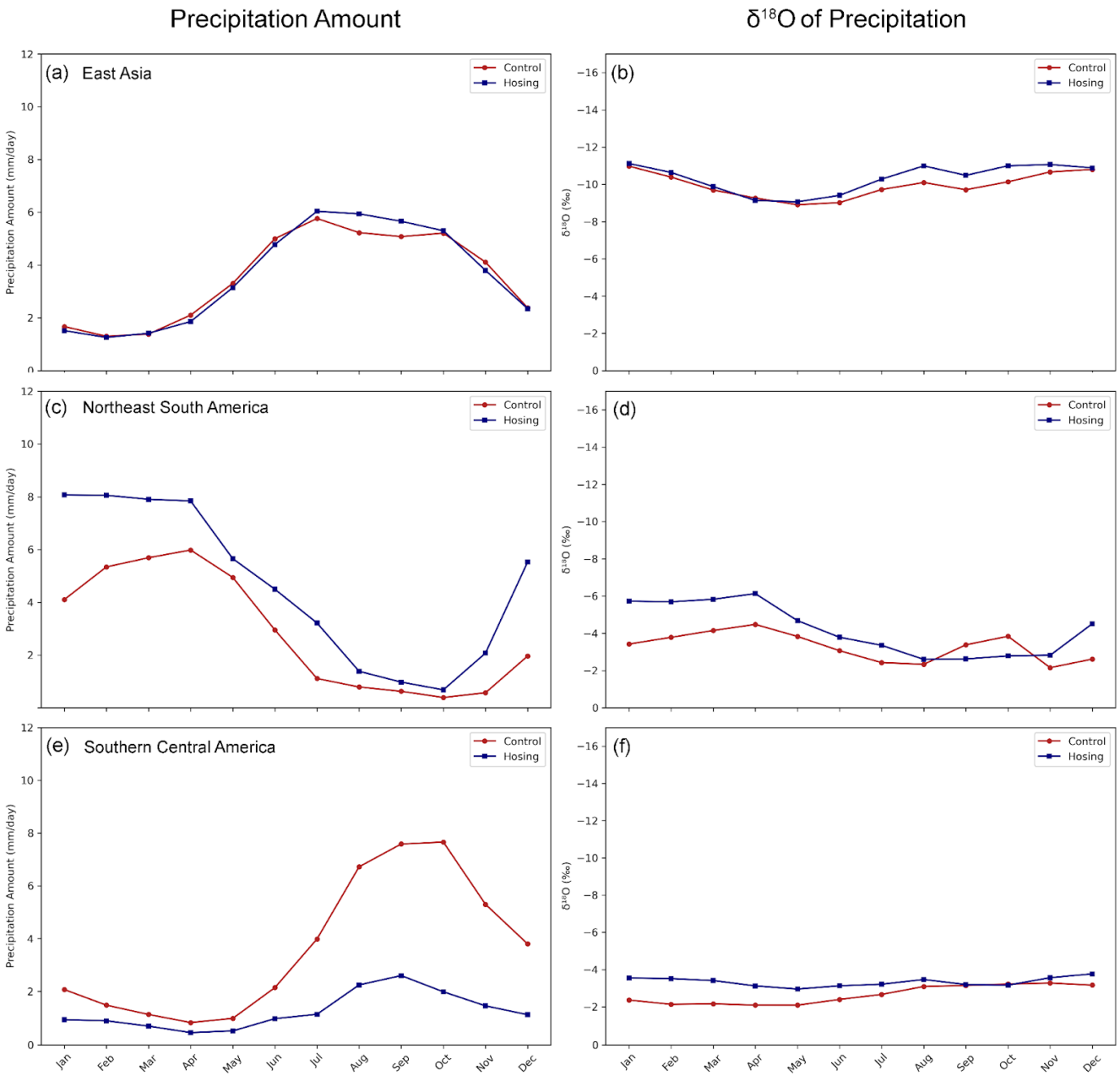

Figure 11. The area-weighted monthly average precipitation amount (left column) and $\delta^{18}O$ of precipitation (not amount-weighted; right column) for the "ctrl" (red) and "hose" (blue) simulations for (a,b) East Asia, (c,d) northeast South America, and (e,f) southern Central America.

1090

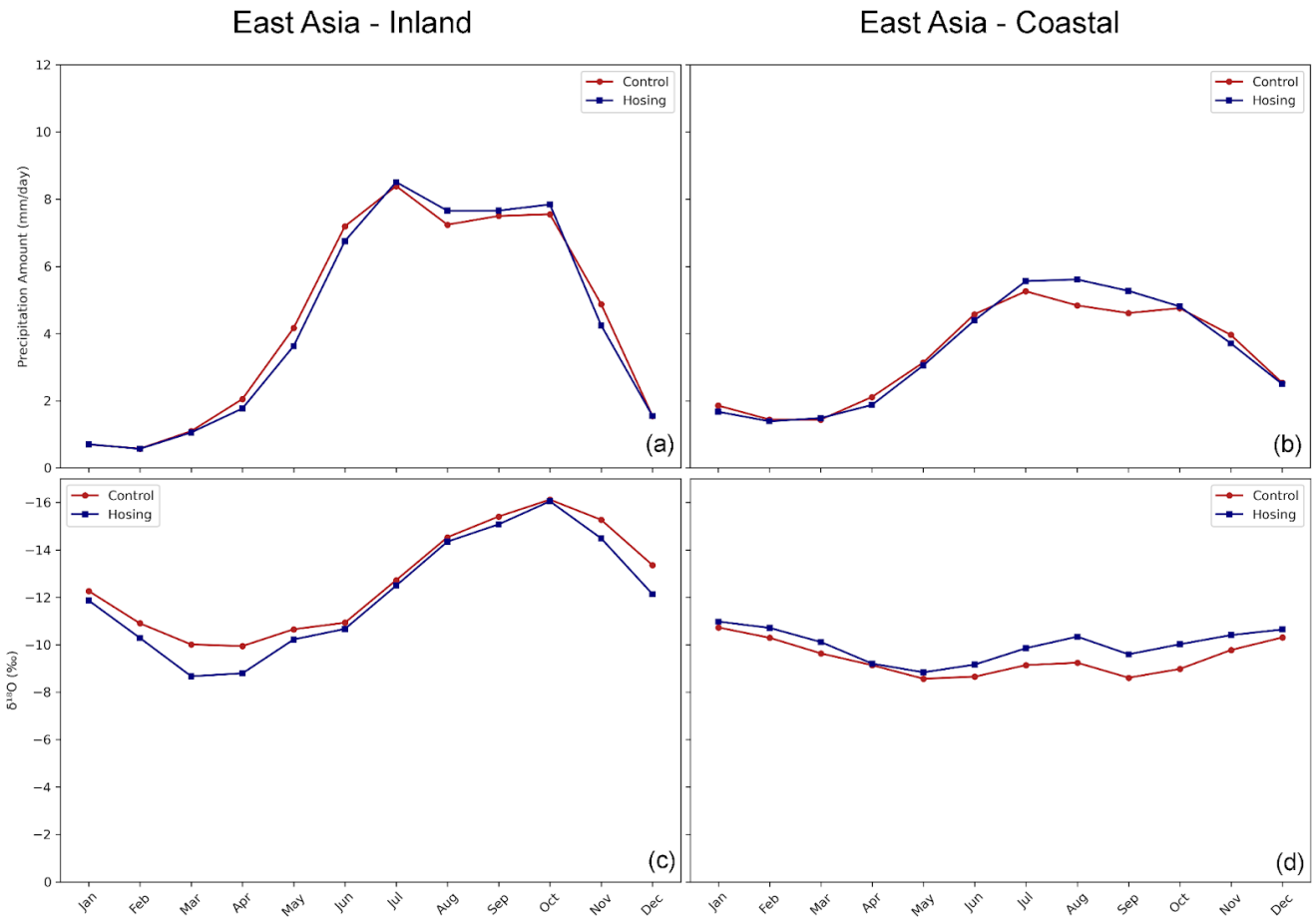

Figure 12. The monthly climatology of the area-weighted precipitation amount (top row) and $\delta^{18}O_p$ (bottom row) for the "ctrl" (red) and "hose" (blue) simulations for East Asia. Data from the western (inland) subregion defined by the positive $\Delta\delta^{18}O_p$ anomaly in Fig. 10a are plotted in the left column. Data from the eastern (coastal) subregion defined by the negative $\Delta\delta^{18}O_p$ anomaly are plotted on the right.

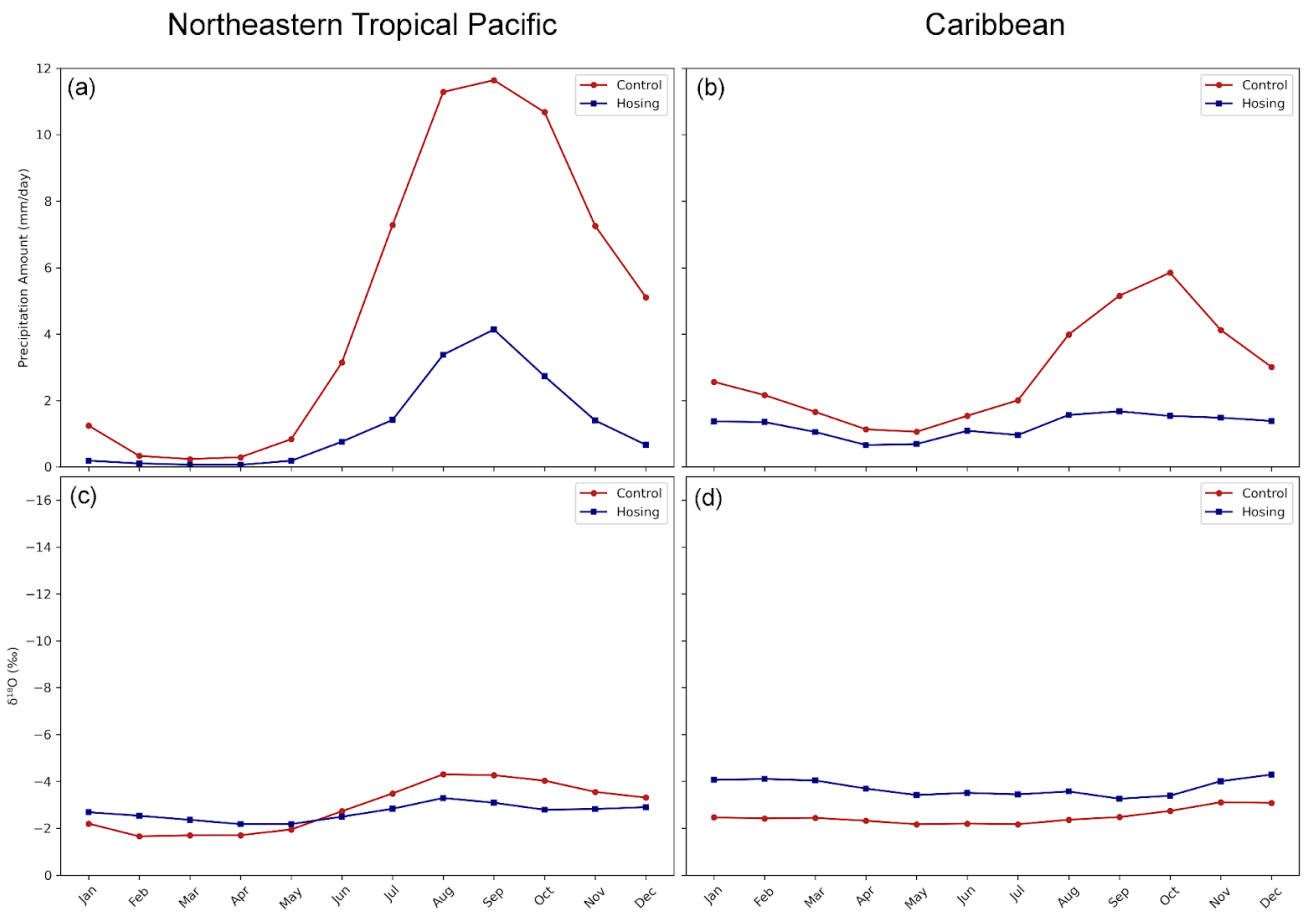

Figure 13. As in Fig. 12, but for Southern Central America. Data from the southern subregion (northeastern tropical Pacific) defined by the positive $\Delta\delta^{18}O_p$ anomaly in Fig. 10g are plotted in the left column, while data from the northern subregion (Caribbean) defined by the negative $\Delta\delta^{18}O_p$ anomaly in Fig. 10g are plotted in the right column.

Tables

Table 1. Location metadata for all paleoclimate proxy datasets in this compilation.

Record ID	Lat	Lon	IPCC Region	Site Name	Reference
ABC1	-15.54	46.89	Madagascar	Anjohibe Cave, Madagascar	Duan et al., 2021
ANJB2	-15.54	46.89	Madagascar	Anjohibe Cave, Madagascar	Voarintsoa et al., 2017
BA03	4.26	114.96	S.E. Asia	Malaysian Borneo	Chen et al., 2016
BTV21a	-27.22	-49.16	S.E. South America	Botuverá Cave, SE Brazil	Bernal et al., 2016
C7	26.57	-77.12	E. North America	Great Cistern Sinkhole, Bahamas	Sullivan et al., 2021
CM2013	22.38	-83.97	Caribbean	Santo Tomas Cave, Cuba	Fensterer et al., 2013
CM2019	23.38	-82.97	Caribbean	Santo Tomas Cave, Cuba	Warken et al., 2019
Core17940	20.12	117.38	E. Asia	South China Sea	Wang et al., 1999
Core5LI	15.53	-89.23	S. Central America	Lake Izabal, Guatemala	Duarte et al., 2021
CP	22.38	-83.97	Caribbean	Dos Anas Cave, Cuba	Fensterer et al., 2013
Curtis6VII93	16.92	-89.83	S. Central America	Lake Peten-Itza, Guatemala	Curtis et al., 1998
D4Cheng	25.28	108.08	E. Asia	Dongge Cave, China	Cheng et al., 2009
D4Dykoski	25.28	108.08	E. Asia	Dongge Cave, China	Dykoski et al., 2005
EJConroy	-0.87	-89.45	Equatorial Pacific Ocean	El Junco Lake, Galapagos	Conroy et al., 2008
F14	24.69	102.67	E. Asia	Dianchi, Yunan, China	Hillman et al., 2021
FR5	29.23	107.9	E. Asia	Furong Cave, China	Li et al., 2011
GB2GC1	26.67	-93.92	C. North America	Garrison Basin, Gulf of Mexico	Thirumalai et al., 2021
GURM1	15.43	-90.28	S. Central America	Grutas del Rey Marcos, Guatemala	Winter et al., 2020
H14	23.08	57.35	Arabian Peninsula	Hoti Cave, Oman	Cheng et al., 2009
H5	23.08	57.35	Arabian Peninsula	Hoti Cave, Oman	Neff et al., 2001
HF01	29.02	107.18	E. Asia	Chongqing, Southwest China	Yang et al., 2019
JAR7	-21.08	-56.58	S.E. South America	Jaragua Cave, Brazil	Novello et al., 2017
JPC51	24.41	-83.22	Caribbean	Florida Straits	Schmidt et al., 2012
KM1	25.26	91.88	S. Asia	Mawmluh Cave	Huguet et al., 2018
KMA	25.26	91.88	S. Asia	Mawmluh cave	Berkelhammer et al., 2012
KN51	-15.18	128.37	N. Australia	Cave KNI-51, Western Australia	Denniston et al., 2013 (a)
LagoPuertoArturo	17.53	-90.18	S. Central America	Lago Puerto Arturo, Maya Lowlands	Wahl et al., 2014
LBA99	8.33	-71.78	N. South America	Laguna Blanca, Venezuelan Andes	Polissar et al., 2013
LC1	19.86	-88.76	S. Central America	Lake Chichancanab, Mexico	Hodell et al., 1995
LG11	-14.42	-44.37	N.E. South America	Lapa Grande Cave, Brazil	Strikis et al., 2011

LH2	29.48	109.53	E. Asia	Lianhua Cave, Hunan, China	Zhang et al., 2013
LP	-10.7	-76.06	N.W. South America	Laguna Pumacocha, Peru	Bird et al., 2011
LR06_B3_2013	-8.53	120.43	S.E. Asia	Liang Luar cave, western Flores, Indonesia	Ayliffe et al., 2013
LSF19	-16.15	-44.6	N.E. South America	Lapa Sem Fim Cave, Brazil	Azevedo et al., 2021
M981P	-10.27	34.32	E. Southern Africa	Lake Malawi, Africa	Johnson et al., 2003
MAW6	25.26	91.82	S. Asia	Mawmluh Cave, India	Lechleitner et al., 2017
MD022550	26.95	-91.35	C. North America	Gulf of Mexico	LoDico et al., 2006
MWS1	25.26	91.88	S. Asia	Mawmluh cave	Dutt et al., 2015
NARC	-5.73	-77.5	N.W. South America	Cueva del Diamante, Peru	Cheng et al., 2013
NCB	-5.94	-77.31	N.W. South America	Cueva del Tigre Perdido, Peru	van Breukelen et al., 2008
PAD07	-13.22	-44.05	N.E. South America	Padre Cave, Brazil	Cheng et al., 2009
ParuCo	29.8	92.35	Tibetan Plateau	Paru Co, Tibetan Plateau, China	Bird et al., 2014
PET-PI6	17	-89.78	S. Central America	Lake Petén Itzá, Guatemala	Escobar et al., 2012
PLJJUN15	-11.04	-76.11	N.W. South America	Lake Junín, Peruvian Andes	Woods et al., 2020
Q52007	17.17	54.3	Arabian Peninsula	Qunf Cave, Oman	Fleitmann et al., 2007
Q5Cheng	17.17	54.3	Arabian Peninsula	Qunf Cave, Oman	Cheng et al., 2009
RN1	-5.58	-37.64	N.E. South America	Rainha cave, Brazil	Cruz et al., 2009
RN4	-5.58	-37.64	N.E. South America	Rainha cave, Brazil	Cruz et al., 2009
SG1	28.18	107.17	E. Asia	Shigao Cave, China	Jiang et al., 2012
Sha3	-5.7	-77.9	N.W. South America	Shatuca Cave, Peruvian Andes	Bustamante et al., 2016
SSC01	4.1	114.83	S.E. Asia	Gunung Mulu National Park, Borneo	Carolin et al., 2016
Staubwasser63KA	24.62	65.98	S. Asia	Arabian Sea	Staubwasser et al., 2003
T8	-24.02	29.11	E. Southern Africa	Makapansgat Valley, South Africa	Holmgren et al., 2003
TA122	-0.35	100.75	S.E. Asia	Tangga Cave, Sumatra	Wurtzel et al., 2018
TK07	8.33	98.73	S.E. Asia	Klang Cave, Thailand	Chawchai et al., 2021
TK20	8.33	98.73	S.E. Asia	Klang Cave, Thailand	Chawchai et al., 2021
TM6	-16	-47	N.E. South America	Tamboril Cave, Brazil	Ward et al., 2019

TOW109B	-2.73	121.52	S.E. Asia	Lake Towuti, Indonesia	Russell et al., 2014
V1	10.6	-84.8	S. Central America	Costa Rica	Lachniet et al., 2004
XBL29	24.2	103.36	E. Asia	Xiaobailong cave, China	Cai et al., 2015
ZLP1	26.02	104.1	E. Asia	Zhuliuping Cave, China	Huang et al., 2016

1120

Tables

Table 1. Location metadata for all paleoclimate proxy datasets in this compilation.

Record ID	Lat	Lon	IPCC Region	Site Name	Reference
ABC1	-15.54	46.89	Madagascar	Anjohibe Cave, Madagascar	Duan et al., 2021
ANJB2	-15.54	46.89	Madagascar	Anjohibe Cave, Madagascar	Voarintsoa et al., 2017
BA03	4.26	114.96	S.E. Asia	Malaysian Borneo	Chen et al., 2016
BTV21a	-27.22	-49.16	S.E. South America	Botuverá Cave, SE Brazil	Bernal et al., 2016
C7	26.57	-77.12	E. North America	Great Cistern Sinkhole, Bahamas	Sullivan et al., 2021
CM2013	22.38	-83.97	Caribbean	Santo Tomas Cave, Cuba	Fensterer et al., 2013
CM2019	23.38	-82.97	Caribbean	Santo Tomas Cave, Cuba	Warken et al., 2019
Core17940	20.12	117.38	E. Asia	South China Sea	Wang et al., 1999
Core5LI	15.53	-89.23	S. Central America	Lake Izabal, Guatemala	Duarte et al., 2021
CP	22.38	-83.97	Caribbean	Dos Anas Cave, Cuba	Fensterer et al., 2013
Curtis6VII93	16.92	-89.83	S. Central America	Lake Peten-Itza, Guatemala	Curtis et al., 1998
D4Cheng	25.28	108.08	E. Asia	Dongge Cave, China	Cheng et al., 2009
D4Dykoski	25.28	108.08	E. Asia	Dongge Cave, China	Dykoski et al., 2005
EJConroy	-0.87	-89.45	Equatorial Pacific Ocean	El Junco Lake, Galapagos	Conroy et al., 2008
F14	24.69	102.67	E. Asia	Dianchi, Yunan, China	Hillman et al., 2021
FR5	29.23	107.9	E. Asia	Furong Cave, China	Li et al., 2011
GB2GC1	26.67	-93.92	C. North America	Garrison Basin, Gulf of Mexico	Thirumalai et al., 2021
GURM1	15.43	-90.28	S. Central America	Grutas del Rey Marcos, Guatemala	Winter et al., 2020
H14	23.08	57.35	Arabian Peninsula	Hoti Cave, Oman	Cheng et al., 2009
H5	23.08	57.35	Arabian Peninsula	Hoti Cave, Oman	Neff et al., 2001

Record ID	Lat	Lon	IPCC Region	Site Name	Reference
HF01	29.02	107.18	E. Asia	Chongqing, Southwest China	Yang et al., 2019
JAR7	-21.08	-56.58	S.E. South America	Jaragua Cave, Brazil	Novello et al., 2017
JPC51	24.41	-83.22	Caribbean	Florida Straits	Schmidt et al., 2012
KM1	25.26	91.88	S. Asia	Mawmluh Cave	Huguet et al., 2018
KMA	25.26	91.88	S. Asia	Mawmluh cave	Berkelhammer et al., 2012
KN51	-15.18	128.37	N. Australia	Cave KNI-51, Western Australia	Denniston et al., 2013 (a)
LagoPuertoArturo	17.53	-90.18	S. Central America	Lago Puerto Arturo, Maya Lowlands	Wahl et al., 2014
LBA99	8.33	-71.78	N. South America	Laguna Blanca, Venezuelan Andes	Polissar et al., 2013
LC1	19.86	-88.76	S. Central America	Lake Chichancanab, Mexico	Hodell et al., 1995
LG11	-14.42	-44.37	N.E. South America	Lapa Grande Cave, Brazil	Strikis et al., 2011
LH2	29.48	109.53	E. Asia	Lianhua Cave, Hunan, China	Zhang et al., 2013
LP	-10.7	-76.06	N.W. South America	Laguna Pumacocha, Peru	Bird et al., 2011
LR06_B3_2013	-8.53	120.43	S.E. Asia	Liang Luar cave, western Flores, Indonesia	Ayliffe et al., 2013
LSF19	-16.15	-44.6	N.E. South America	Lapa Sem Fim Cave, Brazil	Azevedo et al., 2021
M981P	-10.27	34.32	E. Southern Africa	Lake Malawi, Africa	Johnson et al., 2003
MAW6	25.26	91.82	S. Asia	Mawmluh Cave, India	Lechleitner et al., 2017
MD022550	26.95	-91.35	C. North America	Gulf of Mexico	LoDico et al., 2006
MWS1	25.26	91.88	S. Asia	Mawmluh cave	Dutt et al., 2015
NARC	-5.73	-77.5	N.W. South America	Cueva del Diamante, Peru	Cheng et al., 2013
NCB	-5.94	-77.31	N.W. South America	Cueva del Tigre Perdido, Peru	van Breukelen et al., 2008
PAD07	-13.22	-44.05	N.E. South America	Padre Cave, Brazil	Cheng et al., 2009
ParuCo	29.8	92.35	Tibetan Plateau	Paru Co, Tibetan Plateau, China	Bird et al., 2014
PET-PI6	17	-89.78	S. Central America	Lake Petén Itzá, Guatemala	Escobar et al., 2012
PLJJUN15	-11.04	-76.11	N.W. South America	Lake Junín, Peruvian Andes	Woods et al., 2020
Q52007	17.17	54.3	Arabian Peninsula	Qunf Cave, Oman	Fleitmann et al., 2007
Q5Cheng	17.17	54.3	Arabian Peninsula	Qunf Cave, Oman	Cheng et al., 2009
RN1	-5.58	-37.64	N.E. South America	Rainha cave, Brazil	Cruz et al., 2009
RN4	-5.58	-37.64	N.E. South America	Rainha cave, Brazil	Cruz et al., 2009

Record ID	Lat	Lon	IPCC Region	Site Name	Reference
SG1	28.18	107.17	E. Asia	Shigao Cave, China	Jiang et al., 2012
Sha3	-5.7	-77.9	N.W. South America	Shatuca Cave, Peruvian Andes	Bustamante et al., 2016
SSC01	4.1	114.83	S.E. Asia	Gunung Mulu National Park, Borneo	Carolin et al., 2016
Staubwasser63KA	24.62	65.98	S. Asia	Arabian Sea	Staubwasser et al., 2003
T8	-24.02	29.11	E. Southern Africa	Makapansgat Valley, South Africa	Holmgren et al., 2003
TA122	-0.35	100.75	S.E. Asia	Tangga Cave, Sumatra	Wurtzel et al., 2018
TK07	8.33	98.73	S.E. Asia	Klang Cave, Thailand	Chawchai et al., 2021
TK20	8.33	98.73	S.E. Asia	Klang Cave, Thailand	Chawchai et al., 2021
TM6	-16	-47	N.E. South America	Tamboril Cave, Brazil	Ward et al., 2019
TOW109B	-2.73	121.52	S.E. Asia	Lake Towuti, Indonesia	Russell et al., 2014
V1	10.6	-84.8	S. Central America	Costa Rica	Lachniet et al., 2004
XBL29	24.2	103.36	E. Asia	Xiaobailong cave, China	Cai et al., 2015
ZLP1	26.02	104.1	E. Asia	Zhuliuping Cave, China	Huang et al., 2016

Table 2. Archive and interpretation metadata for the paleoclimate proxy datasets used in this study. Tier 1 data meet all strict inclusion criteria, while Tier 2 data are deficient in either dating or data resolution over the 7ka-10ka interval. Tier 3 data meet none of the strict inclusion criteria and are not included in quantitative analyses. All foraminifera used in the compilation are G. ruber (white). BSi MAR is the biogenic silica mass accumulation rate, in mg $SiO_2 cm^{-2} yr^{-1}$.

Record ID	Tier	Archive	Proxy	Interp. Group	Interp. Dir.	Reference
ABC1	1	speleothem	$\delta^{18}O$	P_{iso}	inverse	Duan et al., 2021
ANJB2	1	speleothem	$\delta^{18}O$	P_{iso}	inverse	Voarintsoa et al., 2017
BA03	1	speleothem	$\delta^{18}O$	P_{iso}	inverse	Chen et al., 2016
BTV21a	1	speleothem	$\delta^{18}O$	P_{iso}	inverse	Bernal et al., 2016
C7	2	lacustrine	grain size	P_{amt}	direct	Sullivan et al., 2021
CM2013	1	speleothem	$\delta^{18}O$	P_{iso}	inverse	Fensterer et al., 2013
CM2019	1	speleothem	$\delta^{18}O$	P_{iso}	inverse	Warken et al., 2019
Core17940	1	marine	$\delta^{18}O$	EM	inverse	Wang et al., 1999
Core5LI	1	lacustrine	Ti	P_{amt}	direct	Duarte et al., 2021
CP	1	speleothem	$\delta^{18}O$	P_{iso}	inverse	Fensterer et al., 2013
Curtis6VII93	2	lacustrine	$\delta^{18}O_{gastro}$ (Cochliopina sp.)	EM	inverse	Curtis et al., 1998
D4Cheng	1	speleothem	$\delta^{18}O$	P_{iso}	inverse	Cheng et al., 2009
D4Dykoski	1	speleothem	$\delta^{18}O$	P_{iso}	inverse	Dykoski et al., 2005
EJConroy	1	lacustrine	clay (%)	EM	direct	Conroy et al., 2008
F14	2	lacustrine	magnetic susceptibility	P_{amt}	inverse	Hillman et al., 2021
FR5	2	speleothem	$\delta^{18}O$	P_{iso}	inverse	Li et al., 2011
GB2GC1	1	marine	$\delta^{18}O$	EM	inverse	Thirumalai et al., 2021
GURM1	1	speleothem	$\delta^{18}O$	P_{iso}	inverse	Winter et al., 2020
H14	1	speleothem	$\delta^{18}O$	P_{iso}	inverse	Cheng et al., 2009
H5	1	speleothem	$\delta^{18}O$	P_{iso}	inverse	Neff et al., 2001
HF01	1	speleothem	$\delta^{18}O$	P_{iso}	inverse	Yang et al., 2019

JAR7	1	speleothem	$\delta^{18}O$	P_{iso}	inverse	Novello et al., 2017
JPC51	1	marine	$\delta^{18}O$	EM	inverse	Schmidt et al., 2012
KM1	1	speleothem	$\delta^{18}O$	P_{iso}	inverse	Huguet et al., 2018
KMA	1	speleothem	$\delta^{18}O$	P_{iso}	inverse	Berkelhammer et al., 2012
KN51	1	speleothem	$\delta^{18}O$	P_{iso}	inverse	Denniston et al., 2013 (a)
LagoPuertoArturo	1	lacustrine	$\delta^{18}O$	EM	inverse	Wahl et al., 2014
LBA99	1	lacustrine	magnetic susceptibility	P_{amt}	direct	Polissar et al., 2013
LC1	1	lacustrine	$CaCO_3$	EM	direct	Hodell et al., 1995
LG11	1	speleothem	$\delta^{18}O$	P_{iso}	inverse	Strikis et al., 2011
LH2	1	speleothem	$\delta^{18}O$	P_{iso}	inverse	Zhang et al., 2013
LP	2	lacustrine	$\delta^{18}O$	P_{iso}	inverse	Bird et al., 2011
LR06_B3_2013	1	speleothem	$\delta^{18}O$	P_{iso}	inverse	Ayliffe et al., 2013
LSF19	1	speleothem	$\delta^{18}O$	P_{iso}	inverse	Azevedo et al., 2021
M981P	2	lacustrine	BSi MAR	P_{amt}	direct	Johnson et al., 2003
MAW6	1	speleothem	$\delta^{18}O$	P_{iso}	inverse	Lechleitner et al., 2017
MD022550	1	marine	$\delta^{18}O$	EM	inverse	LoDico et al., 2006
MWS1	3	speleothem	$\delta^{18}O$	P_{iso}	inverse	Dutt et al., 2015
NARC	1	speleothem	$\delta^{18}O$	P_{iso}	inverse	Cheng et al., 2013
NCB	2	speleothem	$\delta^{18}O$	P_{iso}	inverse	van Breukelen et al., 2008
PAD07	1	speleothem	$\delta^{18}O$	P_{iso}	inverse	Cheng et al., 2009
ParuCo	2	lacustrine	Lithics (%)	P_{amt}	direct	Bird et al., 2014
PET-PI6	1	lacustrine	magnetic susceptibility	EM	direct	Escobar et al., 2012
PLJJUN15	1	lacustrine	Ti	EM	direct	Woods et al., 2020
Q52007	1	speleothem	$\delta^{18}O$	P_{iso}	inverse	Fleitmann et al., 2007
Q5Cheng	1	speleothem	$\delta^{18}O$	P_{iso}	inverse	Cheng et al., 2009
RN1	1	speleothem	$\delta^{18}O$	P_{iso}	inverse	Cruz et al., 2009
RN4	1	speleothem	$\delta^{18}O$	P_{iso}	inverse	Cruz et al., 2009
SG1	1	speleothem	$\delta^{18}O$	P_{iso}	inverse	Jiang et al., 2012
Sha3	1	speleothem	$\delta^{18}O$	P_{iso}	inverse	Bustamante et al., 2016
SSC01	1	speleothem	$\delta^{18}O$	P_{iso}	inverse	Carolin et al., 2016
Staubwasser63KA	1	marine	$\delta^{18}O_{foram}$	EM	inverse	Staubwasser et al., 2003
T8	1	speleothem	$\delta^{18}O$	P_{iso}	direct	Holmgren et al., 2003
TA122	1	speleothem	$\delta^{18}O$	P_{iso}	inverse	Wurtzel et al., 2018
TK07	1	speleothem	$\delta^{18}O$	P_{iso}	inverse	Chawchai et al., 2021
TK20	1	speleothem	$\delta^{18}O$	P_{iso}	inverse	Chawchai et al., 2021
TM6	1	speleothem	$\delta^{18}O$	P_{iso}	inverse	Ward et al., 2019

TOW109B	2	lacustrine	Ti (cps)	P_{amt}	direct	Russell et al., 2014
V1	1	speleothem	$\delta^{18}O$	P_{iso}	inverse	Lachniet et al., 2004
XBL29	2	speleothem	$\delta^{18}O$	P_{iso}	inverse	Cai et al., 2015
ZLP1	1	speleothem	$\delta^{18}O$	P_{iso}	inverse	Huang et al., 2016

Table 2. Archive and interpretation metadata for the paleoclimate proxy datasets used in this study. Tier 1 data meet all strict inclusion criteria, while Tier 2 data are deficient in either dating or data resolution over the 7ka-10ka interval. Tier 3 data meet none of the strict inclusion criteria and are not included in quantitative analyses. All foraminifera used in the compilation are G. ruber (white). BSi MAR is the biogenic silica mass accumulation rate, in mg $SiO_2 cm^{-2} yr^{-1}$.

Record ID	Tier	Archive	Proxy	Interp. Group	Interp. Dir.	Reference
ABC1	1	speleothem	$\delta^{18}O$	P_{iso}	inverse	Duan et al., 2021
ANJB2	1	speleothem	$\delta^{18}O$	P_{iso}	inverse	Voarintsoa et al., 2017
BA03	1	speleothem	$\delta^{18}O$	P_{iso}	inverse	Chen et al., 2016
BTV21a	1	speleothem	$\delta^{18}O$	P_{iso}	inverse	Bernal et al., 2016
C7	2	lacustrine	grain-size	P_{amt}	direct	Sullivan et al., 2021
CM2013	1	speleothem	$\delta^{18}O$	P_{iso}	inverse	Fensterer et al., 2013
CM2019	1	speleothem	$\delta^{18}O$	P_{iso}	inverse	Warken et al., 2019
Core17940	1	marine	$\delta^{18}O$	EM	inverse	Wang et al., 1999
Core5LI	1	lacustrine	Ti	P_{amt}	direct	Duarte et al., 2021
CP	1	speleothem	$\delta^{18}O$	P_{iso}	inverse	Fensterer et al., 2013
Curtis6VII93	2	lacustrine	$\delta^{18}O_{gastro}$ (Cochliopina sp.)	EM	inverse	Curtis et al., 1998
D4Cheng	1	speleothem	$\delta^{18}O$	P_{iso}	inverse	Cheng et al., 2009
D4Dykoski	1	speleothem	$\delta^{18}O$	P_{iso}	inverse	Dykoski et al., 2005
EJConroy	1	lacustrine	clay (%)	EM	direct	Conroy et al., 2008
F14	2	lacustrine	magnetic susceptibility	P_{amt}	inverse	Hillman et al., 2021
FR5	2	speleothem	$\delta^{18}O$	P_{iso}	inverse	Li et al., 2011
GB2GC1	1	marine	$\delta^{18}O$	EM	inverse	Thirumalai et al., 2021
GURM1	1	speleothem	$\delta^{18}O$	P_{iso}	inverse	Winter et al., 2020
H14	1	speleothem	$\delta^{18}O$	P_{iso}	inverse	Cheng et al., 2009
H5	1	speleothem	$\delta^{18}O$	P_{iso}	inverse	Neff et al., 2001
HF01	1	speleothem	$\delta^{18}O$	P_{iso}	inverse	Yang et al., 2019
JAR7	1	speleothem	$\delta^{18}O$	P_{iso}	inverse	Novello et al., 2017

Record ID	Tier	Archive	Proxy	Interp. Group	Interp. Dir.	Reference
JPC51	1	marine	$\delta^{18}O$	EM	inverse	Schmidt et al., 2012
KM1	1	speleothem	$\delta^{18}O$	P_{ann}	inverse	Huguet et al., 2018
KMA	1	speleothem	$\delta^{18}O$	P_{ann}	inverse	Berkelhammer et al., 2012
KN51	1	speleothem	$\delta^{18}O$	P_{ann}	inverse	Denniston et al., 2013 (a)
LagoPuertoArturo	1	lacustrine	$\delta^{18}O$	EM	inverse	Wahl et al., 2014
LBA99	1	lacustrine	magnetic susceptibility	P_{ann}	direct	Polissar et al., 2013
LC1	1	lacustrine	$CaCO_3$	EM	direct	Hodell et al., 1995
LG11	1	speleothem	$\delta^{18}O$	P_{ann}	inverse	Strikis et al., 2011
LH2	1	speleothem	$\delta^{18}O$	P_{ann}	inverse	Zhang et al., 2013
LP	2	lacustrine	$\delta^{18}O$	P_{ann}	inverse	Bird et al., 2011
LR06_B3_2013	1	speleothem	$\delta^{18}O$	P_{ann}	inverse	Ayliffe et al., 2013
LSF19	1	speleothem	$\delta^{18}O$	P_{ann}	inverse	Azevedo et al., 2021
M981P	2	lacustrine	BSi MAR	P_{ann}	direct	Johnson et al., 2003
MAW6	1	speleothem	$\delta^{18}O$	P_{ann}	inverse	Lechleitner et al., 2017
MD022550	1	marine	$\delta^{18}O$	EM	inverse	LoDico et al., 2006
MWS1	3	speleothem	$\delta^{18}O$	P_{ann}	inverse	Dutt et al., 2015
NARC	1	speleothem	$\delta^{18}O$	P_{ann}	inverse	Cheng et al., 2013
NCB	2	speleothem	$\delta^{18}O$	P_{ann}	inverse	van Breukelen et al., 2008
PAD07	1	speleothem	$\delta^{18}O$	P_{ann}	inverse	Cheng et al., 2009
ParuCo	2	lacustrine	Lithics (%)	P_{ann}	direct	Bird et al., 2014
PET-PI6	1	lacustrine	magnetic susceptibility	EM	direct	Escobar et al., 2012
PLJJUN15	1	lacustrine	Ti	EM	direct	Woods et al., 2020
Q52007	1	speleothem	$\delta^{18}O$	P_{ann}	inverse	Fleitmann et al., 2007
Q5Cheng	1	speleothem	$\delta^{18}O$	P_{ann}	inverse	Cheng et al., 2009
RN1	1	speleothem	$\delta^{18}O$	P_{ann}	inverse	Cruz et al., 2009
RN4	1	speleothem	$\delta^{18}O$	P_{ann}	inverse	Cruz et al., 2009
SG1	1	speleothem	$\delta^{18}O$	P_{ann}	inverse	Jiang et al., 2012
Sha3	1	speleothem	$\delta^{18}O$	P_{ann}	inverse	Bustamante et al., 2016
SSC01	1	speleothem	$\delta^{18}O$	P_{ann}	inverse	Carolin et al., 2016
Staubwasser63KA	1	marine	$\delta^{18}O_{foram}$	EM	inverse	Staubwasser et al., 2003
T8	1	speleothem	$\delta^{18}O$	P_{ann}	direct	Holmgren et al., 2003
TA122	1	speleothem	$\delta^{18}O$	P_{ann}	inverse	Wurtzel et al., 2018

Record ID	Tier	Archive	Proxy	Interp. Group	Interp. Dir.	Reference
TK07	1	speleothem	$\delta^{18}O$	P_{ann}	inverse	Chawchai et al., 2021
TK20	1	speleothem	$\delta^{18}O$	P_{ann}	inverse	Chawchai et al., 2021
TM6	1	speleothem	$\delta^{18}O$	P_{ann}	inverse	Ward et al., 2019
TOW109B	2	lacustrine	Ti (cps)	P_{ann}	direct	Russell et al., 2014
V1	1	speleothem	$\delta^{18}O$	P_{ann}	inverse	Lachniet et al., 2004
XBL29	2	speleothem	$\delta^{18}O$	P_{ann}	inverse	Cai et al., 2015
ZLP1	1	speleothem	$\delta^{18}O$	P_{ann}	inverse	Huang et al., 2016

Table 3. Start, end, and duration of the 8.2 ka Event in the global compilation and the four regions discussed in this study.

Region	Statistic	Event Start (yr BP)	Event End (yr BP)	Event Duration (yrs)
Global	*n = 18*			
	Average	8282	8130	152
	Median	8283	8105	133
	Min	8106	8029	50
	Max	8489	8337	289
	SD	116	85	70
East Asia	*n = 6*			
	Average	8284	8133	151
	Median	8306	8071	139
	Min	8106	8044	62
	Max	8489	8337	259
	SD	138	117	75
Southeast Asia	*n = 2*			
	Average	8291	8176	116
	Median	8291	8176	116
	Min	8285	8155	101
	Max	8297	8196	130
	SD	8	29	21
Northeast South America	*n = 2*			
	Average	8329	8204	125
	Median	8329	8204	125
	Min	8215	8165	50
	Max	8442	8242	200

	SD	161	54	106
South Central America	*n = 2*			
	Average	8175	8069	106
	Median	8175	8069	106
	Min	8163	8051	77
	Max	8186	8086	135
	SD	16	25	41

Table 4. Regional and global summary of 8.2 ka events detected by actR and our MM classification methods, separated by the sign of the anomaly ("wetter", "drier", and "no change").

IPCC Region	wetter	drier	no change	% of regional records w/ agreed "events"	"significant"actR events	"tentative" actR events	no actR events
Madagascar	2	0	0	100	1	1	0
S.E.Asia	0	2	1	43	2	1	4
S.E.South-America	0	0	0	0	0	2	0
E.North-America	0	0	1	100	0	0	1
Caribbean	0	0	1	25	0	3	1
E.Asia	0	6	1	70	4	4	2
S.Central-America	0	2	3	71	1	1	5
Equatorial.Pacific-Ocean	0	0	0	0	0	0	1
C.North-America	1	0	0	50	1	1	0
Arabian-Peninsula	0	3	0	75	1	3	0
S.Asia	0	0	1	20	0	4	1
N.Australia	0	0	0	0	1	0	0
N.South-America	0	0	0	0	1	0	0
N.E.South-America	2	0	2	67	1	2	3
N.W.South-America	0	0	1	20	1	2	2
E.Southern-Africa	0	0	0	0	2	0	0
Tibetan-Plateau	0	0	1	100	0	0	1
Global	5	13	12	-	16	24	21

1170

Table 5. The timing, duration, magnitude, and interpretation of the 8.2ka Event for records with agreement between MM and actR methods.

IPCC Region	Record ID	Event Start (yr BP)	Event End (yr BP)	Event Duration (yrs)	MM z-score	actR z-score	Interpretation
Madagascar	ABC1	8248	8029	219	-2.5	-2.5	wetter/depleted
	ANJB2	8318	8124	194	-2.7	-3.0	wetter/depleted
E.Asia	D4Dykoski	8106	8044	62	2.8	2.8	drier/enriched
	F14	8489	8337	152	5.5	5.8	drier/enriched
	FR5	N/A	N/A	N/A	N/A	N/A	N/A
	LH2	8158	8068	90	2.1	1.3	drier/enriched
	HF01	8332	8073	259	1.8	3.0	drier/enriched
	ZLP1	8339	8213	126	3.0	2.9	drier/enriched
	SG1	8280	8062	218	1.5	2.9	drier/enriched
Arabian-Peninsula	H14	8208	8080	128	3.5	3.5	drier/enriched
	H5	8135	8042	93	2.9	3.2	drier/enriched
	Q52007	8407	8199	208	0.8	1.7	drier/enriched
Tibetan-Plateau	ParuCo	N/A	N/A	N/A	N/A	N/A	N/A
S.Asia	KMA	N/A	N/A	N/A	N/A	N/A	N/A
S.E.Asia	SSC01	N/A	N/A	N/A	N/A	N/A	N/A
	TK07	8297	8196	101	3.1	2.9	drier/enriched
	TK20	8285	8155	130	2.5	2.5	drier/enriched
Caribbean	JPC51	N/A	N/A	N/A	N/A	N/A	N/A
C.North-America	MD022550	8469	8180	289	-3.8	-3.8	wetter/depleted
E.North-America	C7	N/A	N/A	N/A	N/A	N/A	N/A
S.Central-America	LC1	N/A	N/A	N/A	N/A	N/A	N/A
	V1	8186	8051	135	3.4	3.1	drier/enriched
	Core5LI	8163	8086	77	-4.0	-0.8	drier/enriched

	Curtis6VII93	N/A	N/A	N/A	N/A	N/A	N/A
	LagoPuertoArturo	N/A	N/A	N/A	N/A	N/A	N/A
N.W.South-America	LP	N/A	N/A	N/A	N/A	N/A	N/A
N.E.South-America	PAD07	8215	8165	50	-2.7	-2.7	wetter/depleted
	LG11	8442	8242	200	-3.0	-2.9	wetter/depleted
	RN1	N/A	N/A	N/A	N/A	N/A	N/A
	TM6	N/A	N/A	N/A	N/A	N/A	N/A

Appendix A

Table A1. Age model information.

Record ID	Published Age Model Algorithm	Published 14C Cal. Curve	Contains Hiatus?	Contains Reversal?	In SISALv2?	Age Model Chosen
ABC1	MOD-AGE	N/A	N	Y	N	Bacon
ANJB2	StalAge	N/A	Y	Y	Y	SISAL Bacon
BA03	StalAge	N/A	N	N	Y	SISAL Bacon
BTV21a	unknown	N/A	N	N	Y	SISAL Bacon
C7	Bacon	IntCal13	N	N	N/A	Bacon
CM2013	StalAge	N/A	N	N	Y	SISAL copRa
CM2019	StalAge	N/A	N	N	Y	SISAL Bacon
Core17940	CALIB 3.0.3	unknown	N	Y	N/A	Bacon
Core5LI	Bacon	IntCal20	N	Y	N/A	Bacon
CP	StalAge	N/A	N	Y	Y	SISAL Bchron
Curtis6VII93	linear interpolation	unknown	N	N	N/A	Bacon
D4Cheng	unknown	N/A	N	N	Y	Bacon
D4Dykoski	linear interpolation	N/A	N	N	Y	Bacon
EJConroy	CALIB 5.0	unknown	N	N	N/A	Bacon
F14	Bacon	IntCal20	N	Y	N/A	Bacon
FR5	unknown	IntCal09	N	N	Y	SISAL copRa
GB2GC1	Bacon	Marine13	N	N	N/A	Bacon

Record ID	Published Age Model Algorithm	Published 14C Cal. Curve	Contains Hiatus?	Contains Reversal?	In SISALv2?	Age Model Chosen
GURM1	COPRA	N/A	N	N	N	SISAL Bacon
H14	unknown	N/A	N	N	Y	Bacon
H5	unknown	N/A	N	Y	Y	SISAL Bacon
HF01	polynomial fit	N/A	N	N	N	SISAL copRa
JAR7	linear interpolation	N/A	N	N	Y	SISAL Bacon
JPC51	CALIB 6.0	unknown	N	N	N/A	Bacon
KM1	StalAge	N/A	N	N	Y	SISAL Bchron
KMA	StalAge	N/A	N	N	Y	SISAL Bacon
KN51	unknown	N/A	N	Y	Y	SISAL copRa
LagoPuertoArturo	CLAM 2.2	IntCal13	N	N	N/A	Bacon
LBA99	linear interpolation	IntCal04	Y	N	N/A	Bacon
LC1	CALIB	unknown	N	Y	N/A	Bacon
LG11	unknown	N/A	N	N	Y	SISAL Bacon
LH2	linear interpolation	N/A	N	N	Y	SISAL Bacon
LP	CALIB 5.0	unknown	N	N	N/A	Bacon
LR06B32013	linear interpolation	N/A	N	N	Y	SISAL Bchron
LSF19	unknown	N/A	Y	N	N	SISAL Bacon
M981P	CALIB 4.3	unknown	N	N	N/A	Bacon
MAW6	COPRA	N/A	N	Y	Y	SISAL Bchron
MD02_2550	CALIB 5.0	unknown	N	N	N/A	Bacon
NARC	linear interpolation	N/A	N	N	Y	SISAL copRa
NCB	Isoplot 3	N/A	N	N	Y	SISAL Bacon
PAD07	unknown	N/A	N	N	N	Bacon
ParuCo	CALIB 6.0	IntCal09	N	N	N/A	Bacon

Record ID	Published Age Model Algorithm	Published 14C Cal. Curve	Contains Hiatus?	Contains Reversal?	In SISALv2?	Age Model Chosen
PET-PI6	OxCal	IntCal09	N	N	N/A	Bacon
PLJ-JUN15	Bacon	IntCal13	N	N	N/A	Bacon
Q52007	linear interpolation	N/A	N	N	Y	Bacon
Q5Cheng	unknown	N/A	N	N	Y	Bacon
RN1	unknown	N/A	N	N	Y	SISAL Bchron
RN4	unknown	N/A	N	N	Y	SISAL Bchron
SG1	linear interpolation	N/A	N	N	Y	SISAL Bacon
Sha3	COPRA	N/A	N	N	Y	SISAL Bchron
SSC01	StalAge	N/A	N	N	Y	Bacon
Staubwasser63KA	least-squares	IntCal98	N	N	N/A	Bacon
T8	linear interpolation	N/A	N	N	Y	Bacon
TA122	Bacon	N/A	N	N	Y	SISAL copRa
TK07	Bacon	N/A	N	N	N	SISAL Bacon
TK20	Bacon	N/A	N	N	N	SISAL Bacon
TM6	COPRA	N/A	N	N	Y	SISAL Bacon
TOW109B	CALIB 6.0	unknown	N	N	N/A	Bacon
V1	fifth-order polynomial best-fit age model	N/A	N	Y	Y	SISAL Bacon
XBL29	linear interpolation	N/A	N	N	Y	SISAL Bchron
ZLP1	linear interpolation	N/A	N	N	Y	SISAL Bacon

~~Record ID~~	~~Published Age Model Algorithm~~	~~Published 14C Cal. Curve~~	~~Contains Hiatus?~~	~~Contains Reversal?~~	~~In SISALv2?~~	~~Age Model Chosen~~
~~ABC1~~	~~MOD-AGE~~	~~N/A~~	~~N~~	~~Y~~	~~N~~	~~Bacon~~
~~ANJB2~~	~~StalAge~~	~~N/A~~	~~Y~~	~~Y~~	~~Y~~	~~SISAL Bacon~~
~~BA03~~	~~StalAge~~	~~N/A~~	~~N~~	~~N~~	~~Y~~	~~SISAL Bacon~~

Record ID	Published Age Model Algorithm	Published 14C Cal. Curve	Contains Hiatus?	Contains Reversal?	In SISALv2?	Age Model Chosen
BTV21a	unknown	N/A	N	N	Y	SISAL Bacon
C7	Bacon	IntCal13	N	N	N/A	Bacon
CM2013	StalAge	N/A	N	N	Y	SISAL copRa
CM2019	StalAge	N/A	N	N	Y	SISAL Bacon
Core17940	CALIB 3.0.3	unknown	N	Y	N/A	Bacon
Core5LI	Bacon	IntCal20	N	Y	N/A	Bacon
CP	StalAge	N/A	N	Y	Y	SISAL Bchron
Curtis6VII93	linear interpolation	unknown	N	N	N/A	Bacon
D4Cheng	unknown	N/A	N	N	Y	Bacon
D4Dykoski	linear interpolation	N/A	N	N	Y	Bacon
EJConroy	CALIB 5.0	unknown	N	N	N/A	Bacon
F14	Bacon	IntCal20	N	Y	N/A	Bacon
FR5	unknown	IntCal09	N	N	Y	SISAL copRa
GB2GC1	Bacon	Marine13	N	N	N/A	Bacon
GURM1	COPRA	N/A	N	N	N	SISAL Bacon
H14	unknown	N/A	N	N	Y	Bacon
H5	unknown	N/A	N	Y	Y	SISAL Bacon
HF01	polynomial fit	N/A	N	N	N	SISAL copRa
IAR7	linear interpolation	N/A	N	N	Y	SISAL Bacon
IPC51	CALIB 6.0	unknown	N	N	N/A	Bacon
KM1	StalAge	N/A	N	N	Y	SISAL Bchron

Record ID	Published Age Model Algorithm	Published 14C Cal. Curve	Contains Hiatus?	Contains Reversal?	In SISALv2?	Age Model Chosen
KMA	StalAge	N/A	N	N	Y	SISAL Bacon
KN51	unknown	N/A	N	Y	Y	SISAL copRa
LagoPuertoArturo	CLAM 2.2	IntCal13	N	N	N/A	Bacon
LBA99	linear interpolation	IntCal04	Y	N	N/A	Bacon
LC1	CALIB	unknown	N	Y	N/A	Bacon
LG11	unknown	N/A	N	N	Y	SISAL Bacon
LH2	linear interpolation	N/A	N	N	Y	SISAL Bacon
LP	CALIB 5.0	unknown	N	N	N/A	Bacon
LR06B32013	linear interpolation	N/A	N	N	Y	SISAL Bchron
LSF19	unknown	N/A	Y	N	N	SISAL Bacon
M981P	CALIB 4.3	unknown	N	N	N/A	Bacon
MAW6	COPRA	N/A	N	Y	Y	SISAL Bchron
MD02_2550	CALIB 5.0	unknown	N	N	N/A	Bacon
NARC	linear interpolation	N/A	N	N	Y	SISAL copRa
NCB	Isoplot 3	N/A	N	N	Y	SISAL Bacon
PAD07	unknown	N/A	N	N	N	Bacon
ParuCo	CALIB 6.0	IntCal09	N	N	N/A	Bacon
PET-PI6	OxCal	IntCal09	N	N	N/A	Bacon
PLJ-JUN15	Bacon	IntCal13	N	N	N/A	Bacon
Q52007	linear	N/A	N	N	Y	Bacon

Record ID	Published Age Model Algorithm	Published 14C Cal. Curve	Contains Hiatus?	Contains Reversal?	In SISALv2?	Age Model Chosen
	interpolation					
Q5Cheng	unknown	N/A	N	N	Y	Bacon
RN1	unknown	N/A	N	N	Y	SISAL Bchron
RN4	unknown	N/A	N	N	Y	SISAL Bchron
SG1	linear interpolation	N/A	N	N	Y	SISAL Bacon
Sha3	COPRA	N/A	N	N	Y	SISAL Bchron
SSC01	StalAge	N/A	N	N	Y	Bacon
Staubwasser63KA	least-squares	IntCal98	N	N	N/A	Bacon
T8	linear interpolation	N/A	N	N	Y	Bacon
TA122	Bacon	N/A	N	N	Y	SISAL copRa
TK07	Bacon	N/A	N	N	N	SISAL Bacon
TK20	Bacon	N/A	N	N	N	SISAL Bacon
TM6	COPRA	N/A	N	N	Y	SISAL Bacon
TOW109B	CALIB 6.0	unknown	N	N	N/A	Bacon
V1	fifth-order polynomial best-fit age model	N/A	N	Y	Y	SISAL Bacon
XBL29	linear interpolation	N/A	N	N	Y	SISAL Bchron
ZLP1	linear interpolation	N/A	N	N	Y	SISAL Bacon

Appendix B

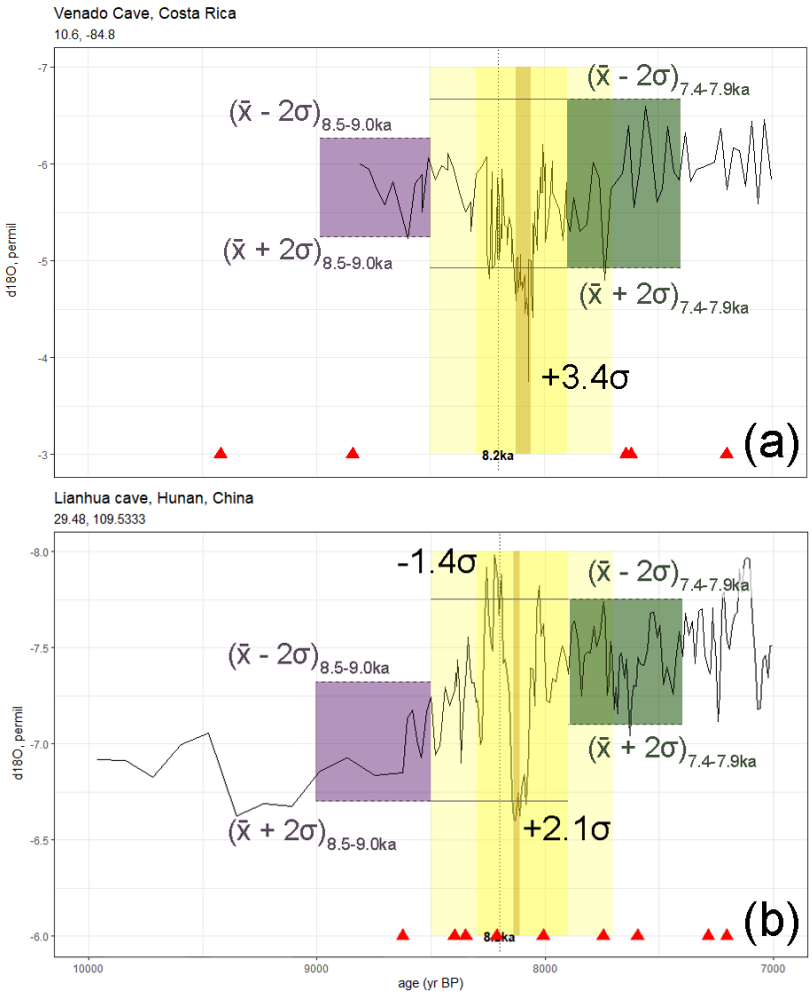

Figure B1. A schematic illustrating the application of our modified Morrill method to (a) the speleothem record of Lachniet et al., 2004 (V1) and (b) the record of Zhang et al., 2013 (LH2). The red triangles indicate the ages of radiometric dates associated with the proxy data. The green and purple shading represents $\bar{x}\pm2\sigma$ in each reference window (7.4 ka-7.9 ka and 8.5 ka-9.0 ka, respectively). The top panel highlights an anomalous isotopic enrichment ("drier"; brown) event which is composed of three separate "events" (separated by < 20 years). As per the event detection methods, these events have been consolidated into a single 8.2 ka Event (8.058 ka-8.124 ka) with the event magnitude given by the maximum absolute z-score over this period (+3.4σ). The bottom panel shows multiple events of opposing signs within the detection window: an anomalous isotopic depletion (-1.4σ, 8.208 ka-8.221 ka) and an anomalous enrichment (+2.1σ, 8.129 ka-8.138 ka; brown). As per the event detection methods, the event with the larger absolute z-score is taken to represent the 8.2 ka Event.

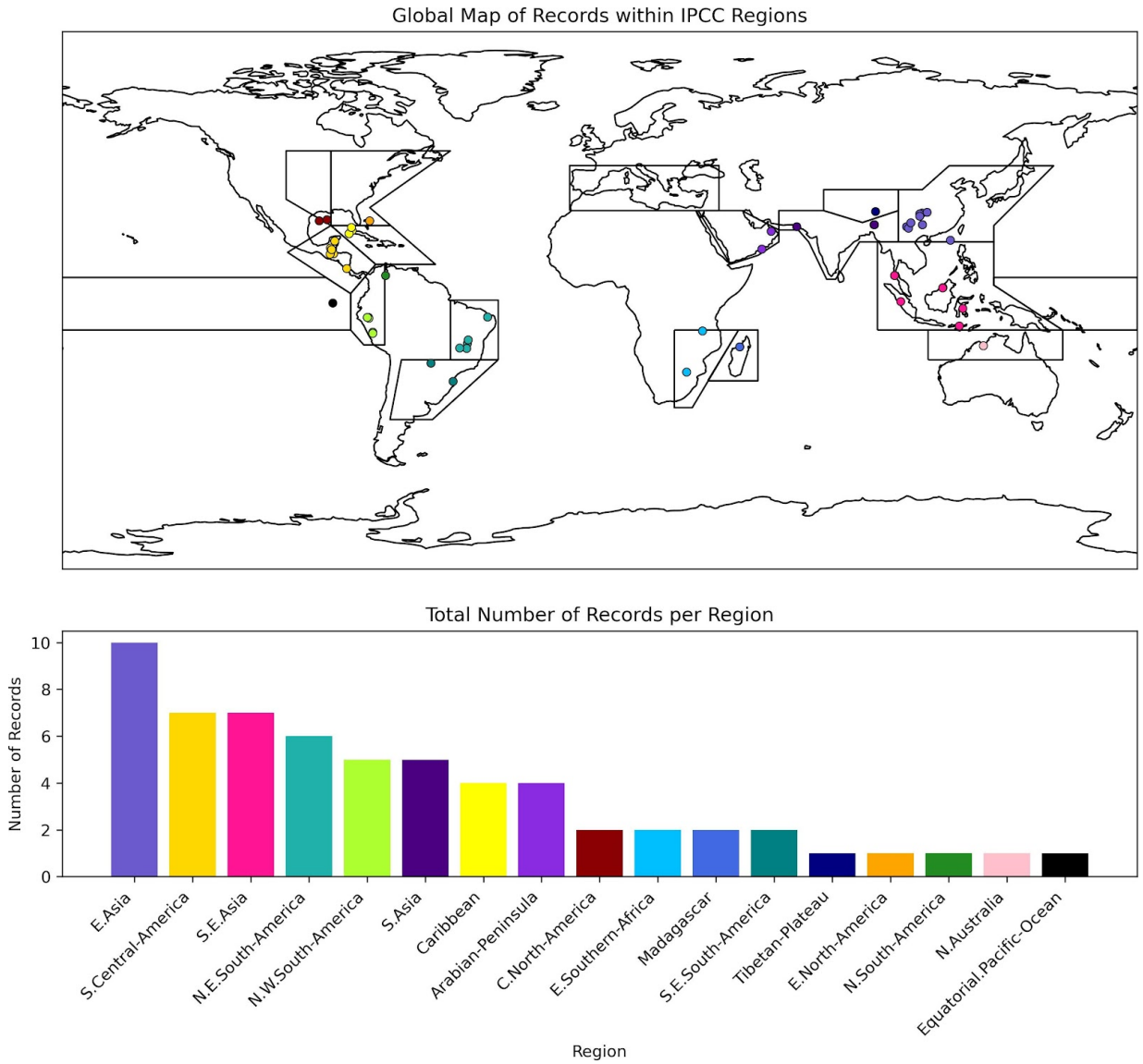

Figure B2. Locations of proxy records within climate reference regions defined in Iturbide et al. (2020).

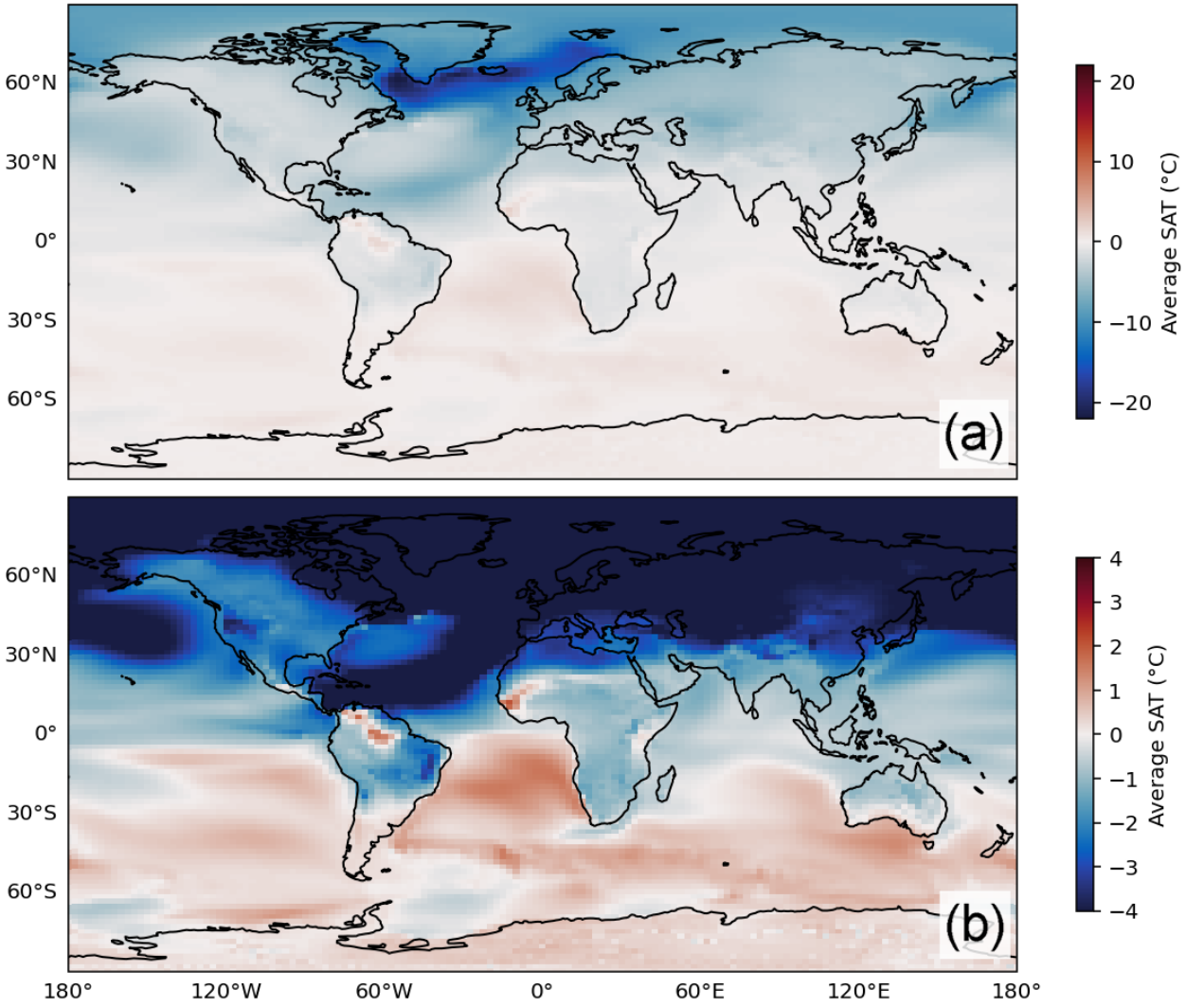

Figure B3. The difference in surface air temperatures between the last 50 years of the "hose" and "ctrl" simulations. Blue shaded areas represent anomalously cold regions, while anomalously warm regions are shaded in red on a global (a) and (b) tropical level.

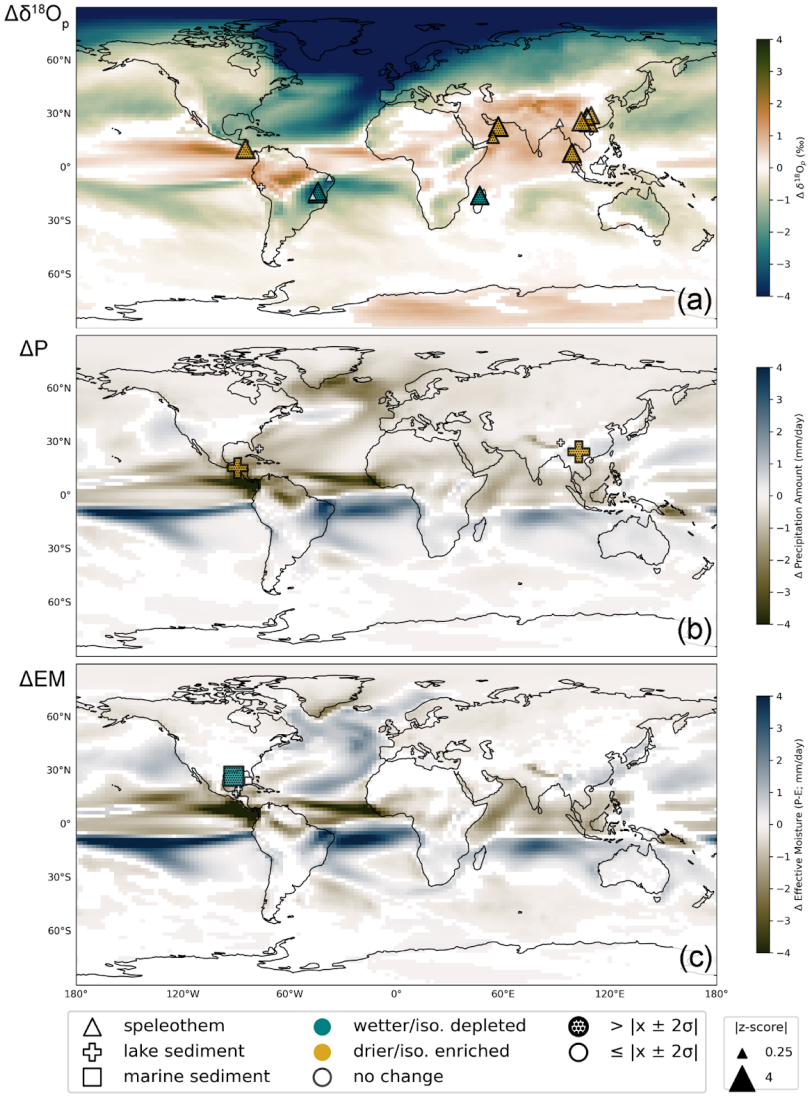

Figure B4. Summary of the 8.2 ka events detected using our modified Morril et al. (2013) method for the paleoclimate records showing agreement with actR (Fig. 4) in the direction of change. Blue symbols represent wetter (and/or isotopically depleted) conditions while brown symbols represent drier (and/or isotopically enriched) conditions relative to each record's mean climatology over the 7.4 ka-7.9 ka and 8.5 ka-9.0 ka windows described in the text. For records in which no event was detected, symbols are shown in white. The archive type is indicated by the symbol shape, and the symbol size is scaled by 250ln(1+|z-score|). The proxy symbols are overlaid on a contour map of the simulated anomalous (a) amount-weighted $\delta^{18}O_p$, (b) precipitation amount, and (c) effective moisture (P-E), calculated from the difference between the last 50 years of the iCESM "hose" and "ctrl" experiments, where only anomalies that exceed the 95% confidence level ($p < 0.05$) are shown.

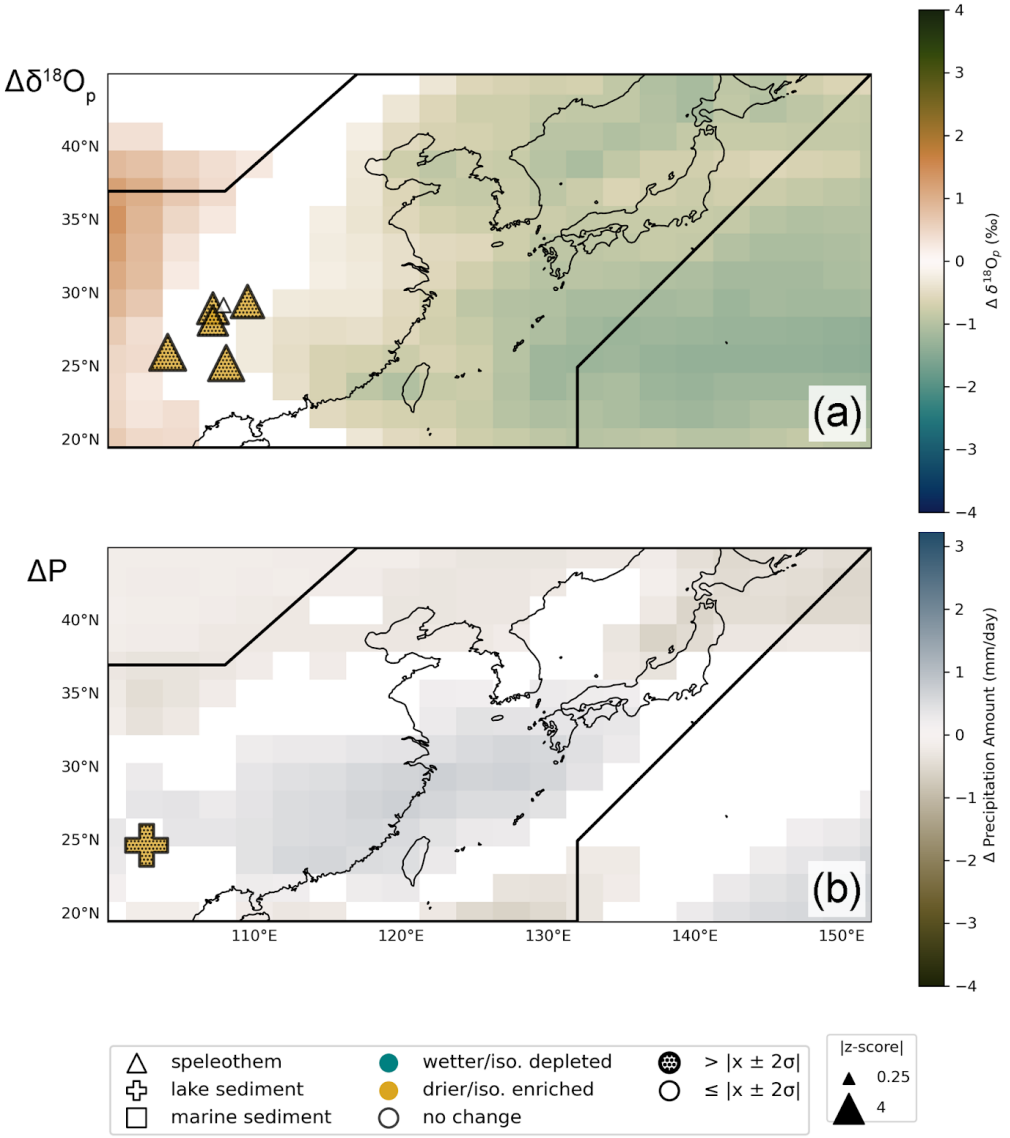

Figure B5. Data-model comparison of IPCC region 35: East Asia (box). Model shading represents (a) the amount-weighted $\delta^{18}O_p$ anomaly, and (b) the precipitation amount anomaly between the last 50 years of the "hose" and "ctrl" simulations that exceed the 95% confidence level ($p < 0.05$). Symbols represent paleoclimate proxy archives within the region corresponding to each respective climate variable, where the brown shaded triangles indicate speleothem records with recorded dry hydroclimate/enriched isotopic anomalies during the 8.2 ka Event and grey symbols indicate records with no hydroclimate anomalies ("no change") relative to each record's mean climatology over the 7.4 ka-7.9 ka and 8.5 ka-9.0 ka windows used in our modified Morrill et al. (2013) method. For symbols showing an anomaly associated with the 8.2 ka Event, size is scaled by 400ln(1+|z-score|) relative to each record's mean and standard deviation.

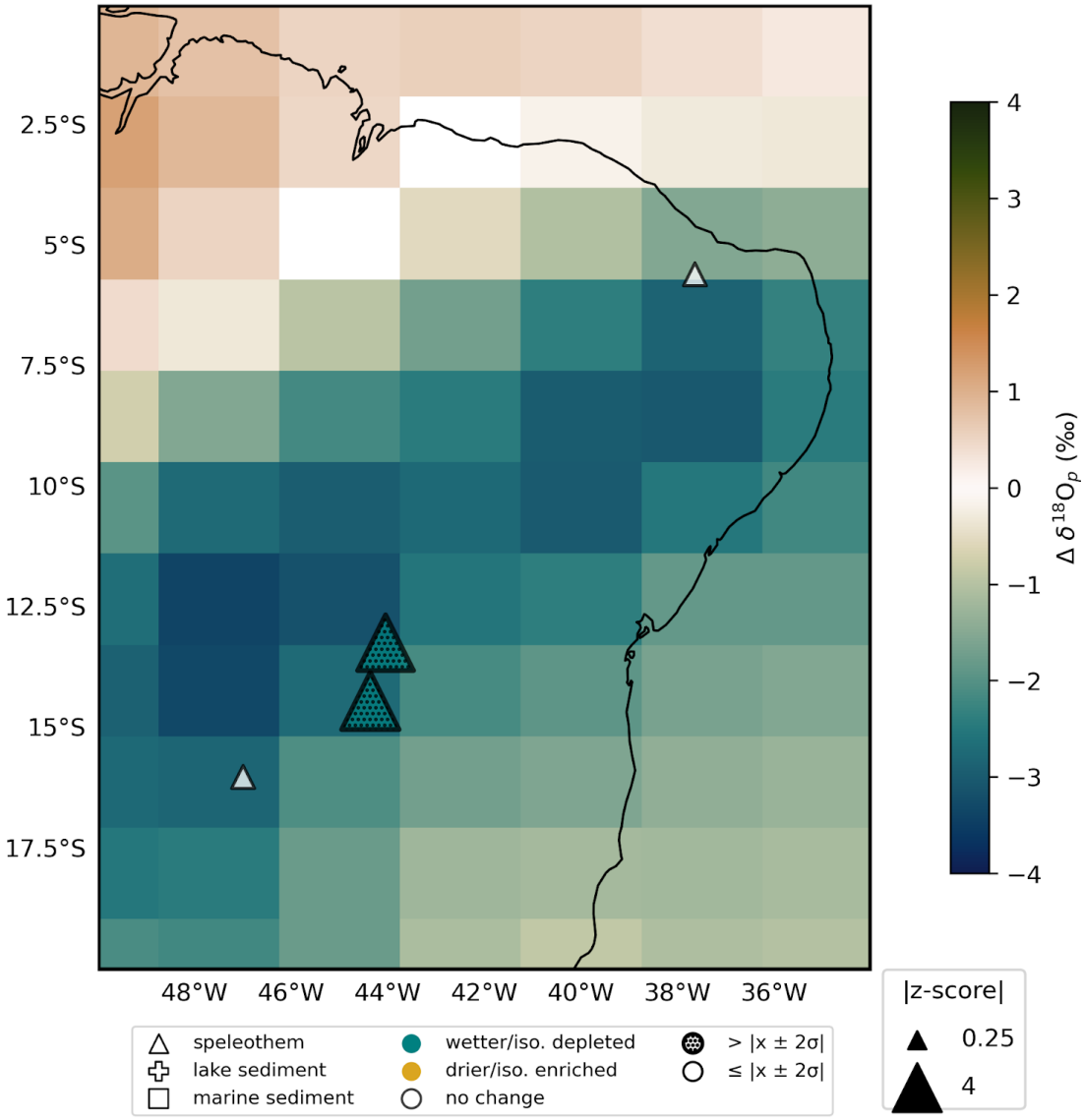

Figure B6. As in Fig. B5, but for IPCC region 11: northeastern South America (box).

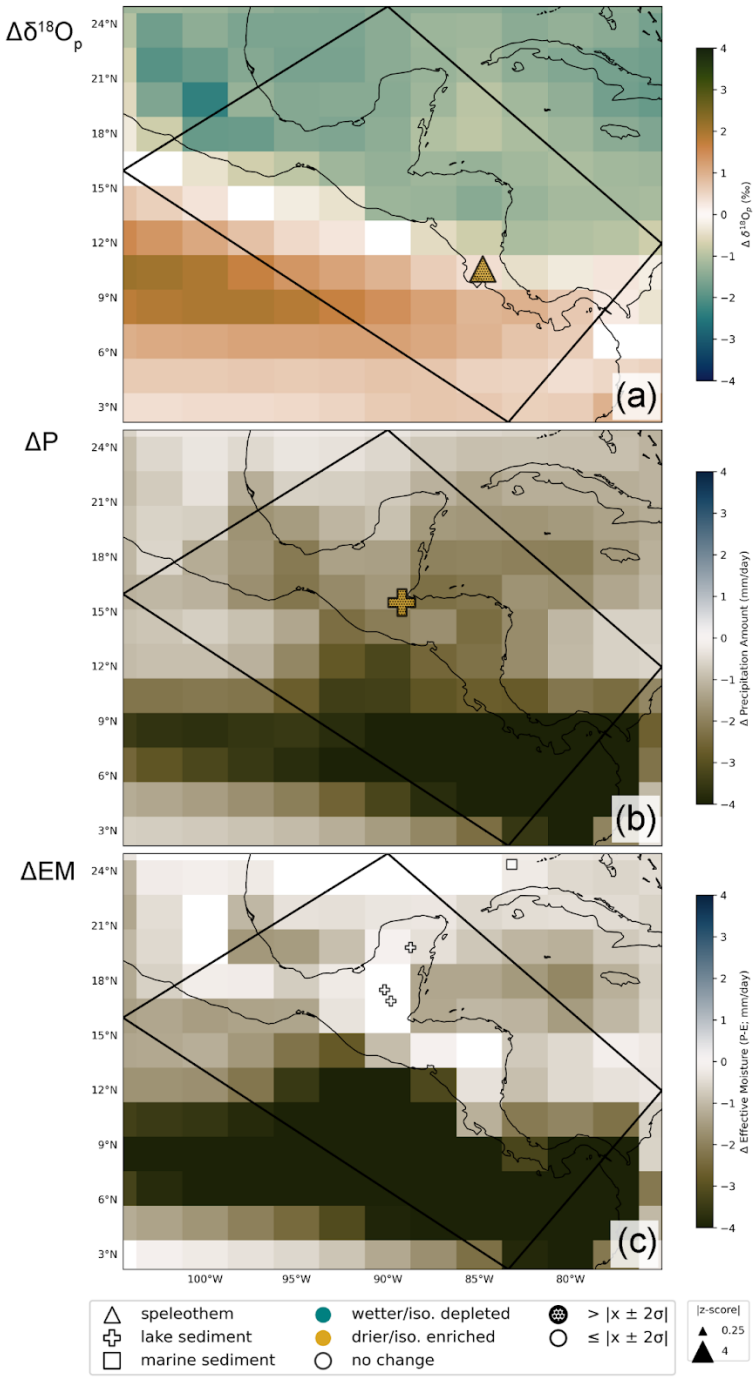

Figure B7. As in Fig. B5, but for IPCC region 7: southern Central America (box), with the addition of (c) the effective moisture (precipitation minus evaporation) anomaly between the last 50 years of the "hose" and "ctrl" simulations.

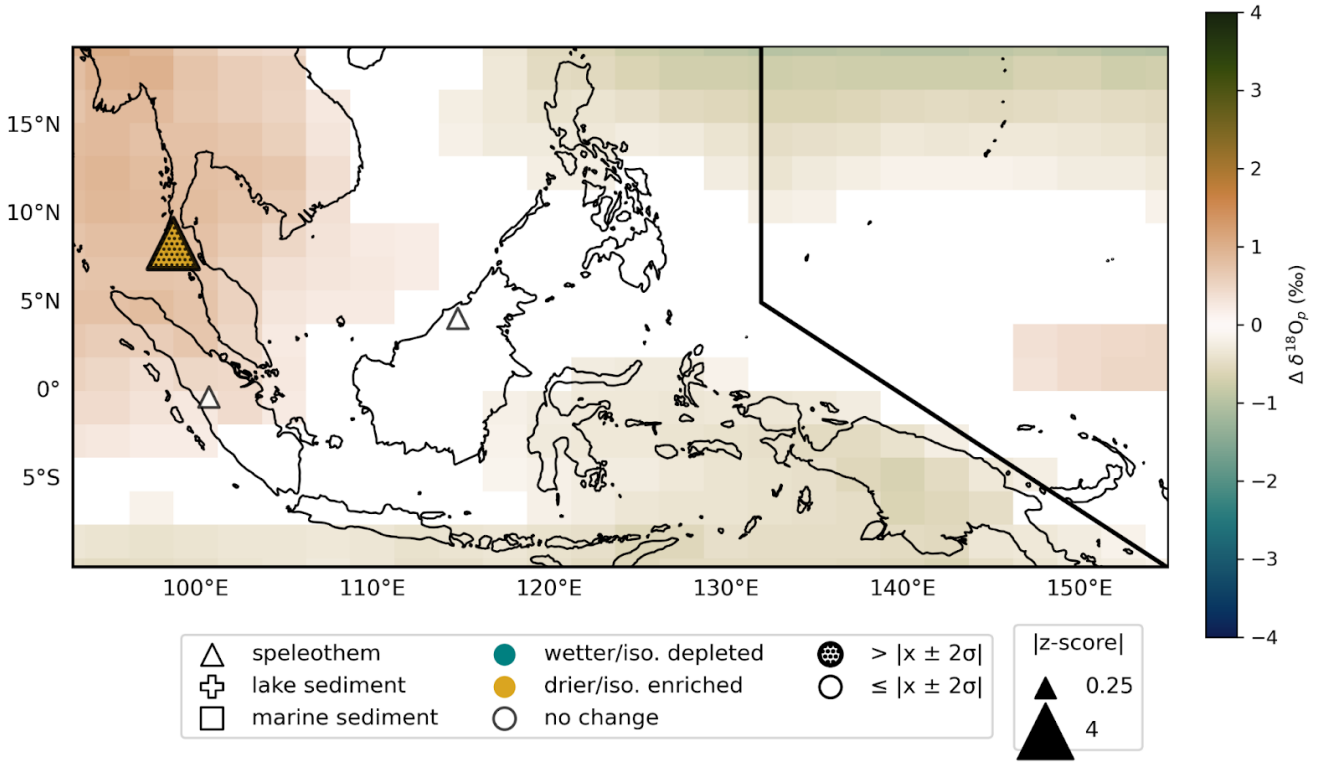

Figure B8. As in Fig. B5, but for IPCC region 38: Southeast Asia.

Appendix C: actR-MM stackplots

C1 Records with wet/depletion events in both actR and MM

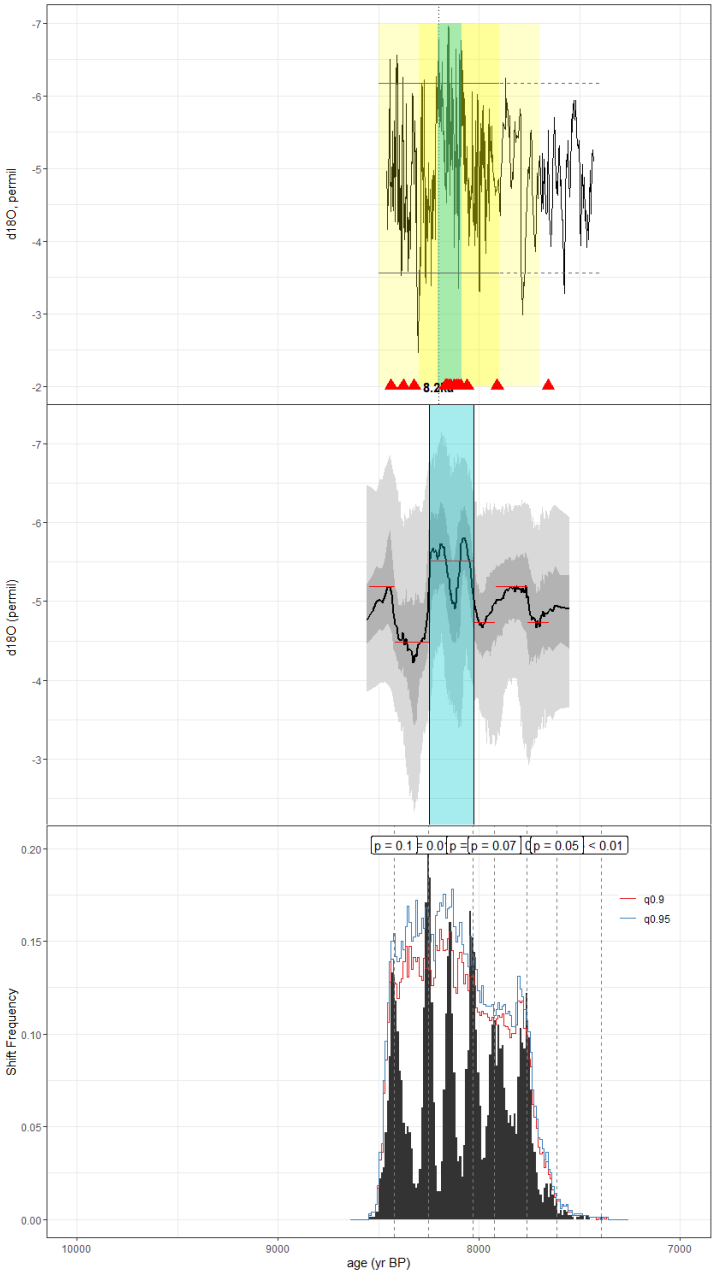

Figure C1. A stackplot from the speleothem record of Duan et al., 2021 (ABC1). The top panel shows the raw oxygen isotope time series with 7.9 ka-8.3 ka highlighted in darker yellow and 7.7 ka-8.5 ka highlighted in lighter yellow, with the ages of radiometric dates represented by red triangles (see schematic in Fig. B1 for more information). The middle panel shows the same time series with age and

paleodata ensemble uncertainty quantile ribbons, where the outermost (lighter) bands represent extreme values and the innermost (darker) bands central values. The horizontal red lines represent mean values assigned to the data by actR, with discontinuities indicating significant changepoints. Vertical blue highlights in the top and middle panels indicate "wet" events derived using the MM and actR methods, respectively, with the width of the highlighted area reflecting the duration of the events as calculated from each method. A bold black outline around the highlighted section indicates a "significant" change, while the lack of an outline reflects "tentative" change. For records reflecting "dry" events (as in Fig. B1), these areas are highlighted in brown instead of blue. The lower panel depicts the frequency of shifts detected in the ensemble dataset (black histogram) relative to 100 null hypothesis surrogate datasets. Red and blue histogram lines represent confidence levels at 90% and 95%, respectively. Dashed vertical lines give the p-values of detected shifts in mean at the alpha = 0.10 level. The age model in the original publication was based on the MOD-AGE algorithm, while the age model used in this synthesis was constructed using the geoChronR package and BACON algorithm.

~~**Figure C1.** A stackplot from the speleothem record of Duan et al., 2021 (ABC1). The top panel shows the raw oxygen isotope time series with 7.9 ka-8.3 ka highlighted in darker yellow and 7.7 ka-8.5 ka highlighted in lighter yellow (see schematic in Fig. B1 for more information). The middle panel shows the same time series with age and paleodata ensemble uncertainty quantile ribbons, where the outermost (lighter) bands represent extreme values and the innermost (darker) bands central values. The horizontal red lines represent mean values assigned to the data by actR, with discontinuities indicating significant changepoints. The lower panel depicts the frequency of shifts detected in the ensemble dataset (black) relative to 100 null hypothesis surrogate datasets (orange). Light and dark orange histogram lines represent confidence levels at 90% and 95%, respectively. Dashed vertical lines give the p-values of detected shifts in mean at the alpha = 0.10 level. The age model in the original publication was based on the MOD-AGE algorithm, while the age model used in this synthesis was constructed using the geoChronR package and BACON algorithm.~~

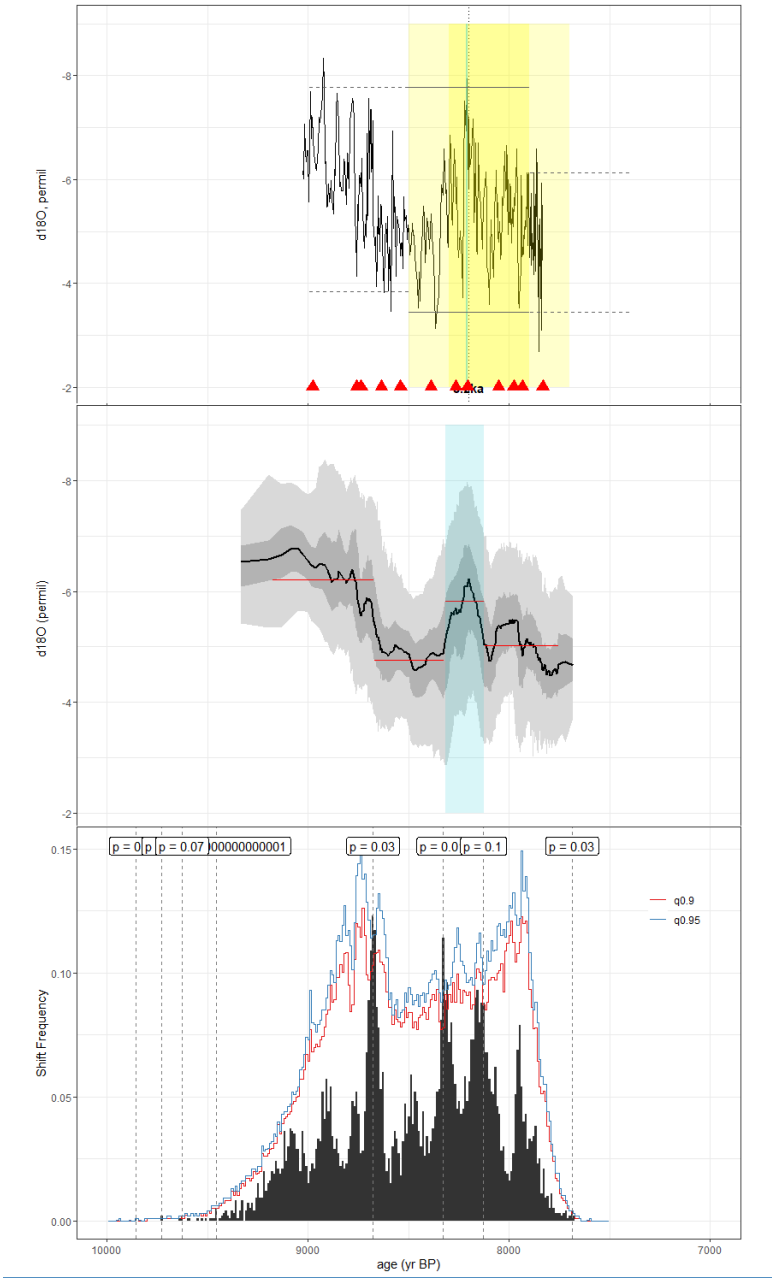

Figure C2. As in Fig. C1, but for the speleothem record of Voarintsoa et al., 2017 (ANJB2). The age model of the original publication was constructed using StalAge. Here, we used the BACON age ensemble from SISALv2.

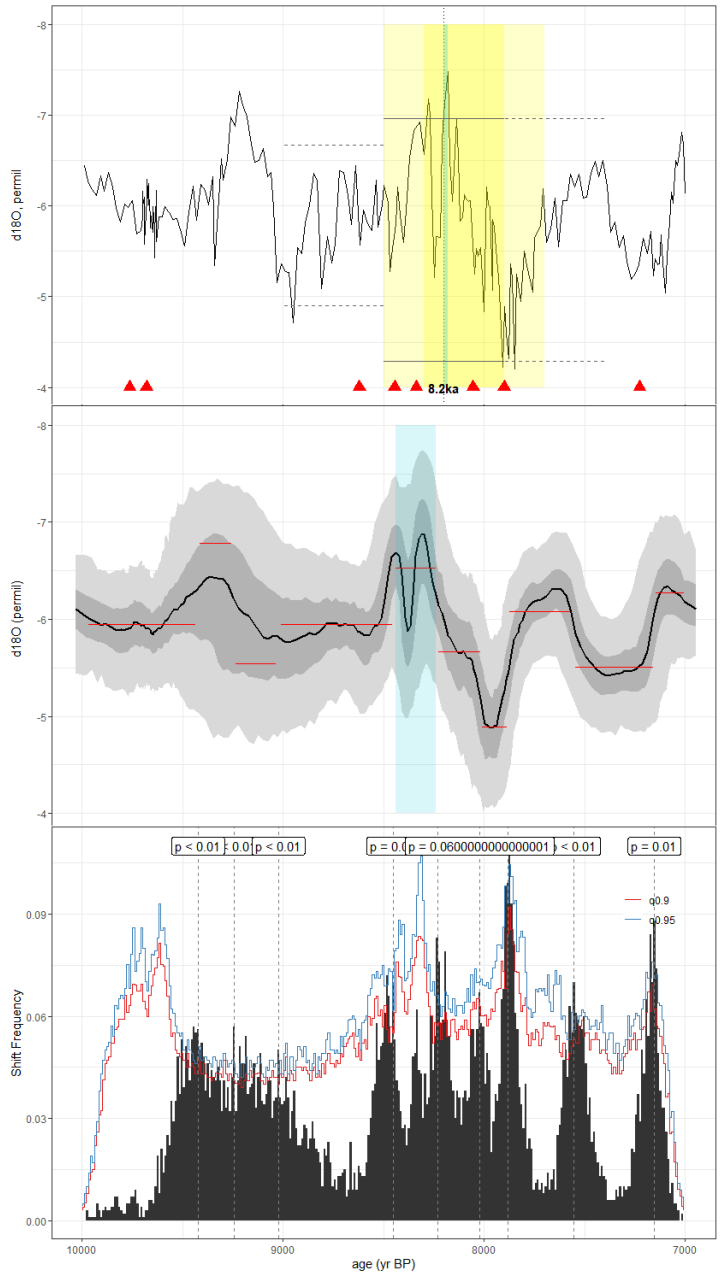

Figure C3. As in Fig. C1, but for the speleothem record of Strikis et al., 2011 (LG11). The original method used in construction of the published age model was unreported, but we leverage the BACON age ensemble published in SISALv2 for our analyses.

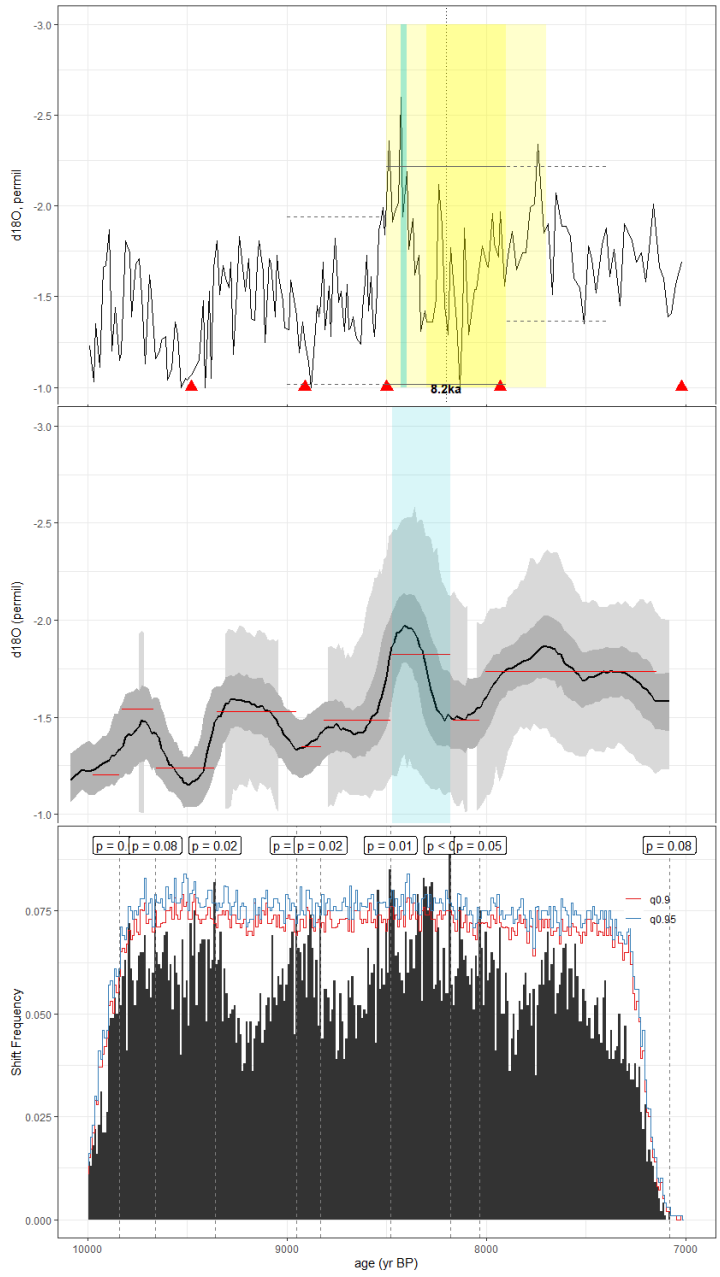

Figure C4. As in Fig. C1, but for the foraminifera record of LoDico et al., 2006 (MD022550). The published age model was constructed using CALIB 5.0, with a 400-year reservoir age correction applied. Here, we used the BACON algorithm included in geoChronR to create the age ensemble.

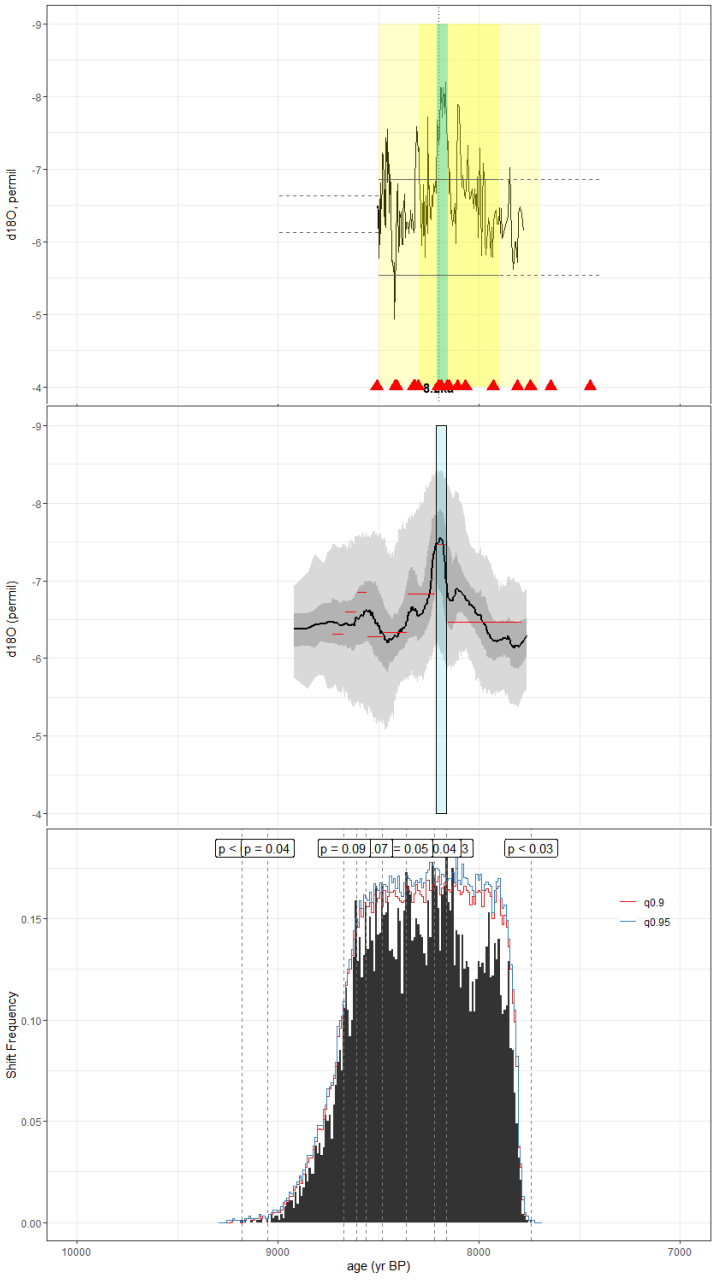

Figure C5. As in Fig. C1, but for the speleothem record of Cheng et al., 2009 (PAD07). The original age modeling method used in the construction of the published time series is unknown. Here, we present an age ensemble using the BACON algorithm provided by geoChronR.

C2 Records with dry/enrichment events in both actR and MM

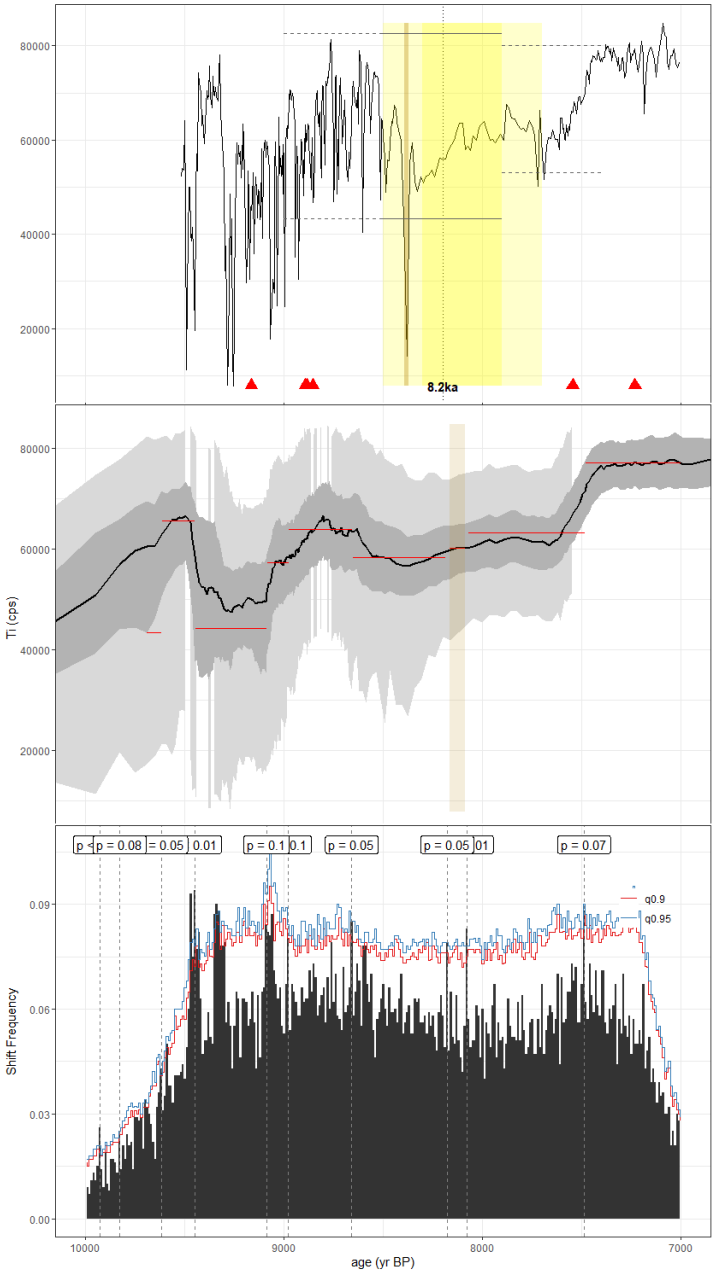

Figure C6. As in Fig. C1, but for the lacustrine titanium content record of Duarte et al., 2021 (Core5LI). The published age model was constructed using BACON using the IntCal20 calibration curve, and here, we construct our age ensemble using the BACON algorithm included with geoChronR.

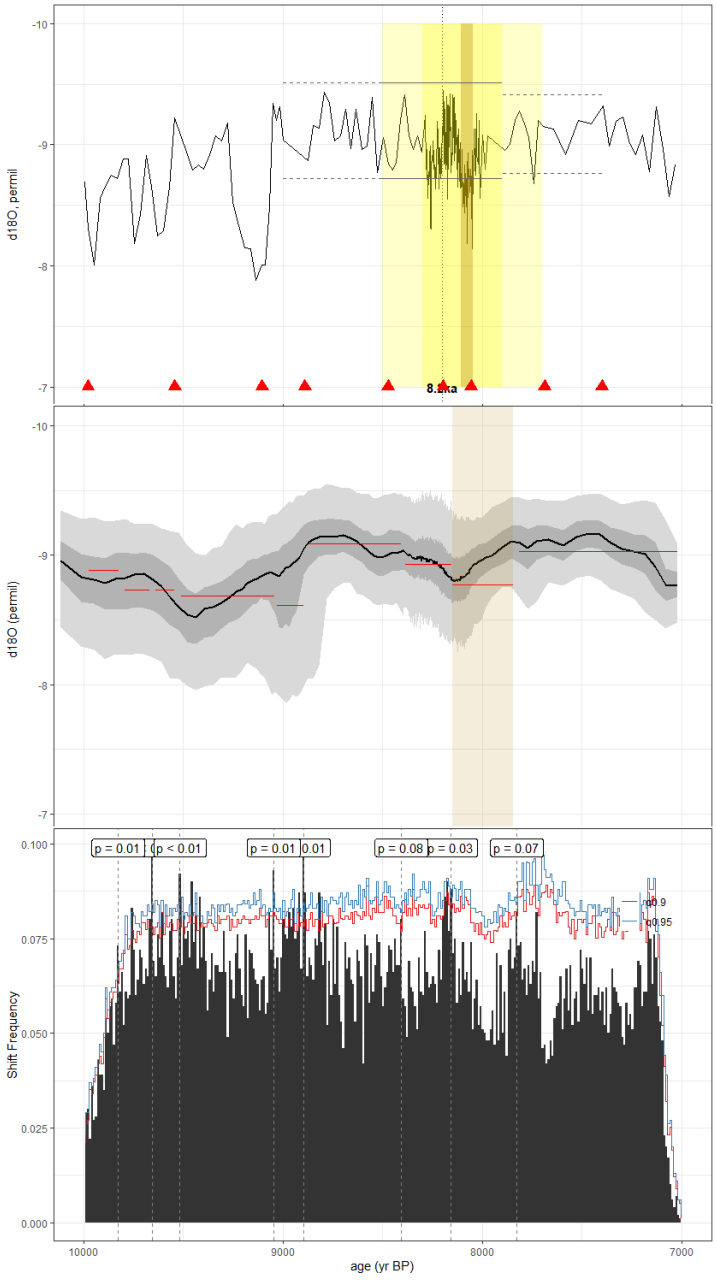

Figure C7. As in Fig. C1, but for the speleothem record of Dykoski et al., 2005 (D4Dykoski). The published age model was constructed by linearly interpolating between U/Th dates. Here, we reconstruct the age model using the BACON algorithm in geoChronR.

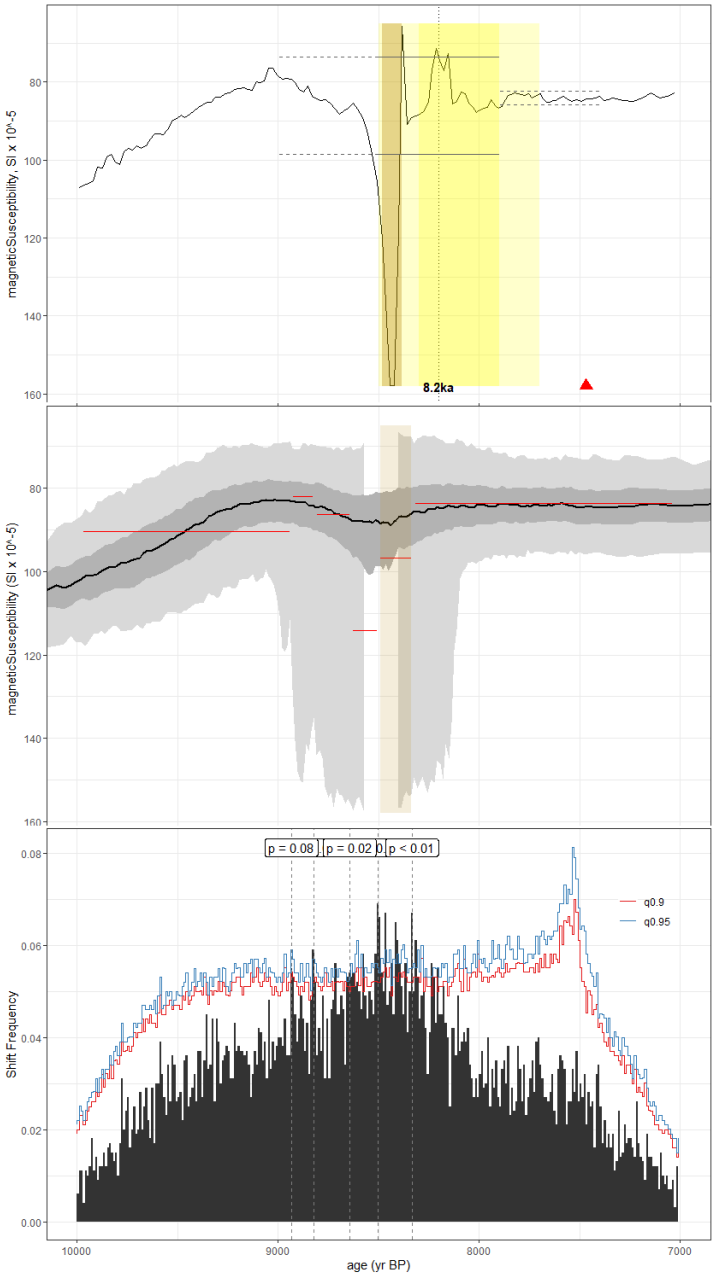

Figure C8. As in Fig. C1, but for the lake sediment magnetic susceptibility record of Hillman et al., 2021 (F14). The original age model was constructed using BACON with the IntCal20 calibration curve. Here, we have reconstructed it using the BACON algorithm in geoChronR.

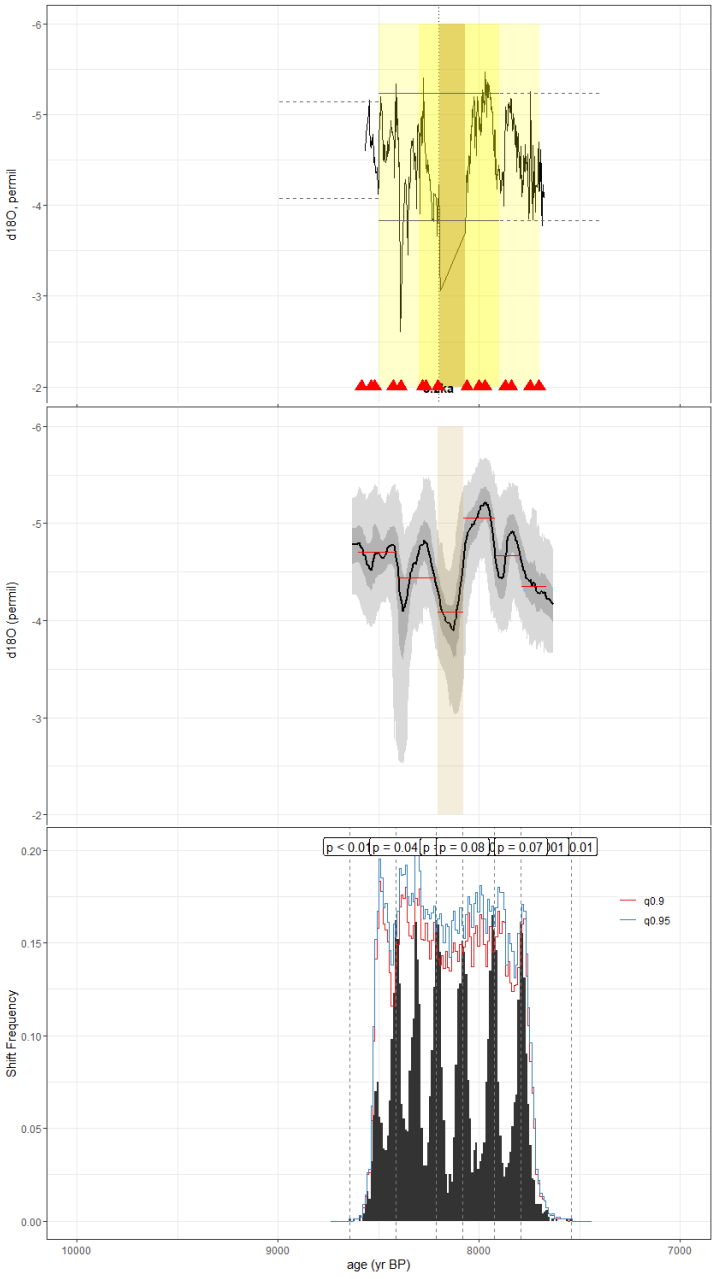

Figure C9. As in Fig. C1, but for the speleothem record of Cheng et al., 2009 (H14). The age modeling algorithm used to construct the original age model was unreported. Here, we constructed our age ensemble using BACON in geoChronR.

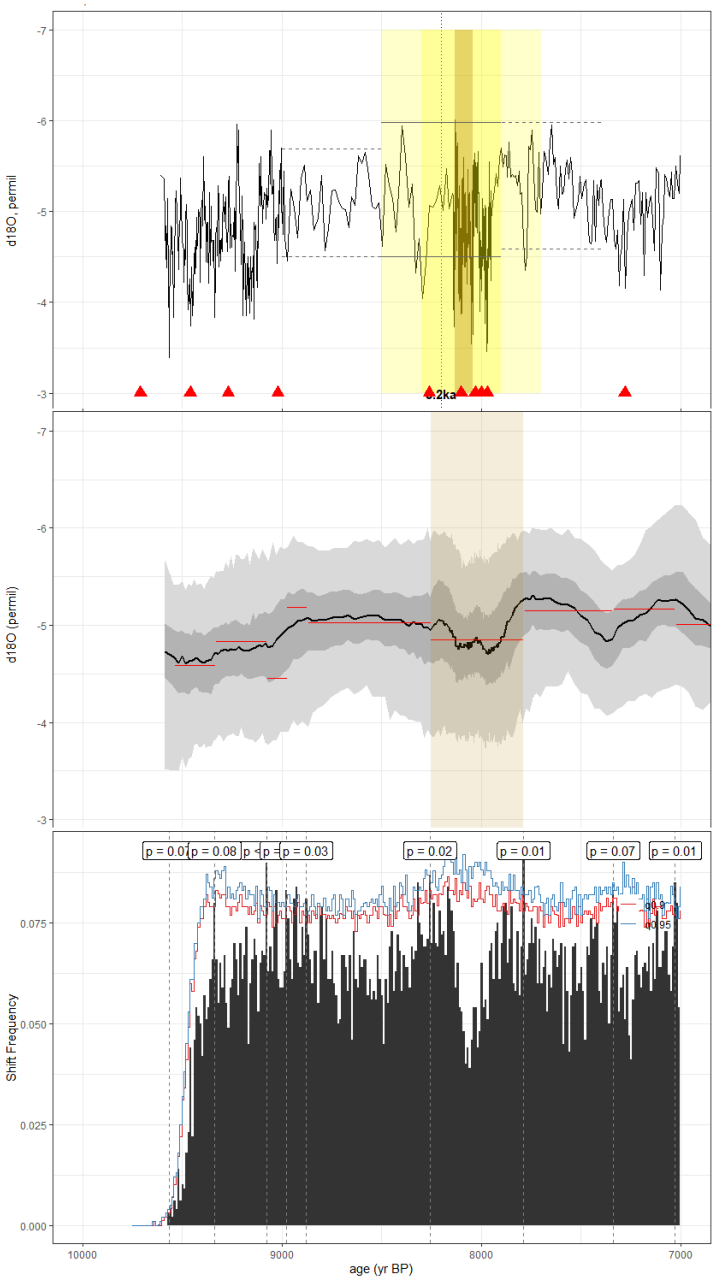

Figure C10. As in Fig. C1, but for the speleothem record of Neff et al., 2001 (H5). While the method used in the construction of the published time series was unreported, we leveraged the SISALv2 BACON ensemble for our analyses.

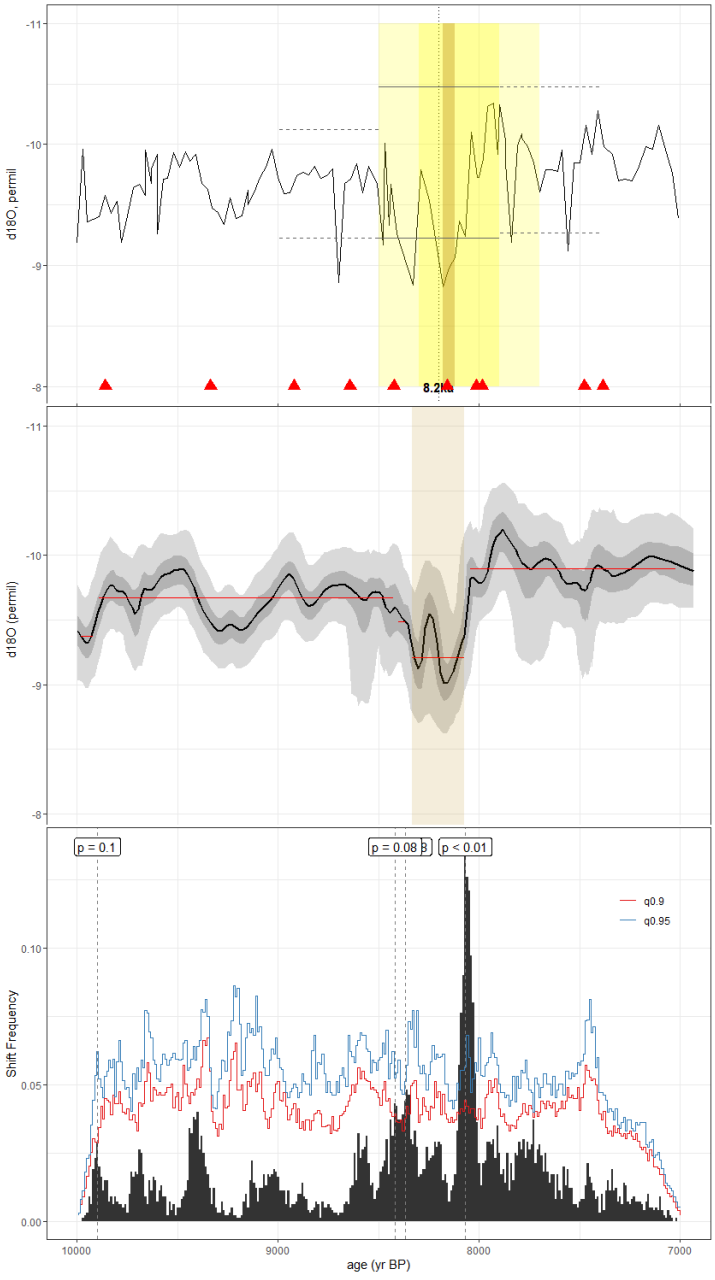

Figure C11. As in Fig. C1, but for the speleothem record of Yang et al., 2019 (HF01). The published age model was constructed via polynomial regression between radiometric dates. For our analyses, we leveraged the copRa age ensemble included in version 2 of the SISAL database.

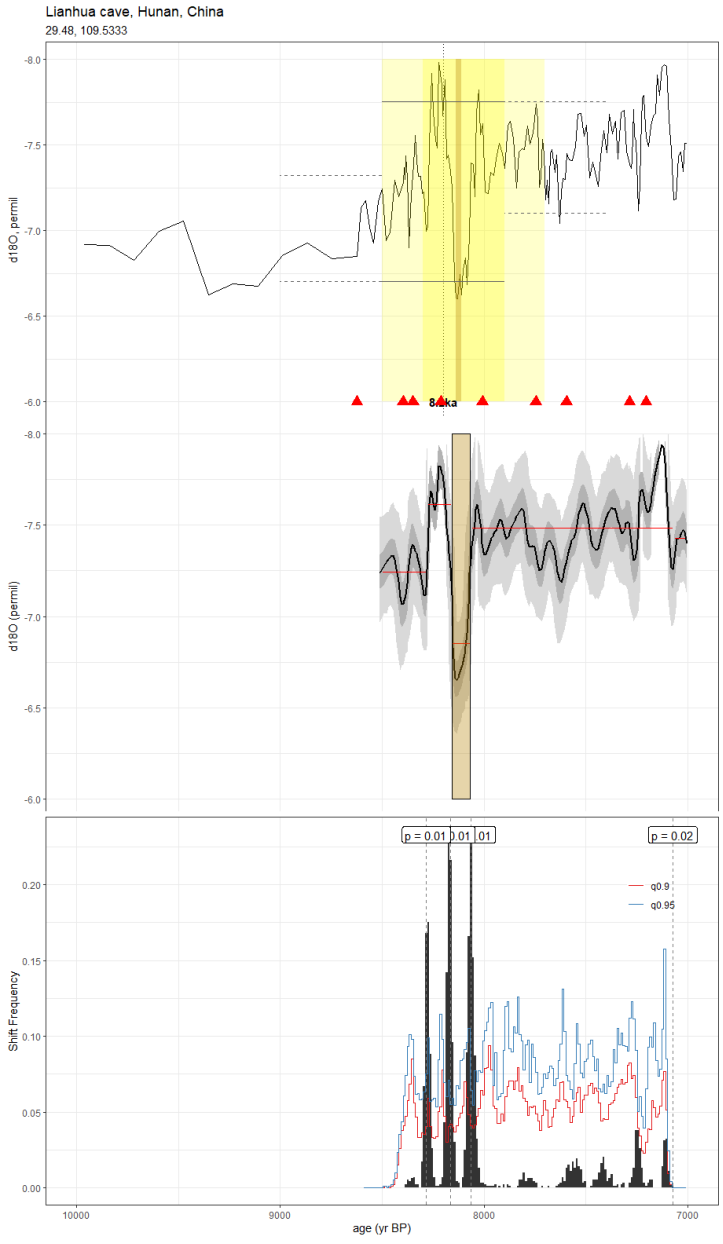

Figure C12. As in Fig. C1, but for the speleothem record of Zhang et al., 2013 (LH2). The published age model was generated by linearly interpolating between radiometric dates. Here, we employ the BACON age ensemble included in version 2 of the SISAL database.

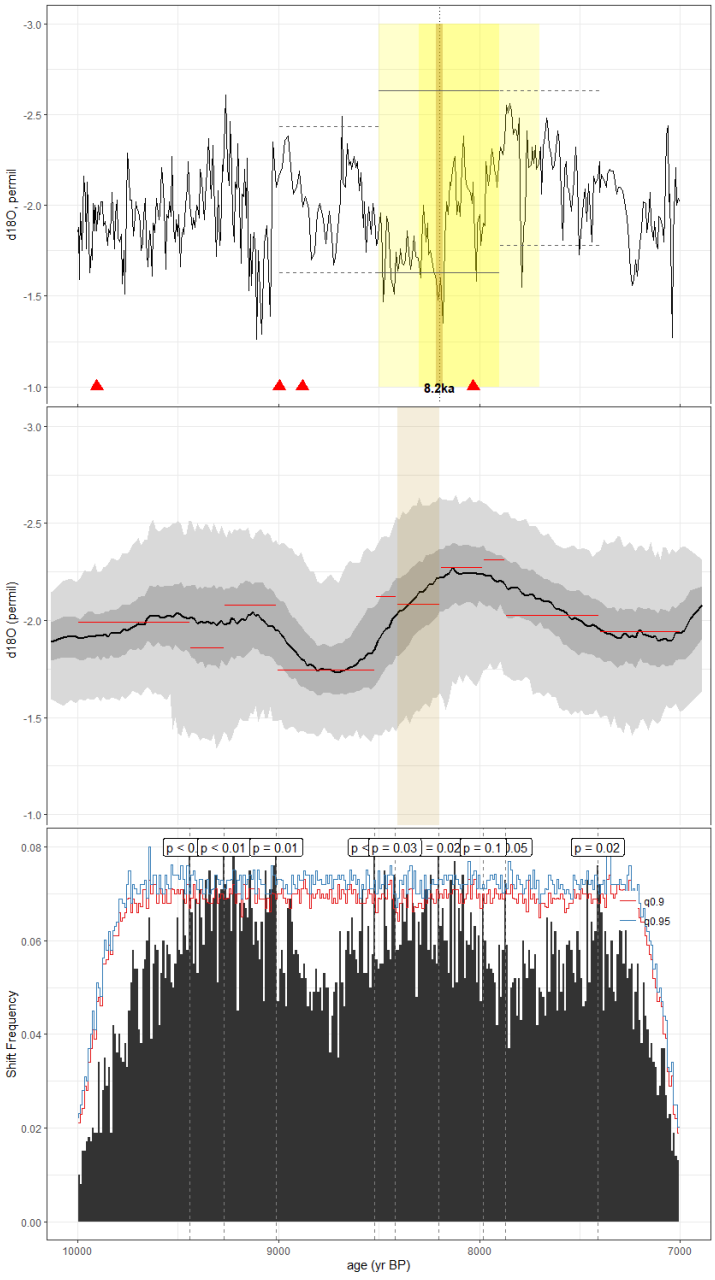

Figure C13. As in Fig. C1, but for the speleothem record of Fleitmann et al., 2007 (Q52007). The published age model was created via a polynomial fit to the age-depth curve of the Th–U data. Our age ensemble leverages the BACON algorithm included in geoChronR.

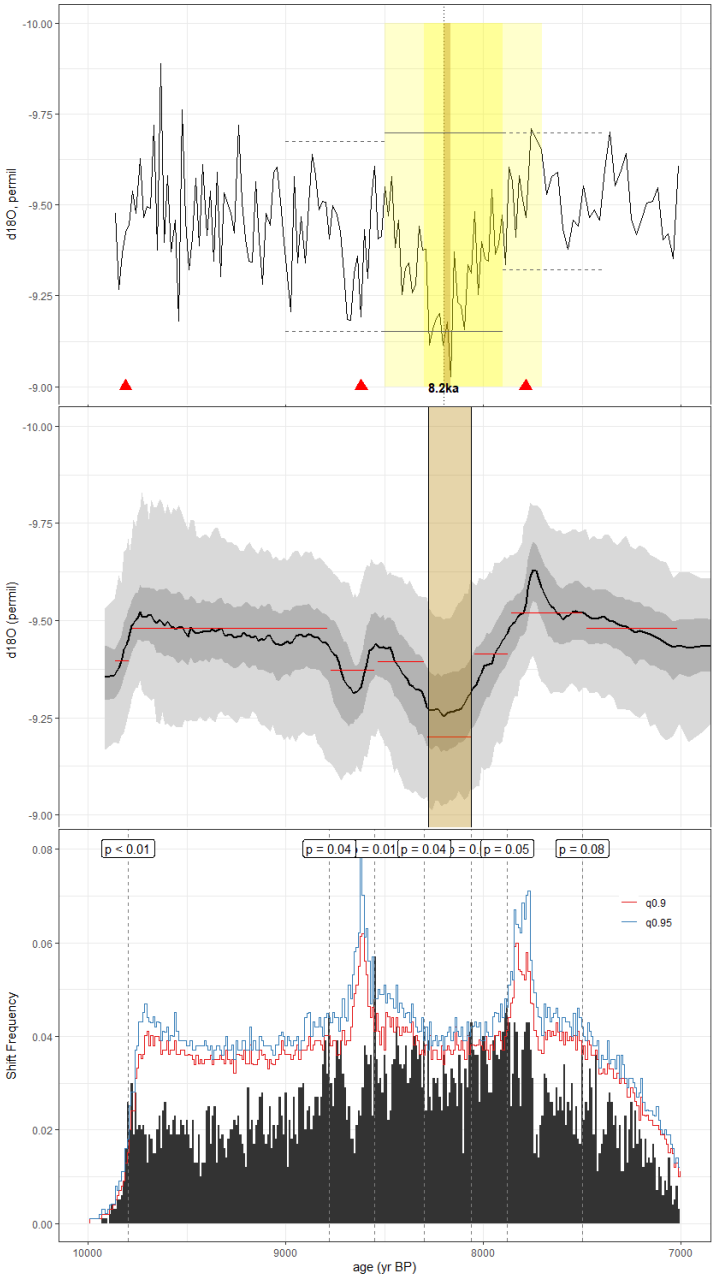

Figure C14. As in Fig. C1, but for the speleothem record of Jiang et al., 2012 (SG1). The published age model was constructed by linear interpolation between U/Th dates. Here, we leverage the BACON ensemble from SISALv2 for our analyses.

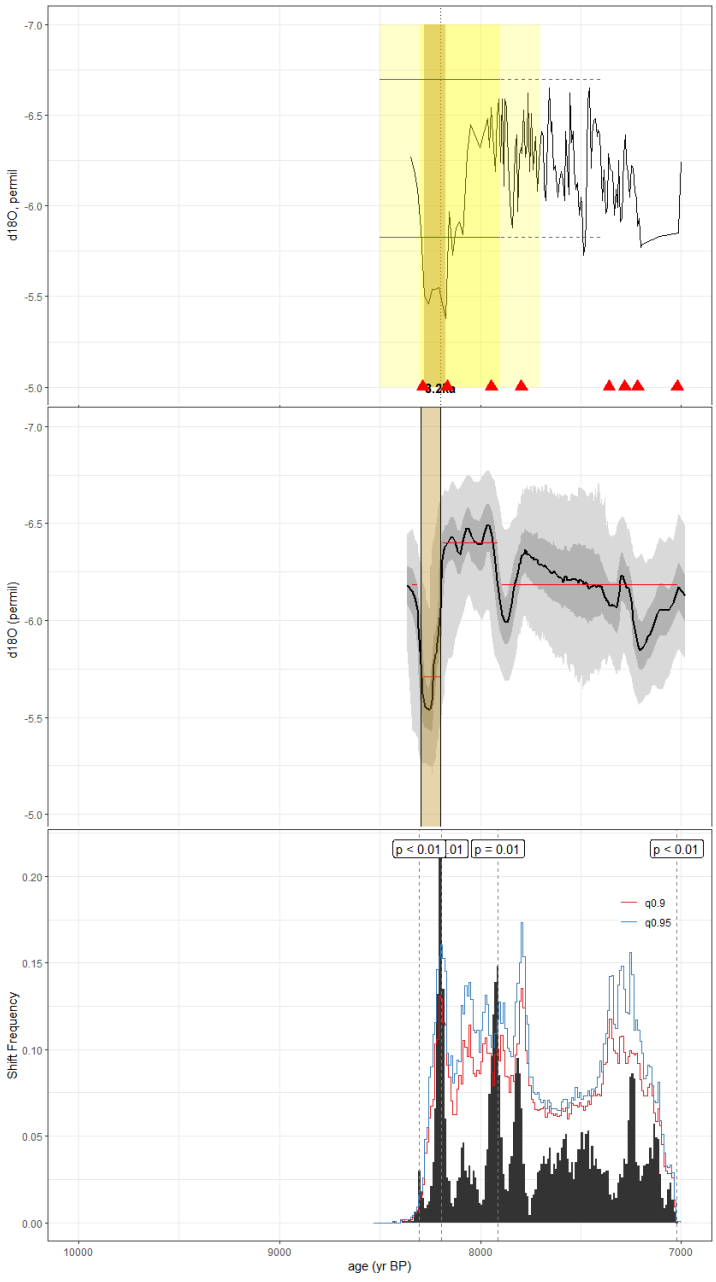

Figure C15. As in Fig. C1, but for the speleothem record of Chawchai et al., 2021 (TK07). The published age model was constructed using the BACON algorithm. Here, we used the BACON age ensemble supplied in the SISALv2 database.

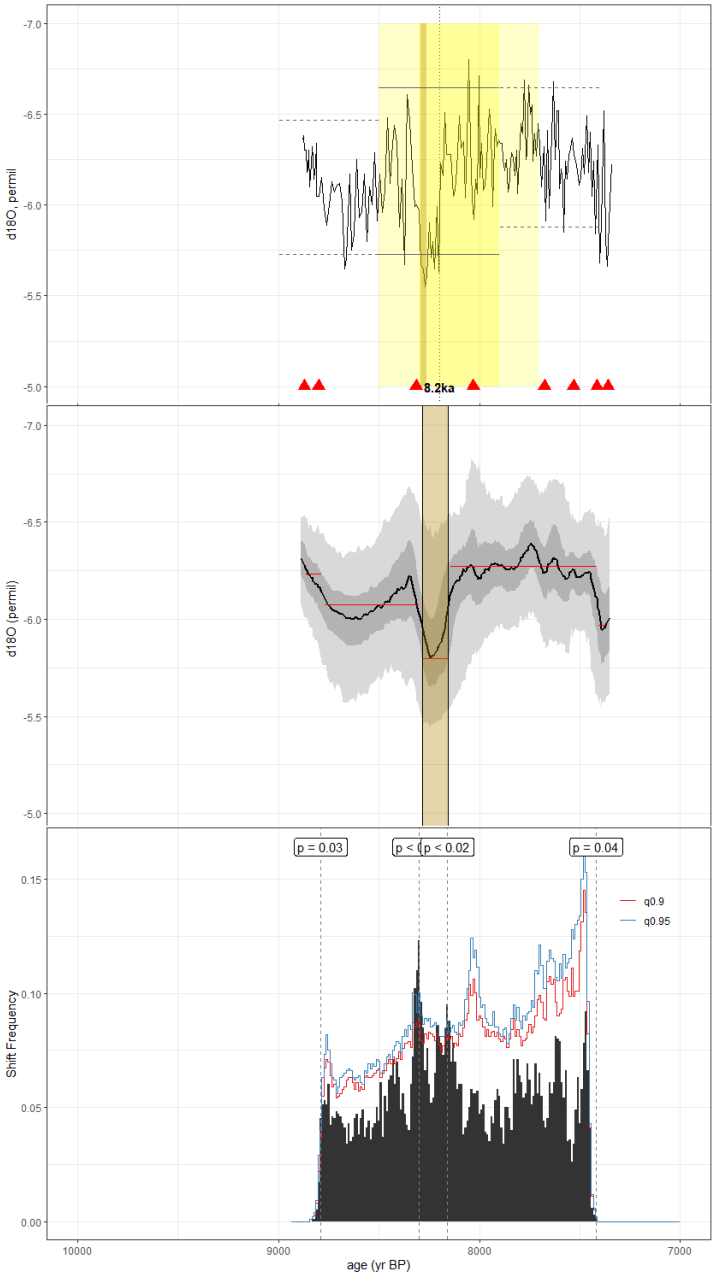

Figure C16. As in Fig. C1, but for the speleothem record of Chawchai et al., 2021 (TK20). The published age model was constructed using the BACON algorithm. Here, we used the BACON age ensemble supplied in the SISALv2 database.

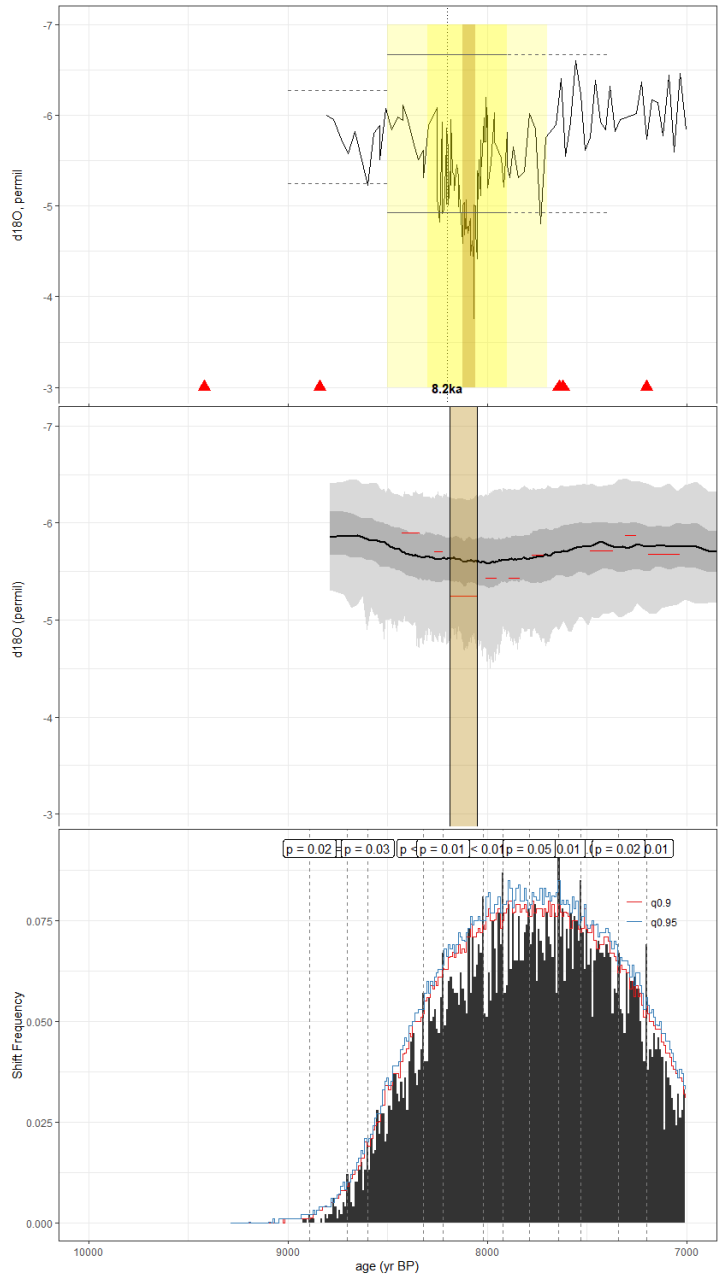

Figure C17. As in Fig. C1, but for the speleothem record of Lachniet et al., 2004 (V1). The published time series was aligned to a fifth-order polynomial best-fit age model between isochron dates. We employ the BACON ensemble provided by SISALv2 for our analyses.

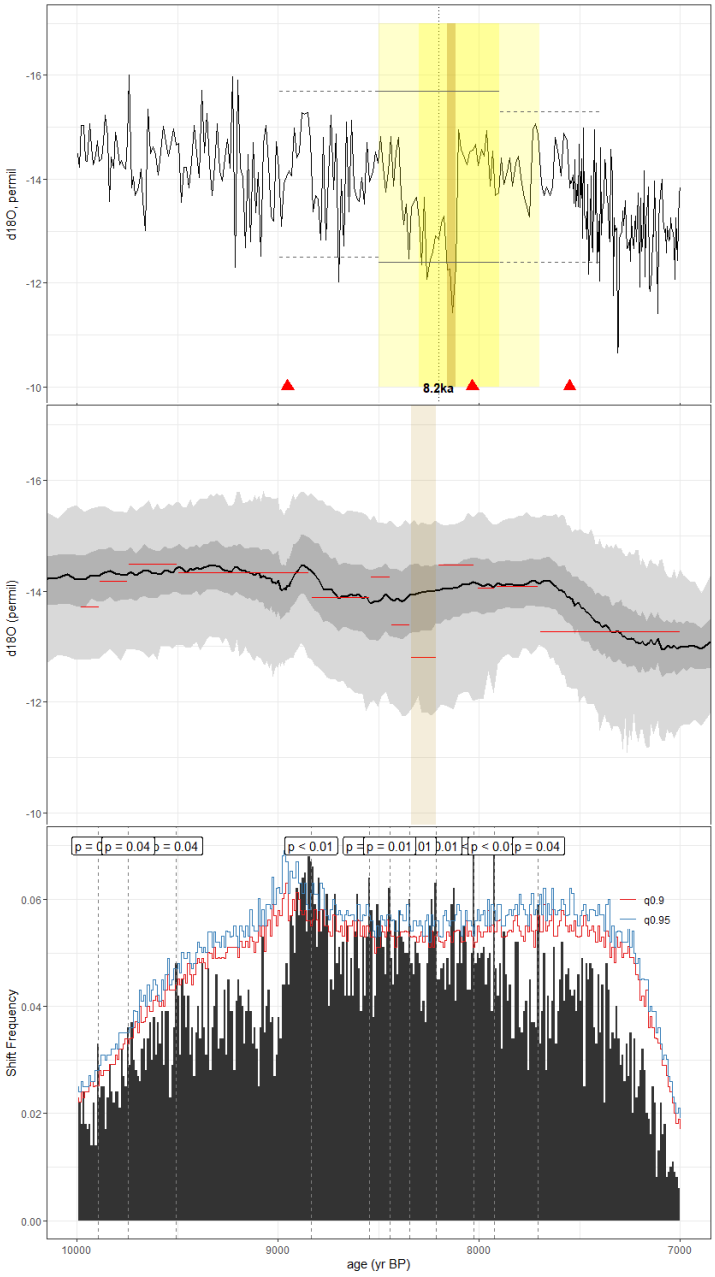

Figure C18. As in Fig. C1, but for the speleothem record of Huang et al., 2016 (ZLP1). The published age model was derived from linear interpolation between radiometric dates. For our analyses, we leveraged the SISALv2 BACON age ensemble.

C3 Records with no event in both actR and MM

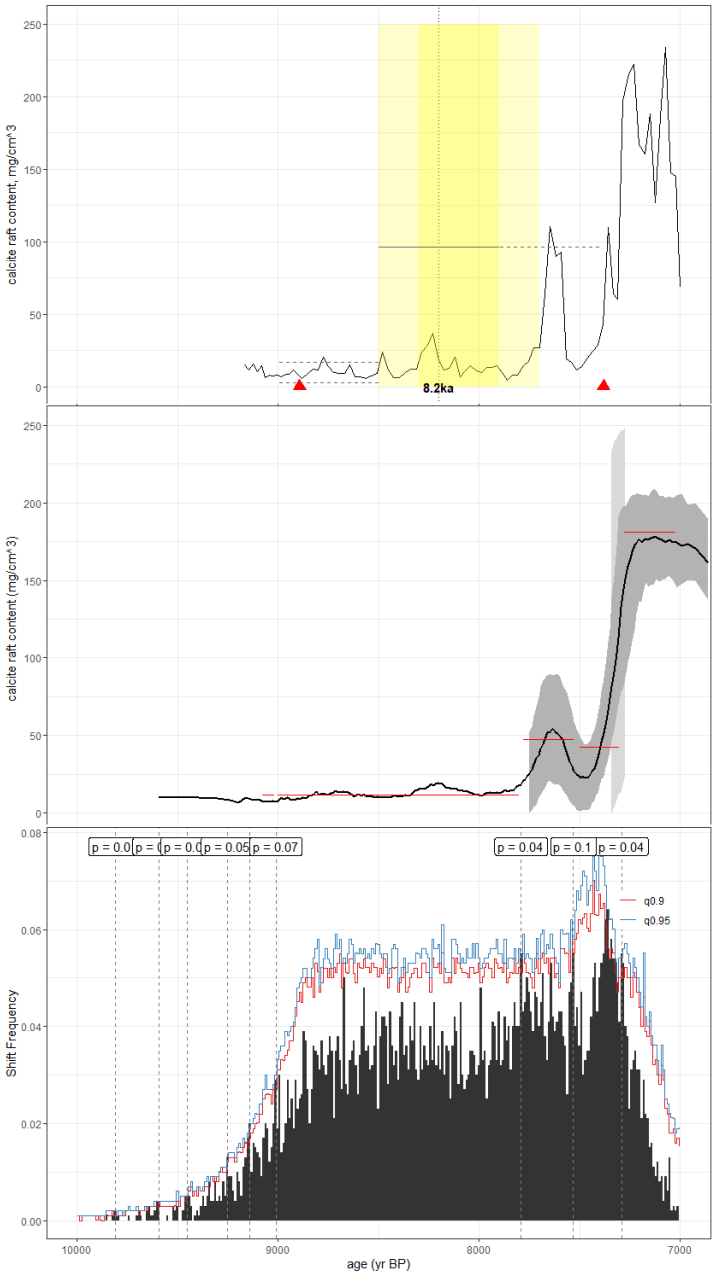

Figure C19. As in Fig. C1, but for the lacustrine calcite raft record of Sullivan et al., 2021 (C7). The published age model was constructed using the BACON algorithm and the IntCal13 calibration curve. Here, we reconstruct the BACON age ensemble using geoChronR and the IntCal20 calibration curve.

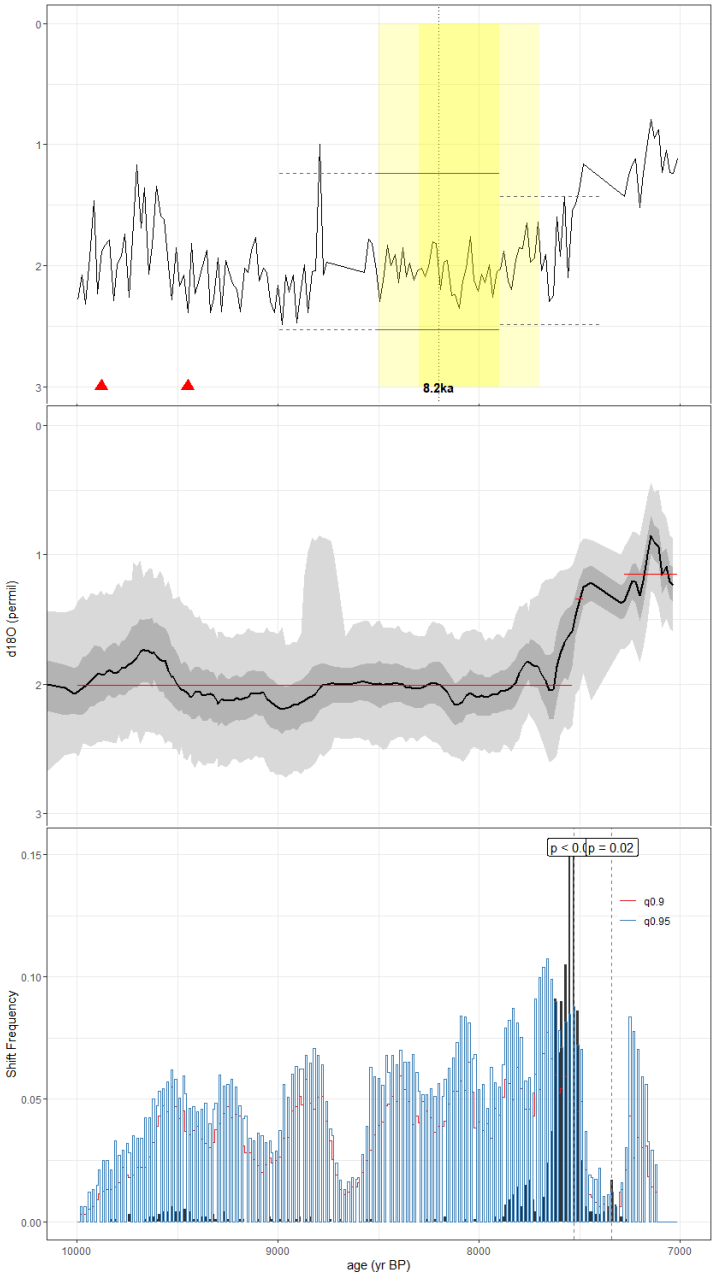

1385

Figure C20. As in Fig. C1, but for the lacustrine gastropod $\delta^{18}O$ record of Curtis et al., 1998 (Curtis6VII93). The published age model was constructed by linearly interpolating between 14C dates derived from terrestrial wood and charcoal samples. Here, we construct the age ensemble using the BACON algorithm included in geoChronR.

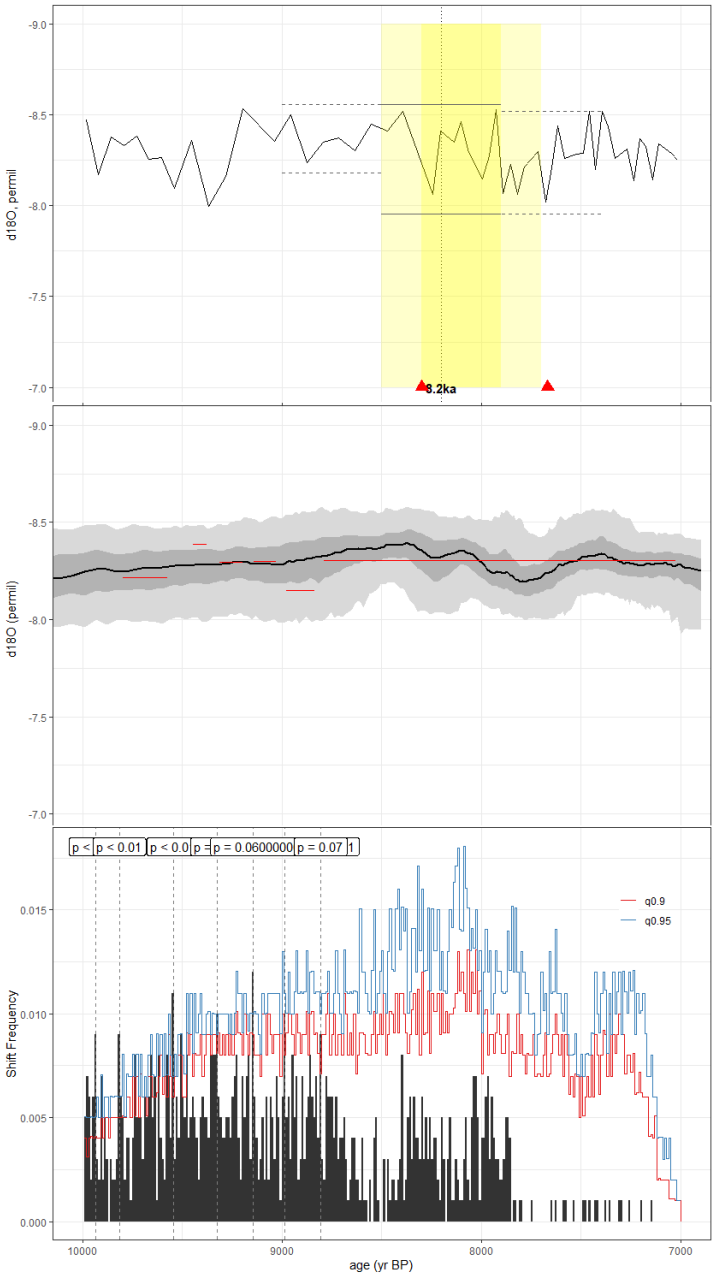

Figure C21. As in Fig. C1, but for the speleothem record of Li et al., 2011 (FR5). The age modeling algorithm used to construct the original age model was unreported, but leveraged the IntCal09 calibration curve. Here, we use the copRa age ensemble included in SISALv2.

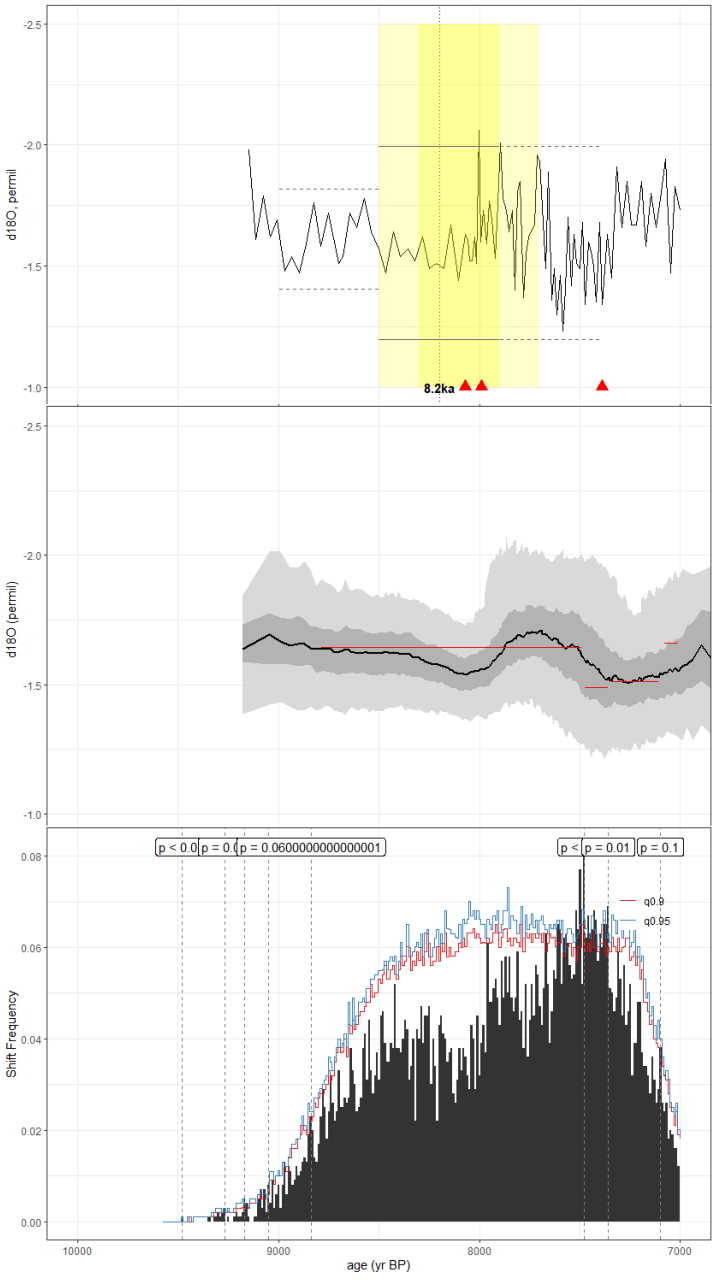

Figure C22. As in Fig. C1, but for the foraminifera record of Schmidt et al., 2012 (JPC51). The published age model was created using CALIB 6.0, with a standard -400-year reservoir age correction for surface waters. Here, we use the BACON algorithm included in geoChronR to produce our age ensemble.

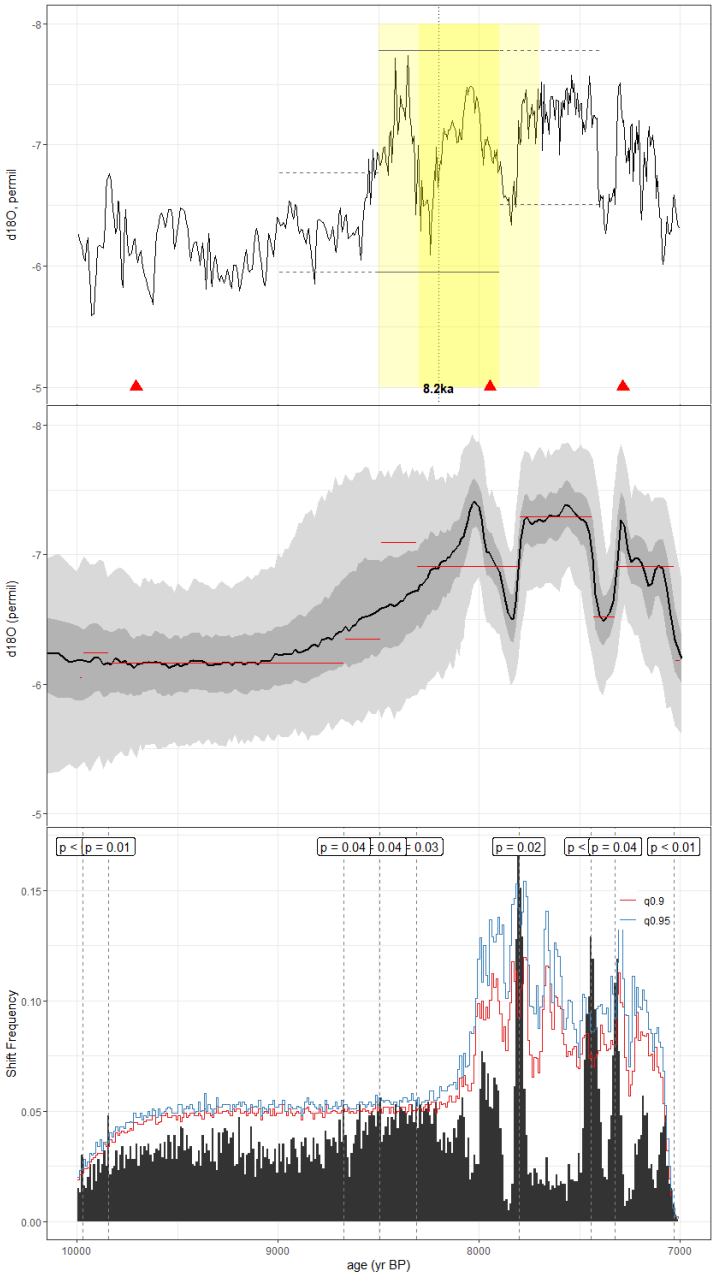

Figure C23. As in Fig. C1, but for the speleothem record of Berkelhammer et al., 2012 (KMA). The published age model was created using the StalAge algorithm. Here, we used the BACON age ensemble included in SISALv2.

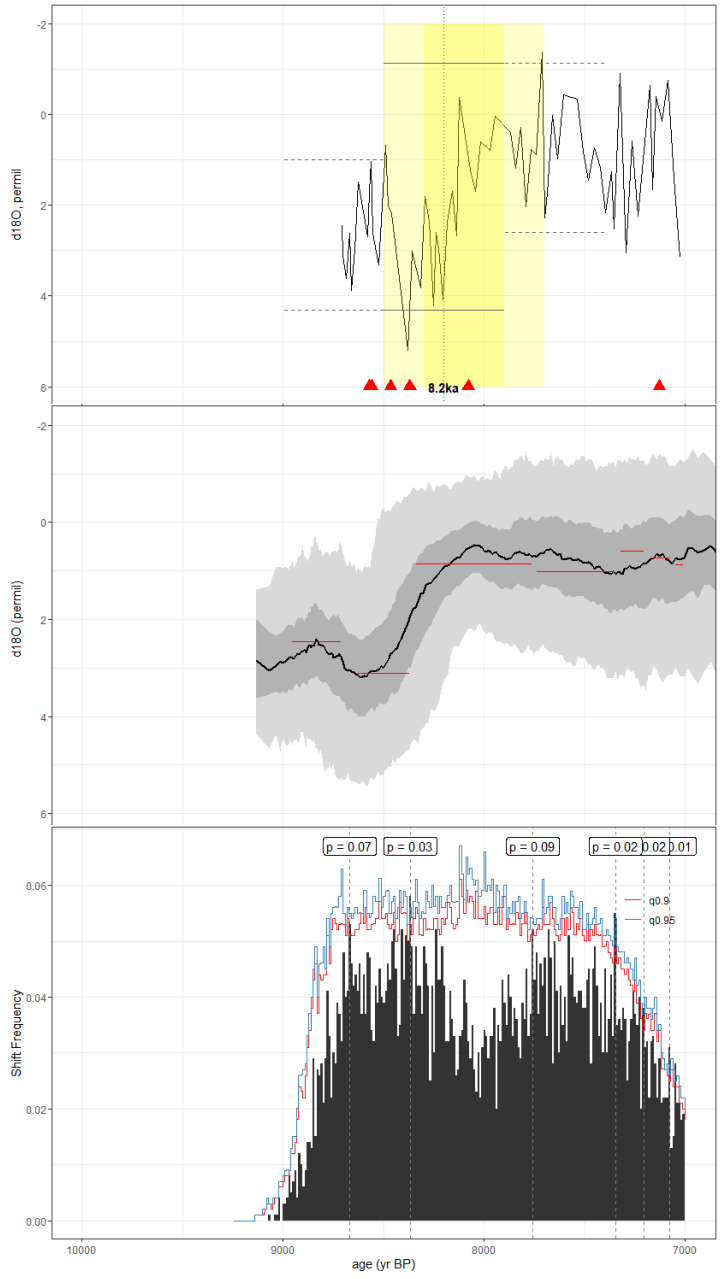

Figure C24. As in Fig. C1, but for the lake sediment $\delta^{18}O$ record of Wahl et al., 2014 (LagoPuertoArturo). The published age model was constructed using CLAM 2.2 and the IntCal13 calibration curve. For our analyses, we reconstructed the age model using BACON and IntCal20 in geoChronR.

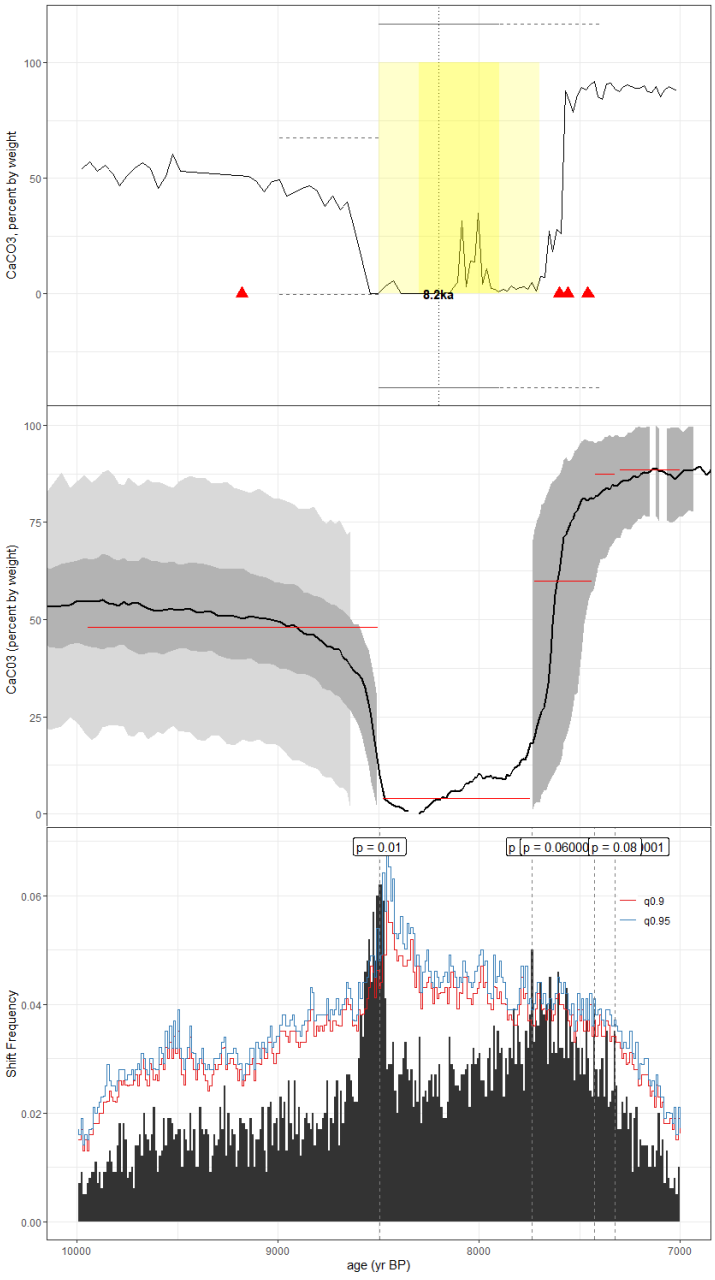

Figure C25. As in Fig. C1, but for the lake sediment record of Hodell et al., 1995 (LC1). The published age model was created using the decadal tree ring dataset in CALIB. Here, we use BACON with the IntCal20 calibration curve supplied by geoChronR.

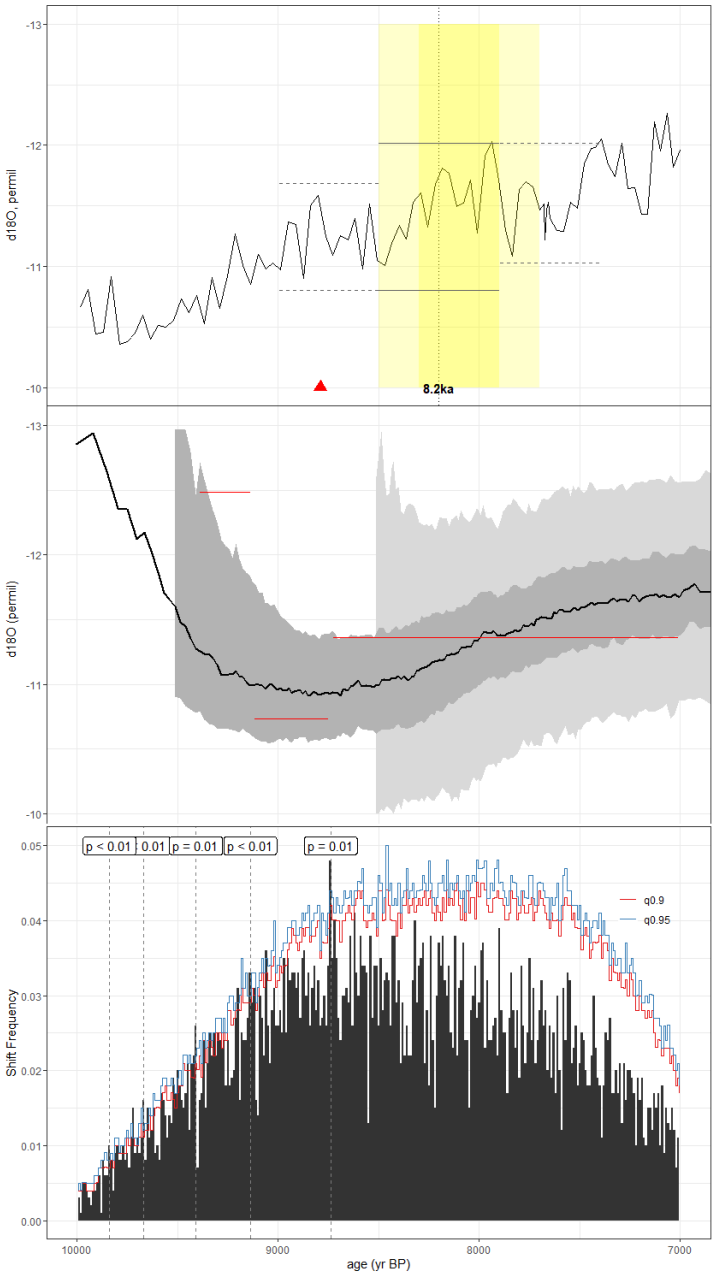

Figure C26. As in Fig. C1, but for the lacustrine sediment record of Bird et al., 2011 (LP). The published age model was created using CALIB 5.0 with an unreported calibration curve. Here, we construct our age ensemble in geoChronR using the BACON algorithm and SHCal20.

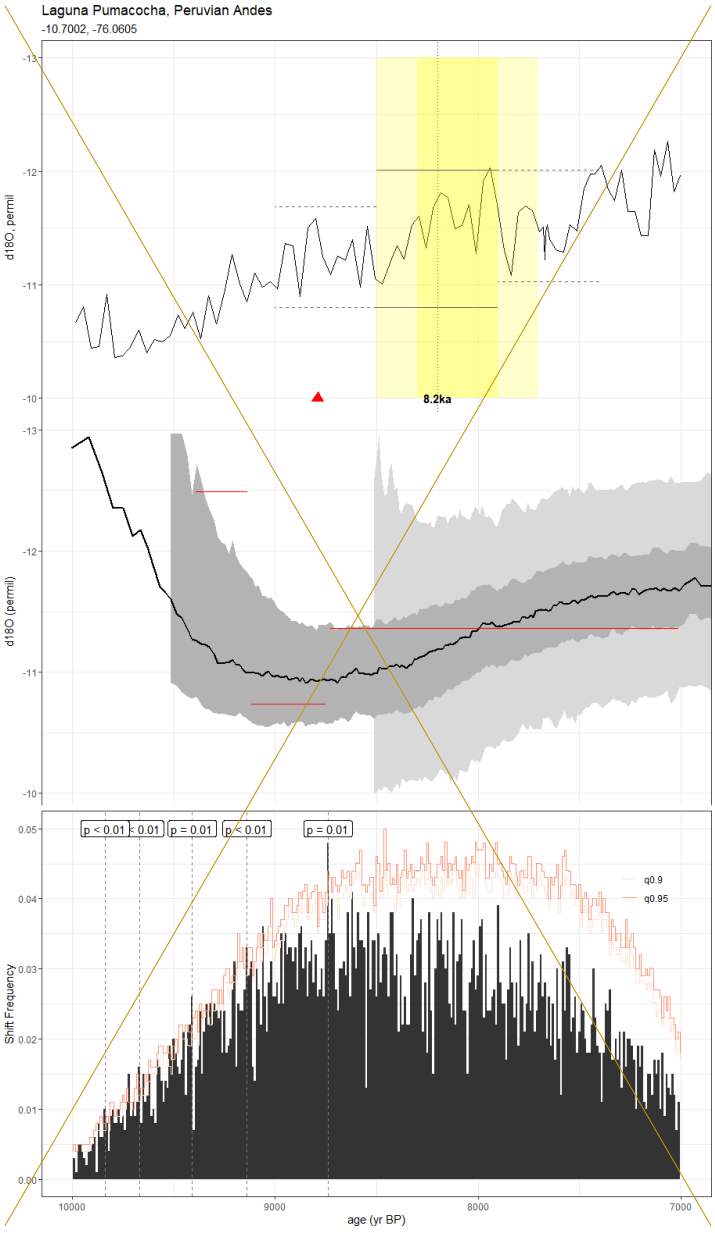

Figure C26. As in Fig. C1, but for the lacustrine sediment record of Bird et al., 2011 (LP). The published age model was created using CALIB 5.0 with an unreported calibration curve. Here, we construct our age ensemble in geoChronR using the BACON algorithm and SHCal20.

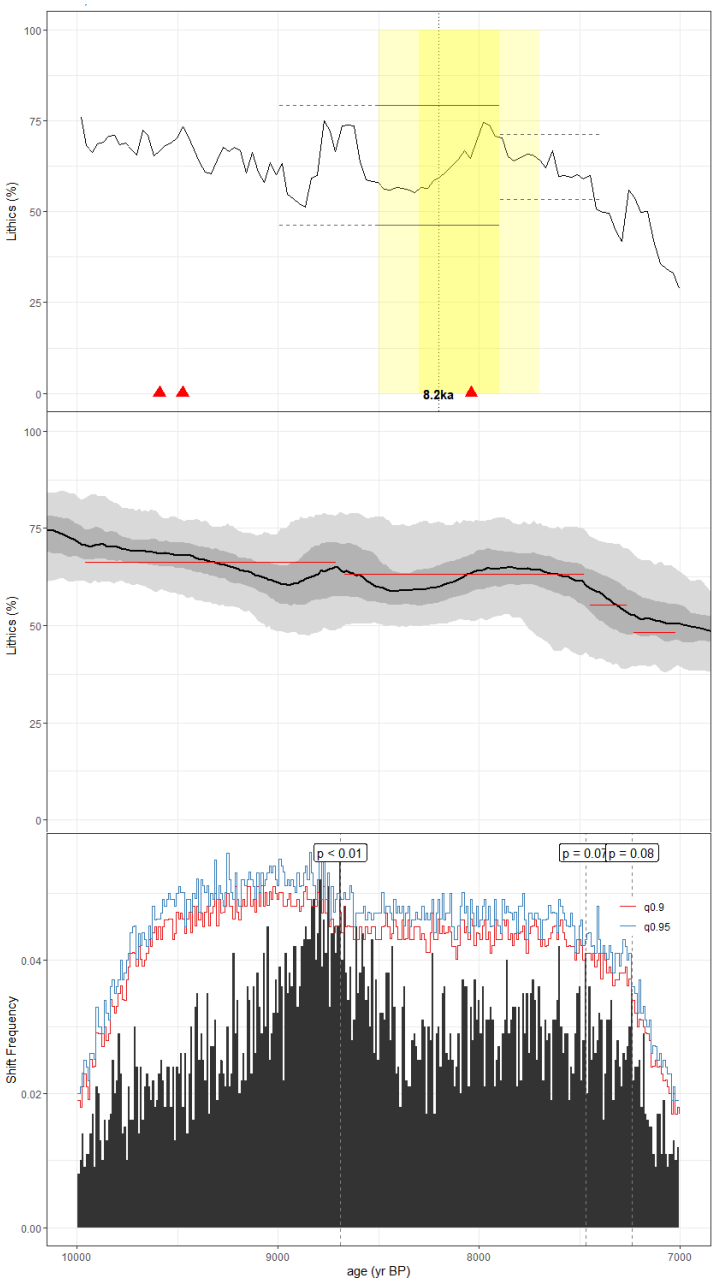

Figure C27. As in Fig. C1, but for the lake sediment (percent lithics) record of Bird et al., 2014 (ParuCo). CALIB 6.0 and the IntCal09 calibration curve were used in the construction of the published age model. We construct our age ensemble using BACON and IntCal20 via geoChronR.

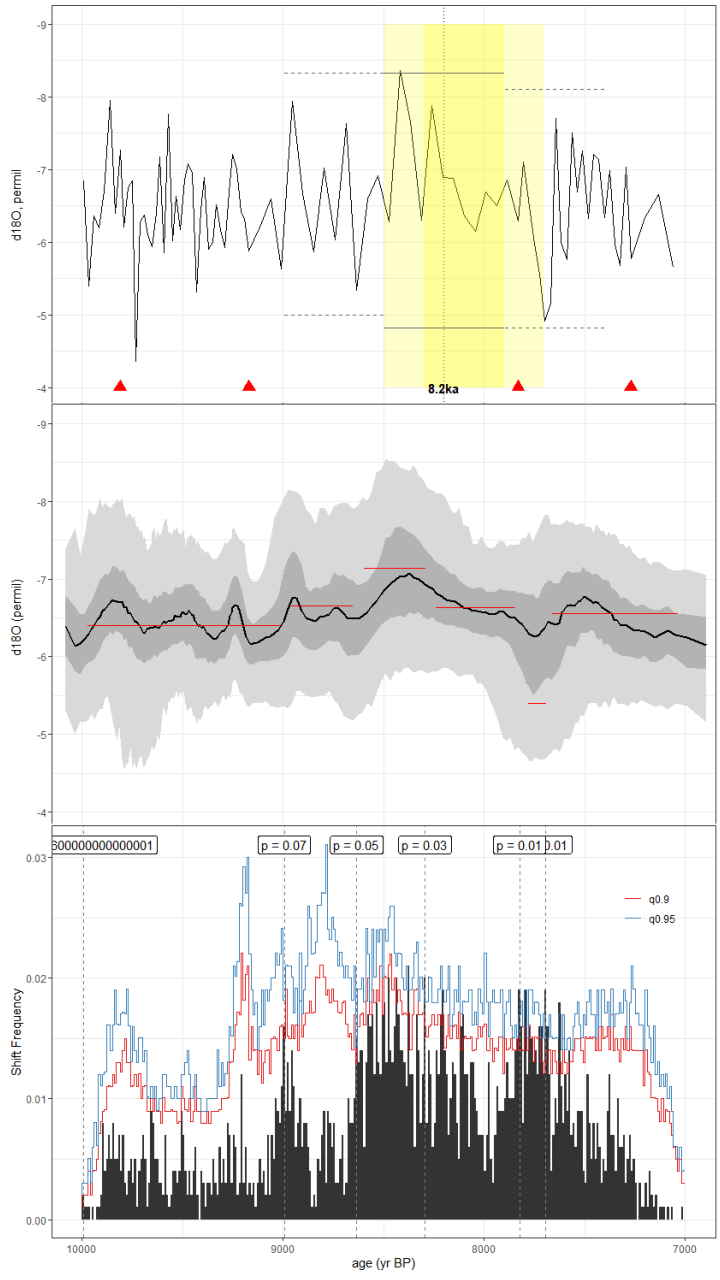

Figure C28. As in Fig. C1, but for the speleothem record of Cruz et al., 2009 (RN1). The method used in the construction of the published age model was unreported, but we leverage the Bchron ensemble supplied in version 2 of the SISAL database for our analyses.

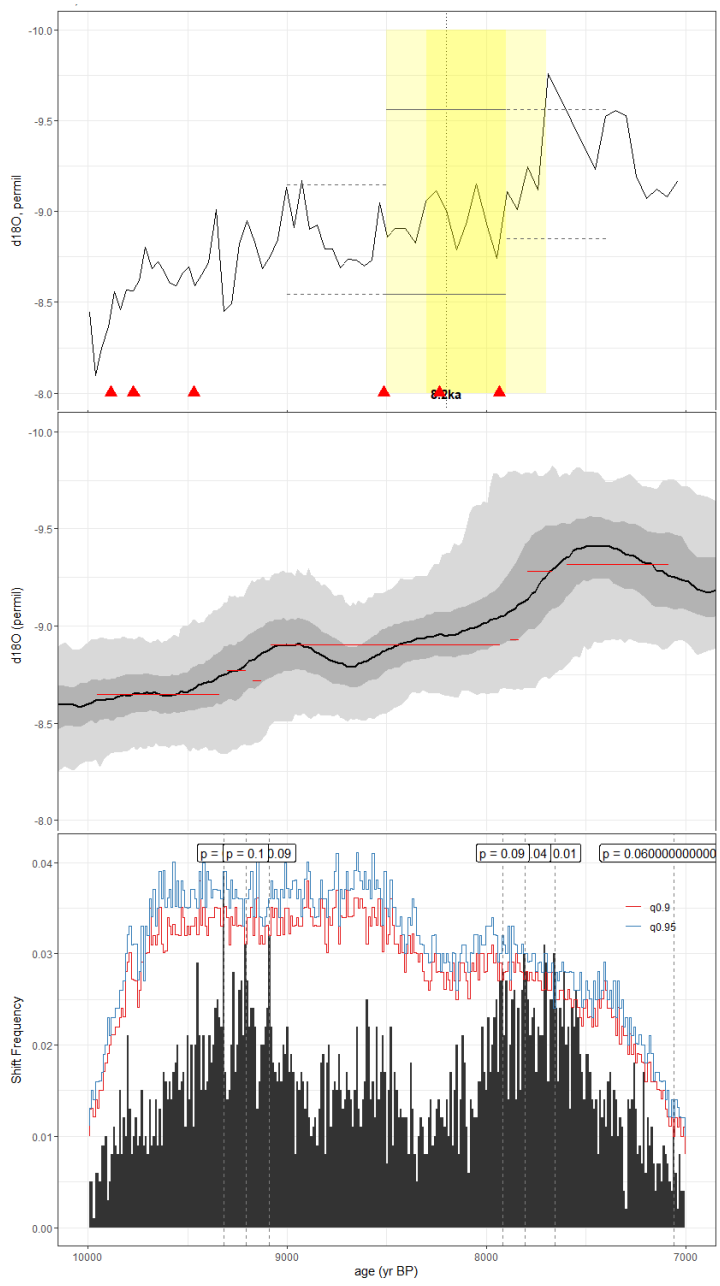

Figure C29. As in Fig. C1, but for the speleothem record of Carolin et al., 2016 (SSC01). StalAge was used to construct the published age model. We used the BACON algorithm included in geoChronR to generate our age ensemble.

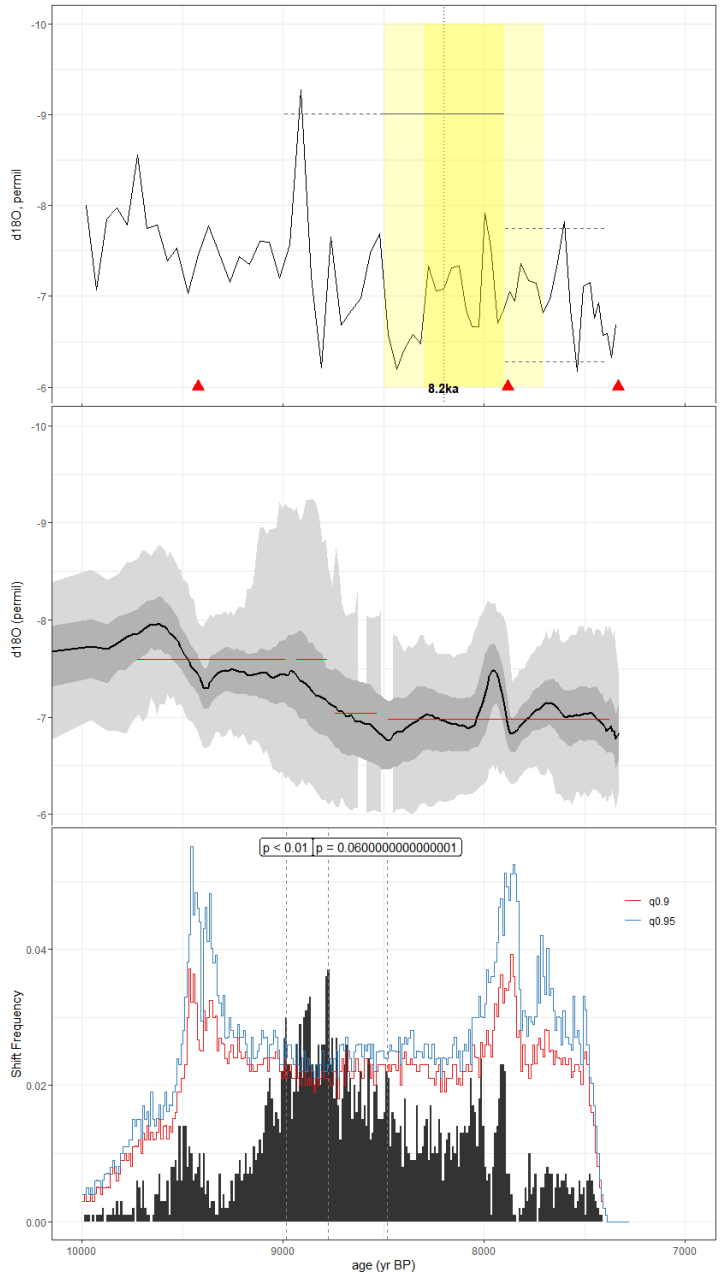

Figure C30. As in Fig. C1, but for the speleothem record of Ward et al., 2019 (TM6). The published age model was constructed using the copRa algorithm, though we use the BACON age ensemble supplied in the SISALv2 database for our analyses.

C4 Records with conflicting signals in actR and MM

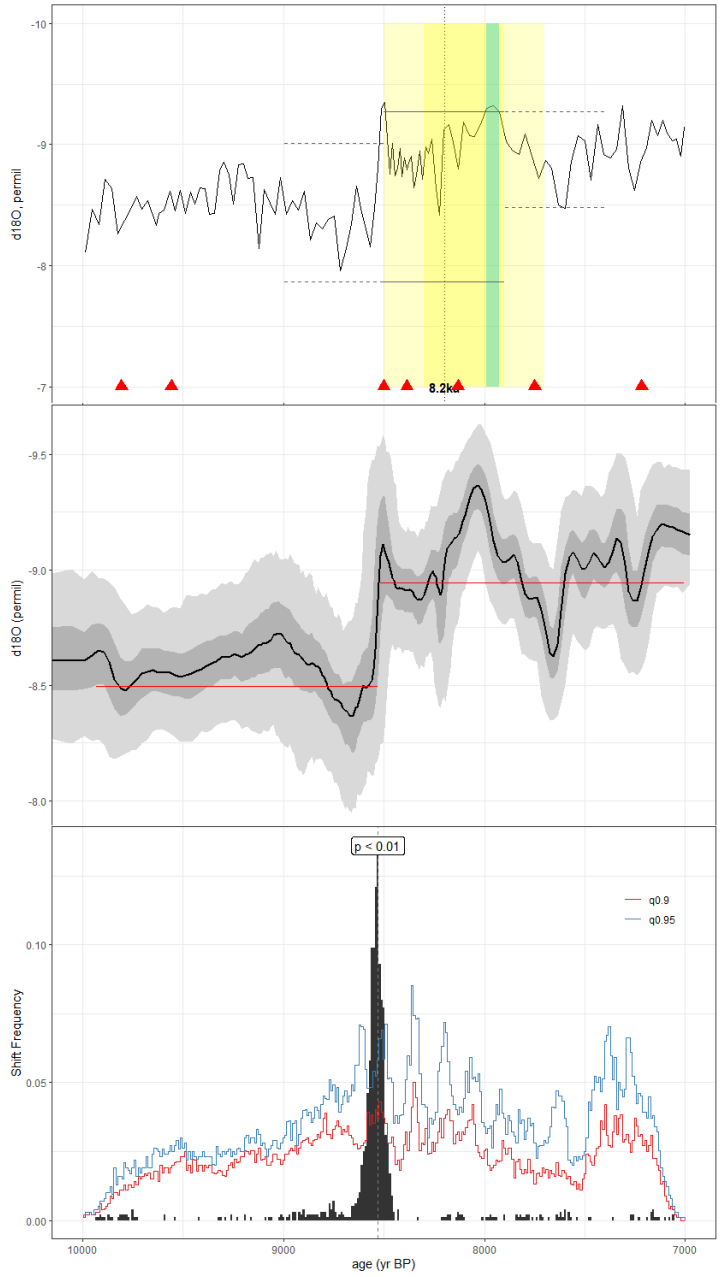

Figure C31. As in Fig. C1, but for the speleothem record of Chen et al., 2016 (BA03). The published age model was based on the StalAge algorithm, but here, we use the BACON ensemble from SISALv2.

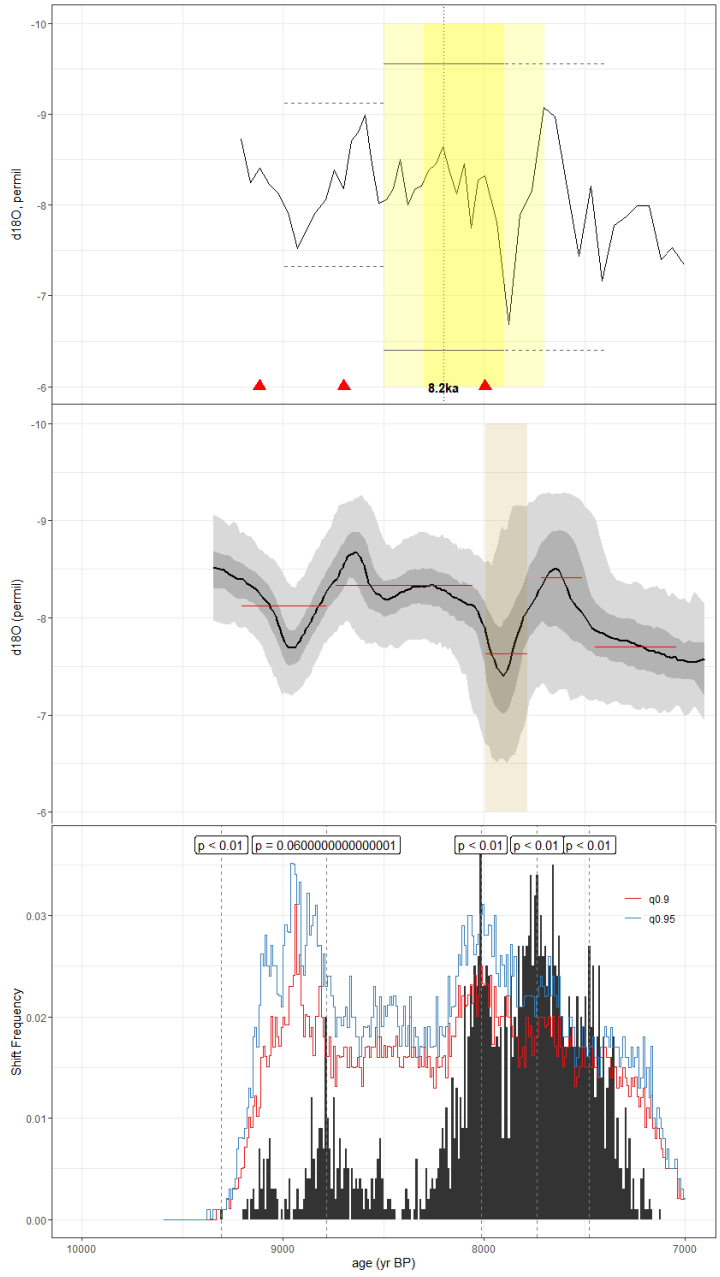

Figure C32. As in Fig. C1, but for the speleothem record of Bernal et al., 2016 (BTV21a). Information about the published age model was unreported. Here, we use the SISALv2 BACON age ensemble.

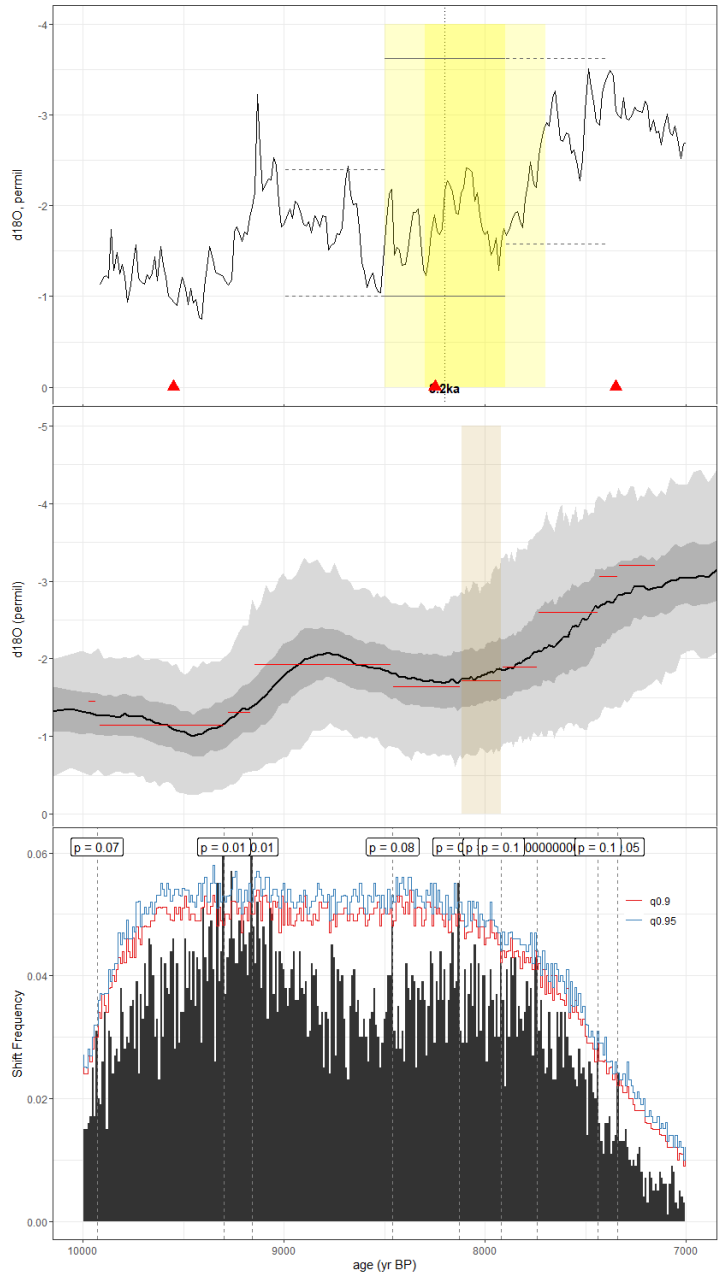

Figure C33. As in Fig. C1, but for the speleothem record of Fensterer et al., 2013 (CM2013). The published age model was constructed using the StalAge algorithm. Here, we use the SISALv2 copRa age ensemble.

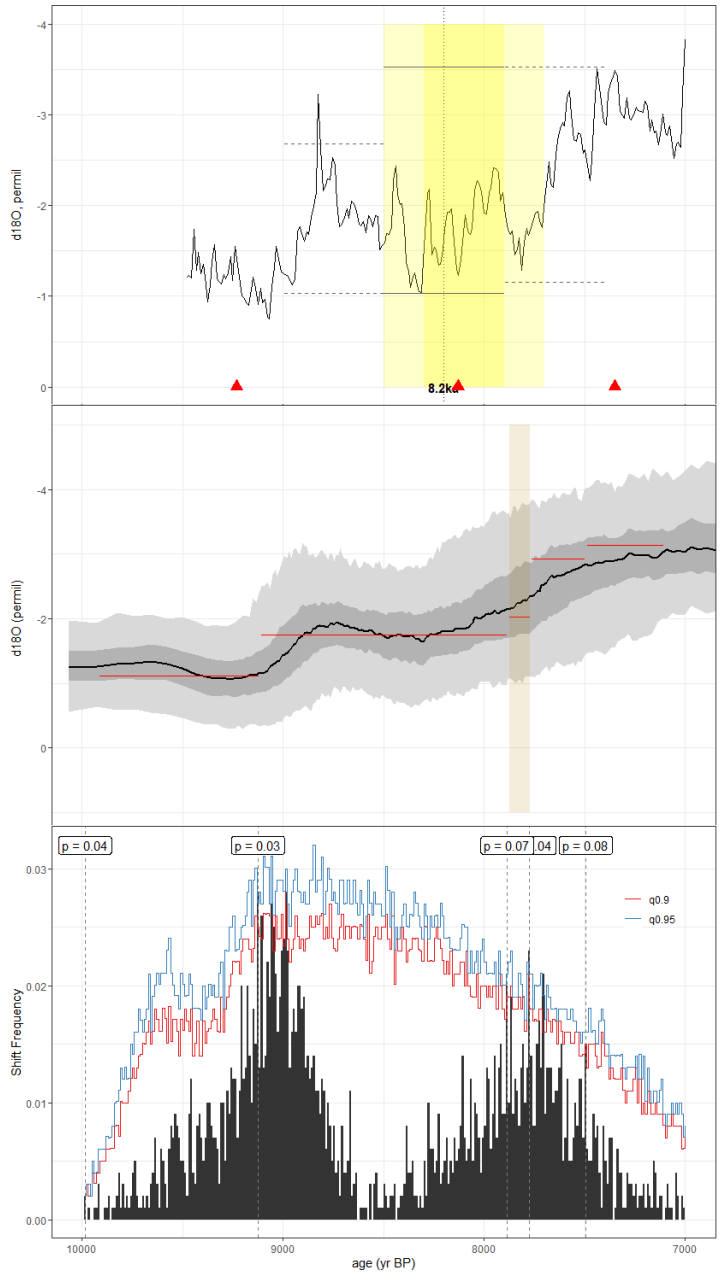

Figure C34. As in Fig. C1, but for the speleothem record of Warken et al., 2019 (CM2019). The published age model was constructed using the StalAge algorithm. Here, we use the SISALv2 BACON age ensemble.

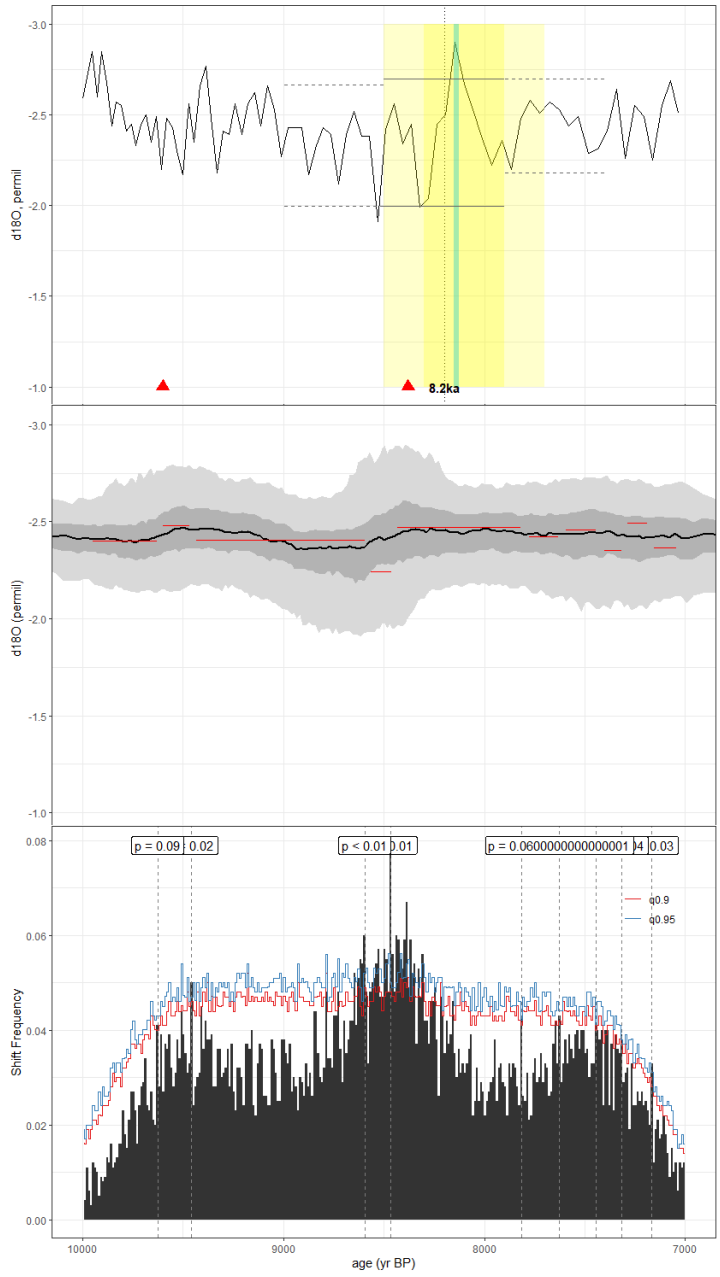

Figure C35. As in Fig. C1, but for the foraminifera record of Wang et al., 1999 (Core17940). The published age model was constructed using CALIB 3.0.3, corrected for a 400-year reservoir age and unspecified calibration curve. We constructed our age ensemble using the BACON algorithm included in geoChronR using the IntCal20 calibration curve.

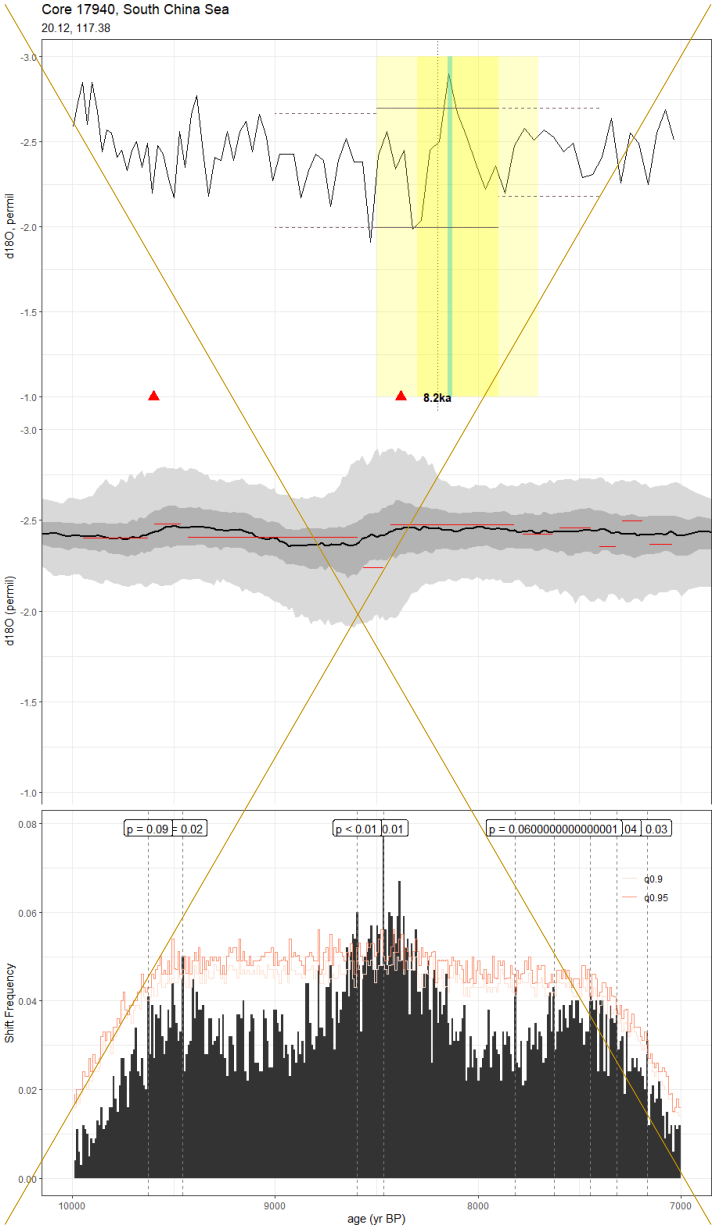

Figure C35. As in Fig. C1, but for the foraminifera record of Wang et al., 1999 (Core17940). The published age model was constructed using CALIB 3.0.3, corrected for a 400-year reservoir age and unspecified calibration curve. We constructed our age ensemble using the BACON algorithm included in geoChronR using the IntCal20 calibration curve.

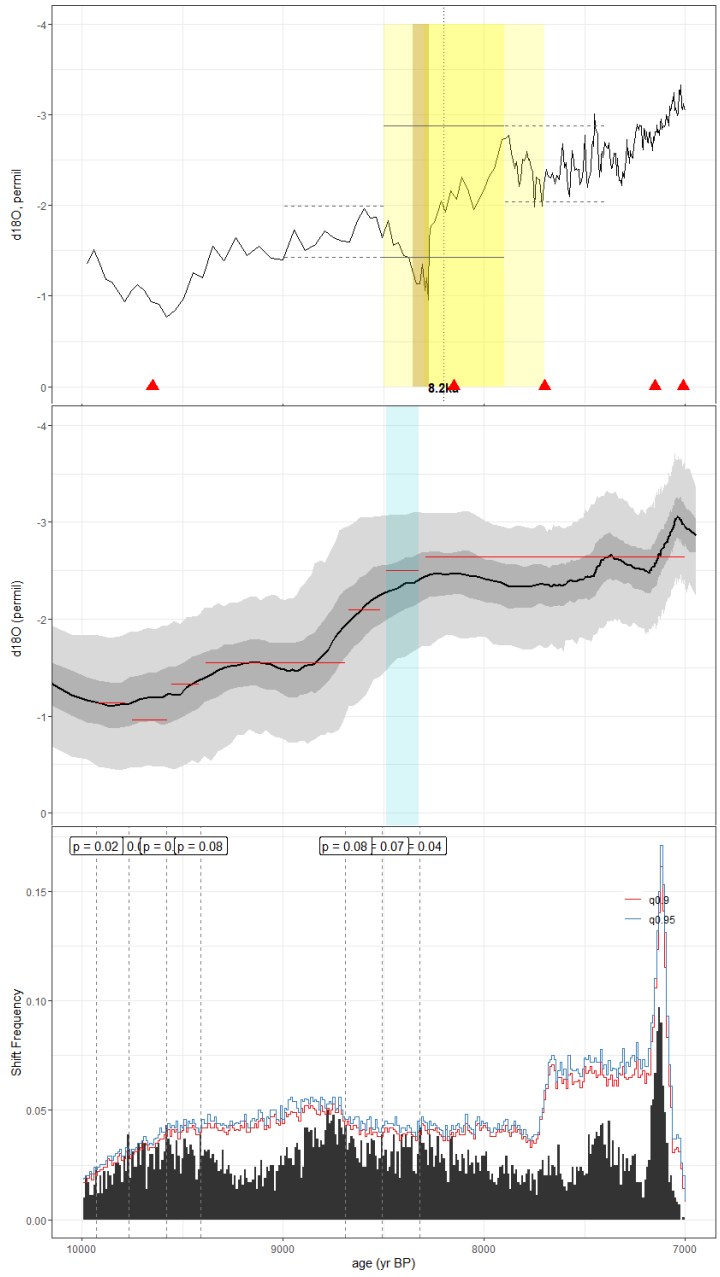

Figure C36. As in Fig. C1, but for the speleothem record of Fensterer et al., 2013 (CP). The published age model was constructed using the StalAge algorithm. We use the Bchron age ensemble constructed in SISALv2 here.

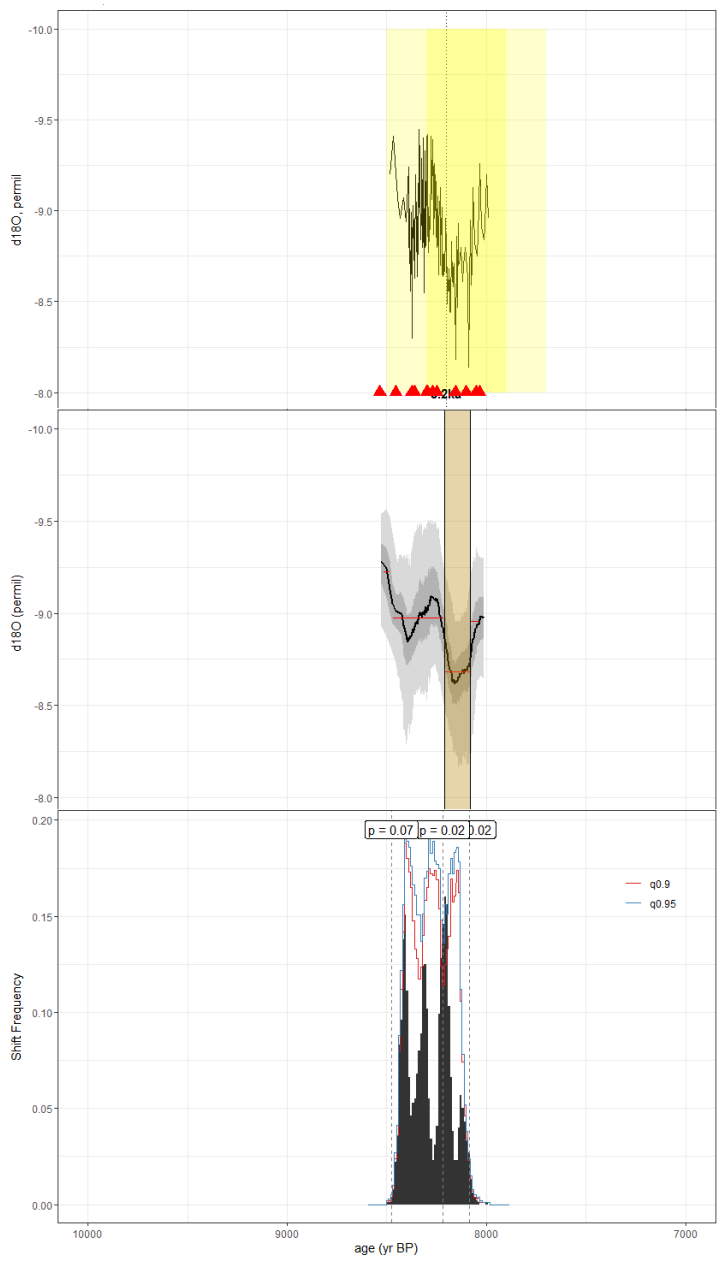

Figure C37. As in Fig. C1, but for the speleothem record of Cheng et al., 2009 (D4Cheng). The age model used in the original publication was unreported. Here, we use the BACON algorithm included in geoChronR to produce our age ensemble.

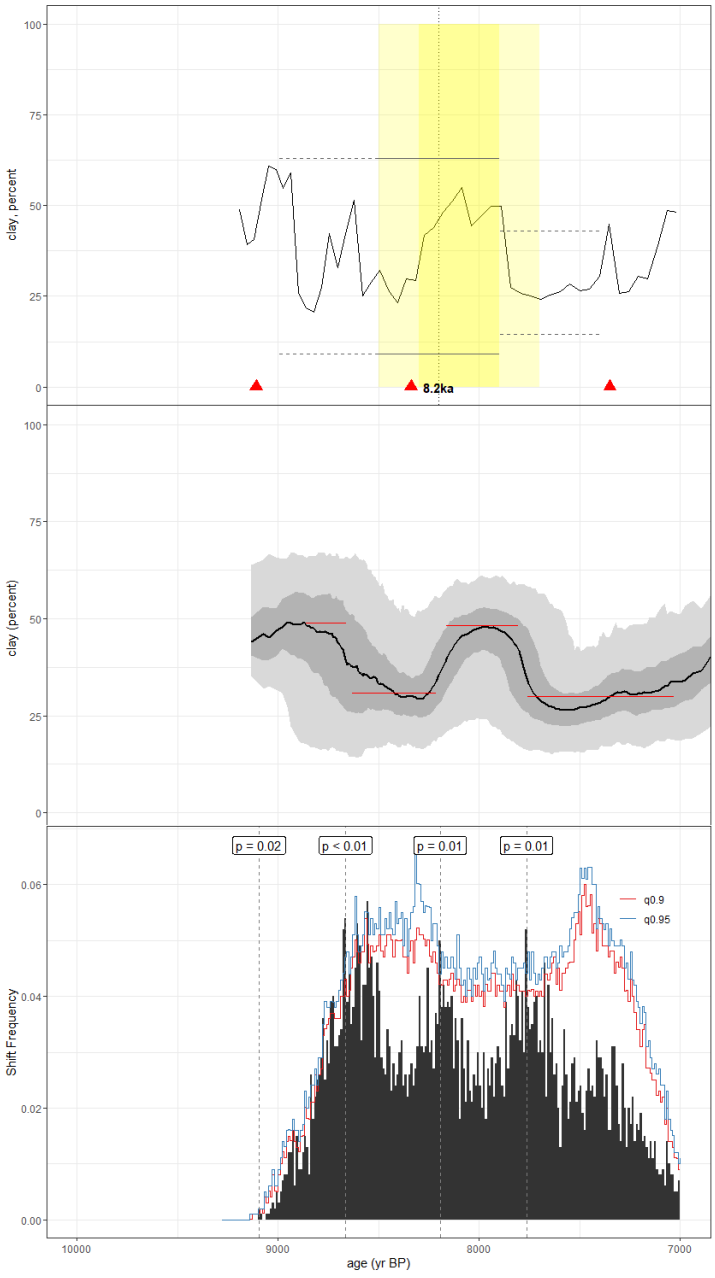

Figure C38. As in Fig. C1, but for the lacustrine clay content record of Conroy et al., 2008 (EJConroy). The published age model was constructed using CALIB 5.0 with the Southern Hemisphere dataset. The age ensemble presented here was created using the BACON algorithm with the SHCal20 calibration curve in geoChronR.

Figure C38. As in Fig. C1, but for the lacustrine clay content record of Conroy et al., 2008 (EJConroy). The published age model was constructed using CALIB 5.0 with the Southern Hemisphere dataset. The age ensemble presented here was created using the BACON algorithm with the SHCal20 calibration curve in geoChronR.

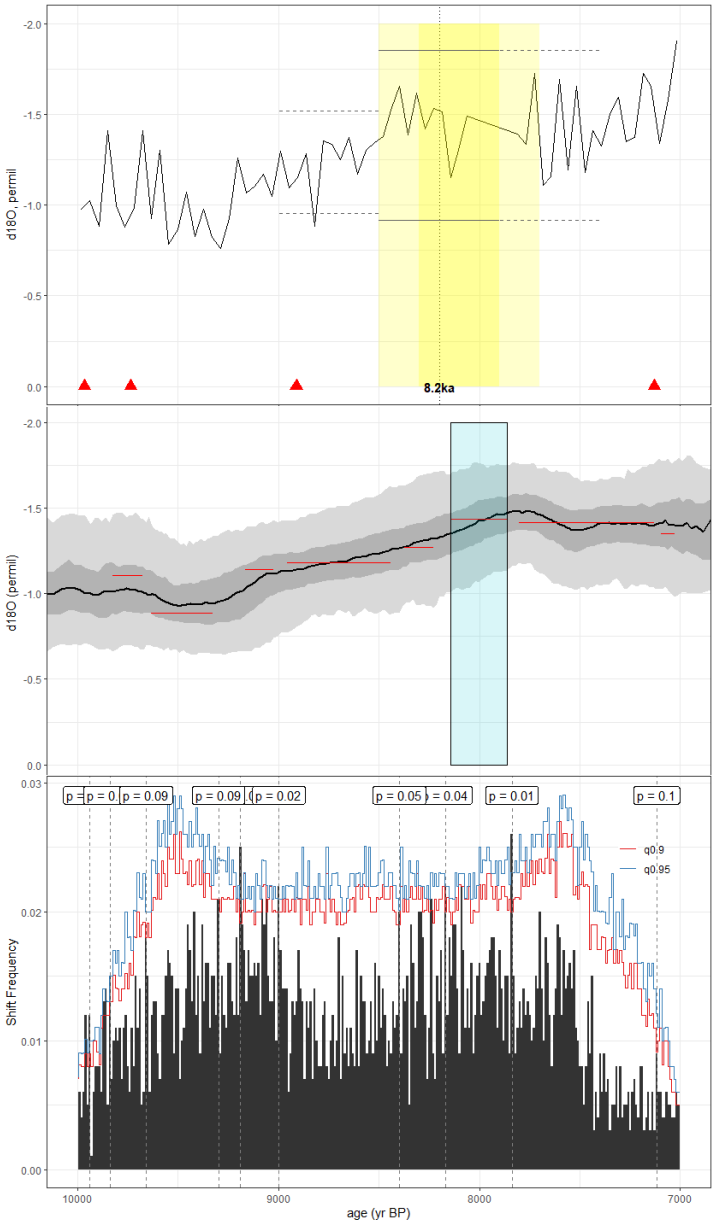

Figure C39. As in Fig. C1, but for the foraminifera record of Thirumulai et al., 2021 (GB2GC1). The published age model was developed using the BACON algorithm and Marine13 calibration curve, which we reconstructed using geoChronR.

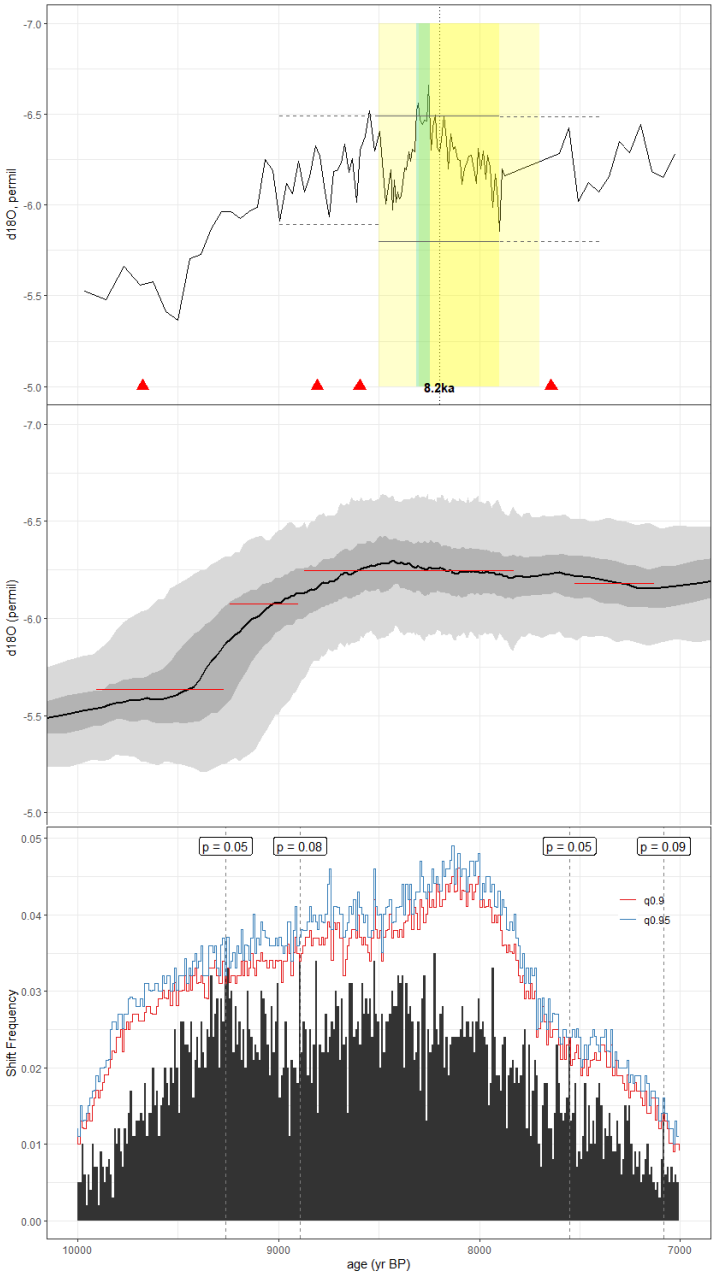

Figure C40. As in Fig. C1, but for the speleothem record of Winter et al., 2020 (GURM1). The published age model was constructed using the copRa algorithm, while we use the BACON ensemble produced for SISALv2 here.

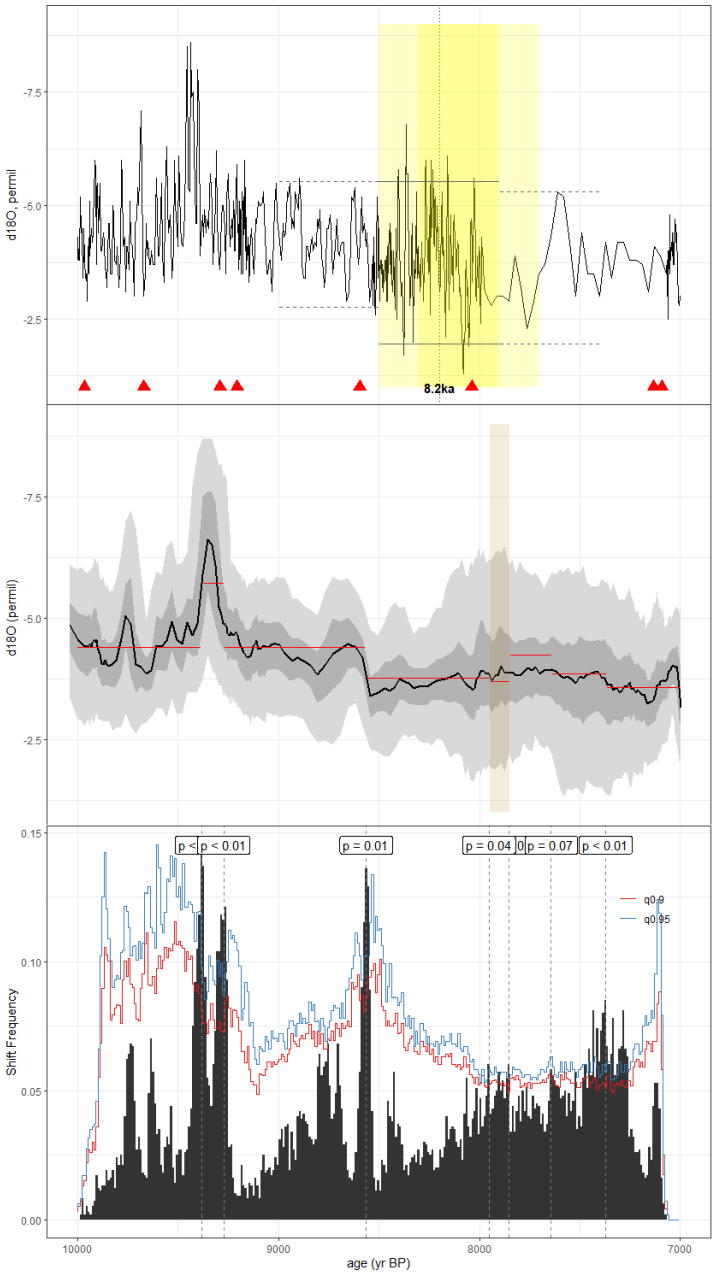

Figure C41. As in Fig. C1, but for the speleothem record of Novello et al., 2017 (JAR7). The published age model was constructed via linear interpolation between radiometric dates. For our analyses, we leveraged the BACON age ensemble produced for SISALv2.

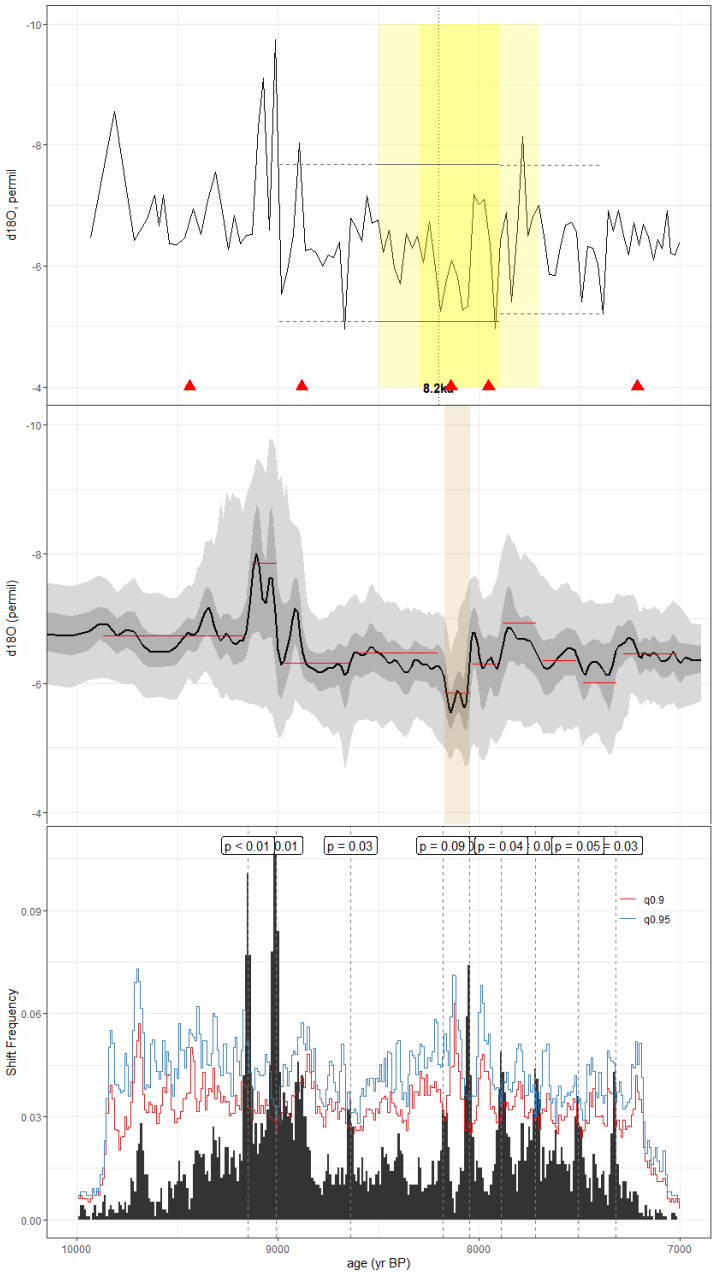

Figure C42. As in Fig. C1, but for the speleothem record of Huguet et al., 2018 (KM1). While the published age model was constructed using the StalAge algorithm, we leverage the Bchron age ensemble included in SISALv2 here.

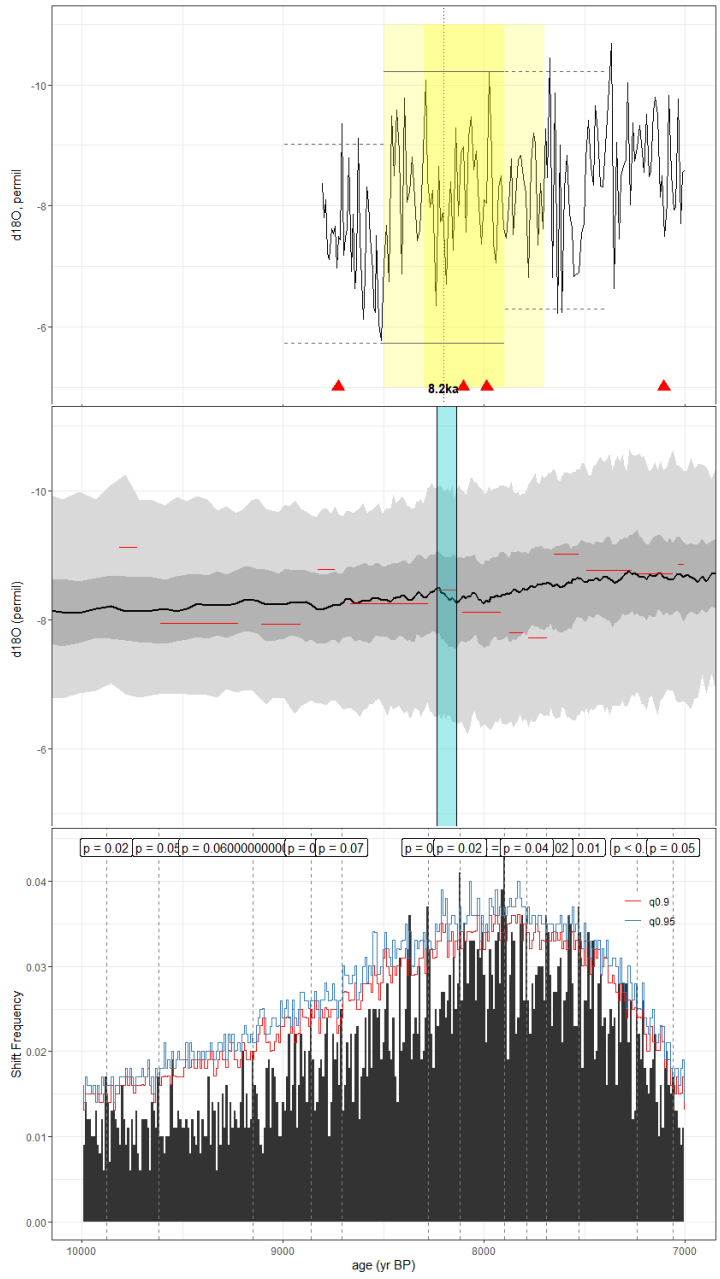

Figure C43. As in Fig. C1, but for the speleothem record of Denniston et al., 2013 (KN51). The method used in the construction of the published age model is unknown, but we use the copRa ensemble generated for SISALv2 here.

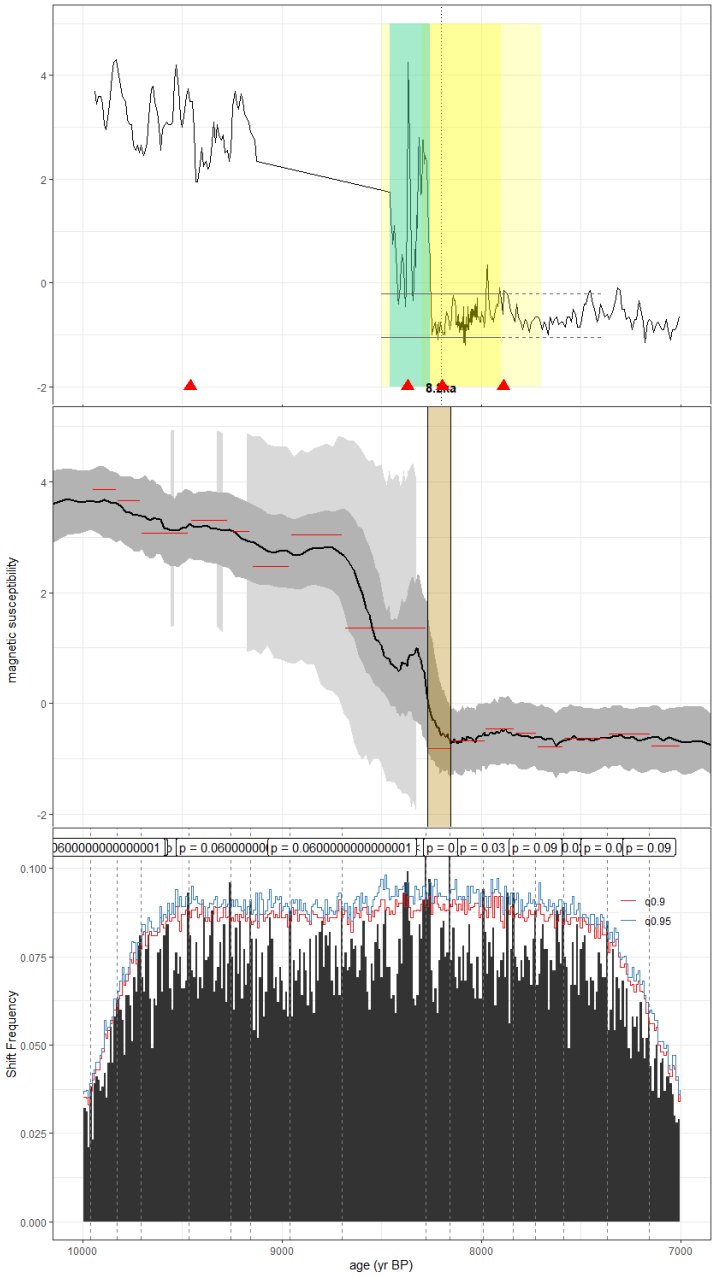

Figure C44. As in Fig. C1, but for the lake sediment magnetic susceptibility record of Pollisar et al., 2013 (LBA99). The published age model was constructed by linearly interpolating between radiometric dates with the IntCal04 calibration curve. Here, we constructed our ensemble using the BACON algorithm and IntCal20 curve included in geoChronR.

~~**Figure C44.** As in Fig. C1, but for the lake sediment magnetic susceptibility record of Pollisar et al., 2013 (LBA99). The published age model was constructed by linearly interpolating between radiometric dates with the IntCal04 calibration curve. Here, we constructed our ensemble using the BACON algorithm and IntCal20 curve included in geoChronR.~~

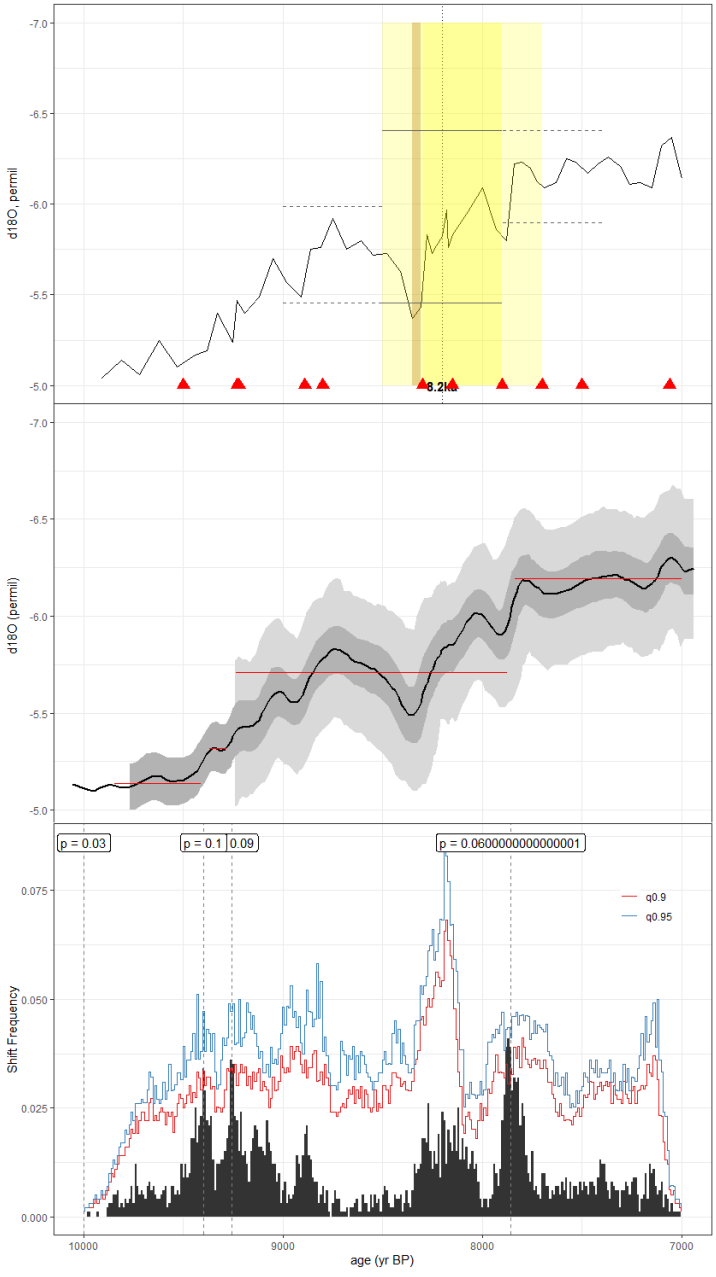

Figure C45. As in Fig. C1, but for the speleothem record of Ayliffe et al., 2013 (LR06_B3_2013). The published age model was constructed by linearly interpolating between radiometric dates. For our analyses, we leveraged the Bchron ensemble published in the

SISALv2 dataset.

Figure C45. As in Fig. C1, but for the speleothem record of Ayliffe et al., 2013 (LR06_B3_2013). The published age model was constructed by linearly interpolating between radiometric dates. For our analyses, we leveraged the Bchron ensemble published in the SISALv2 dataset.

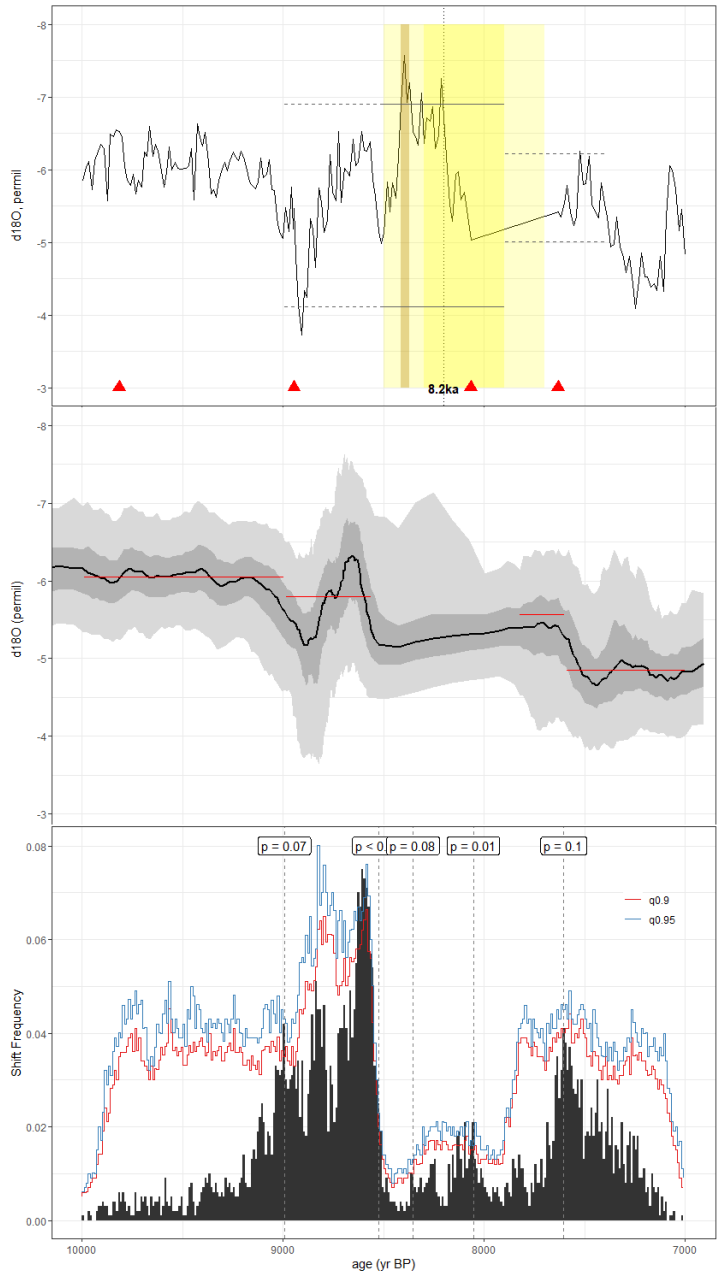

Figure C46. As in Fig. C1, but for the speleothem record of Azevedo et al., 2021 (LSF19). The original method used in the construction of the published age model was unreported, but we use the BACON ensemble supplied in version 2 of the SISAL database for our analyses.

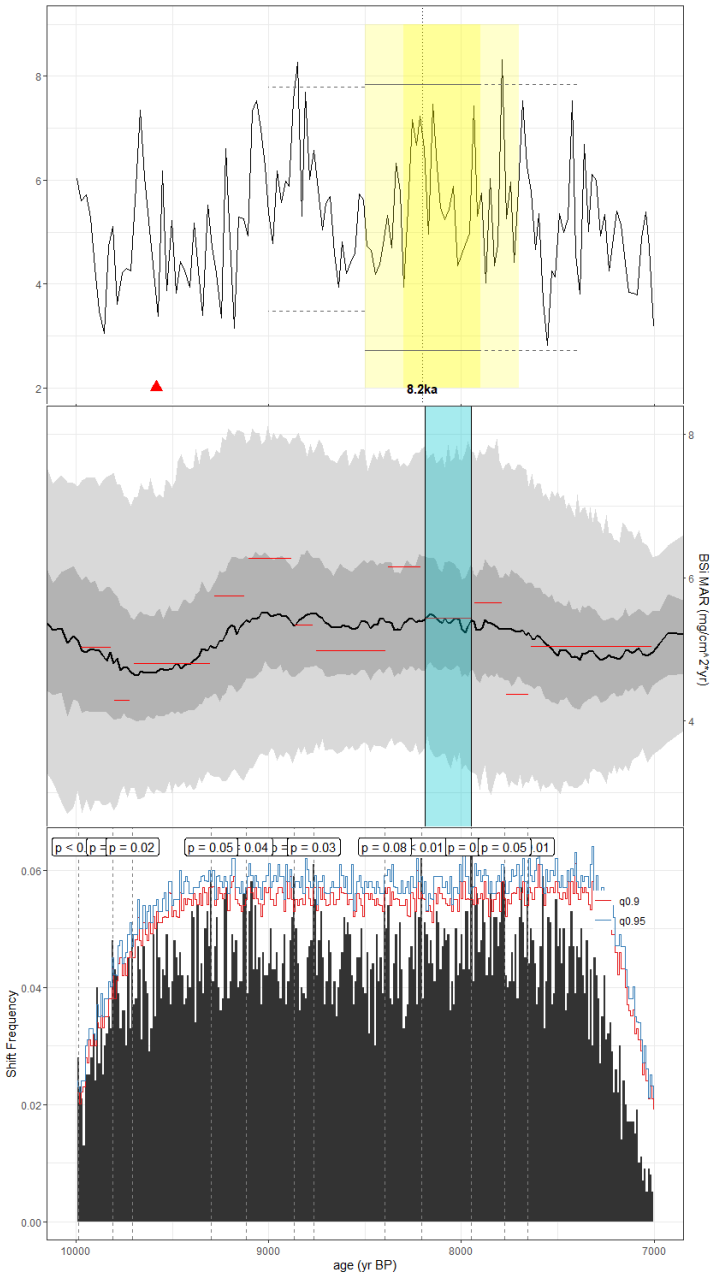

Figure C47. As in Fig. C1, but for the lake sediment BSi MAR record of Johnson et al., 2003 (M981P). CALIB 4.3 was used in the construction of the published age model, with a reservoir age correction of -450 years applied to the radiometric dates. Here, we constructed the age ensemble using the BACON algorithm in geoChronR.

~~**Figure C47.** As in Fig. C1, but for the lake sediment BSi MAR record of Johnson et al., 2003 (M981P). CALIB 4.3 was used in the construction of the published age model, with a reservoir age correction of -450 years applied to the radiometric dates. Here, we constructed the age ensemble using the BACON algorithm in geoChronR.~~

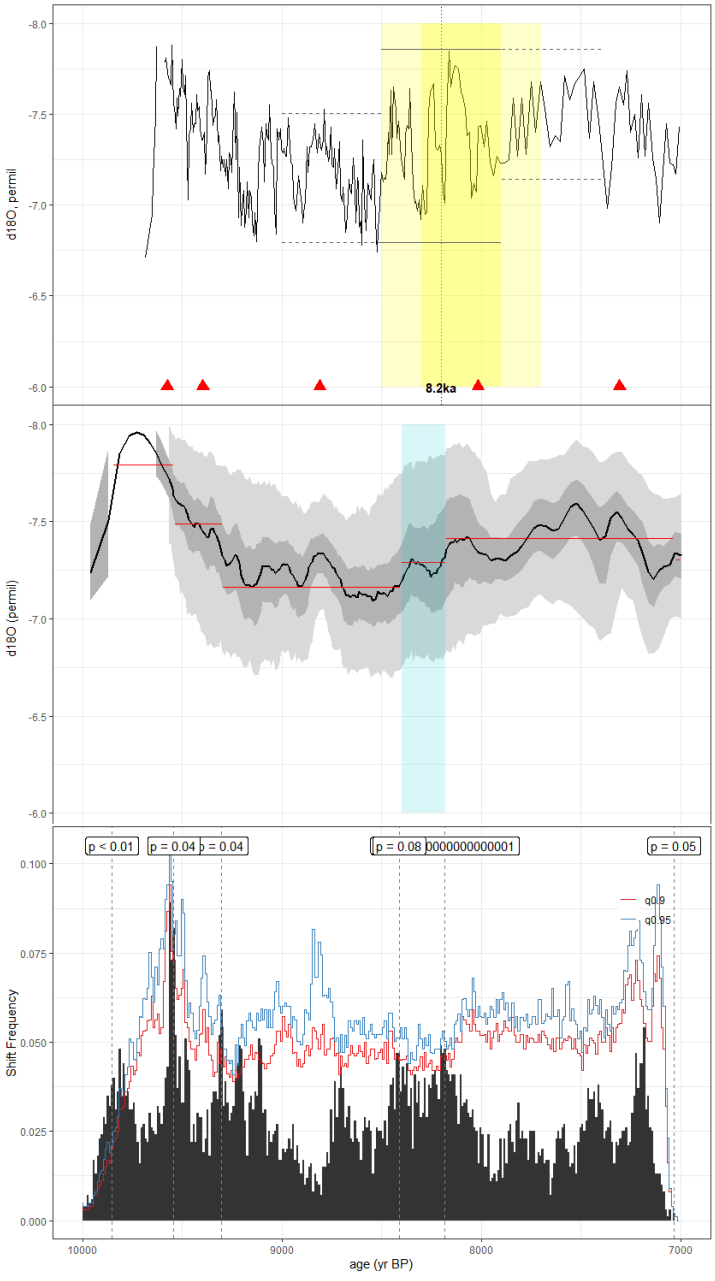

Figure C48. As in Fig. C1, but for the speleothem record of Lechleitner et al., 2017 (MAW6). The published age model was constructed using copRa. Here, we employed the Bchron ensemble included in SISALv2.

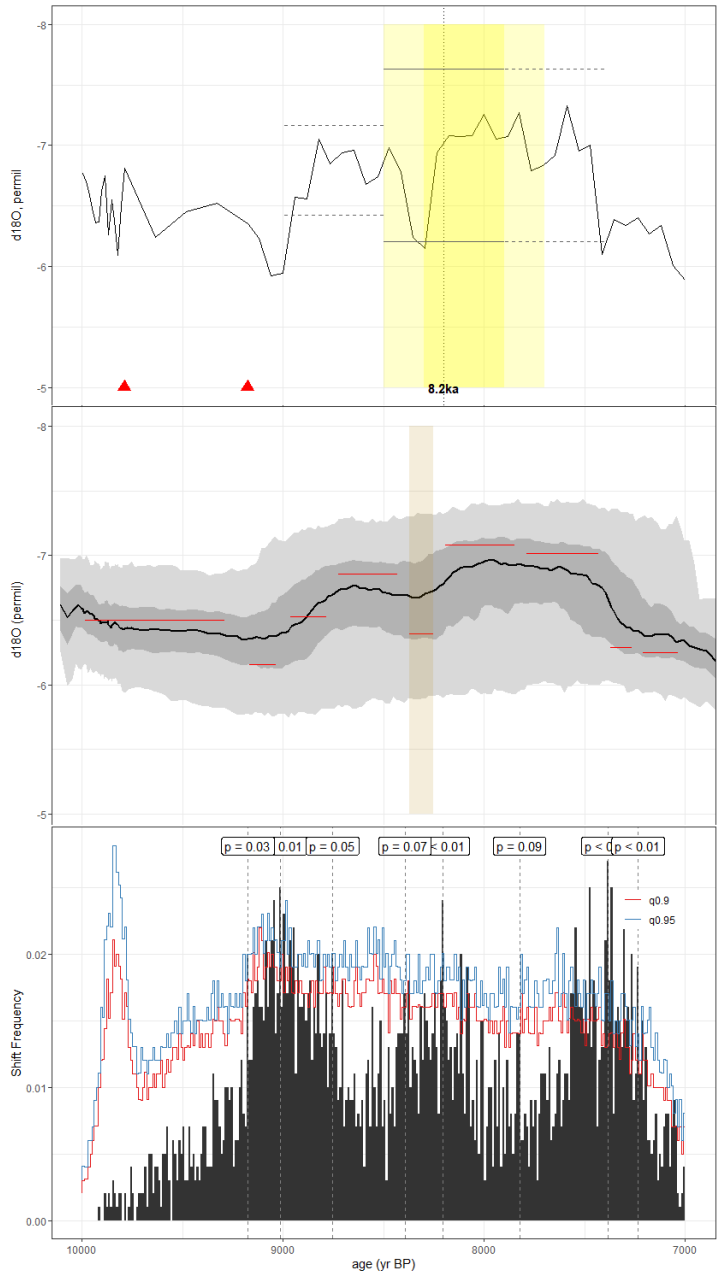

1575

Figure C49. As in Fig. C1, but for the speleothem record of Dutt et al., 2015 (MWS1). The published age model was created using the StalAge algorithm. Here, we use the Bchron ensemble from SISALv2.

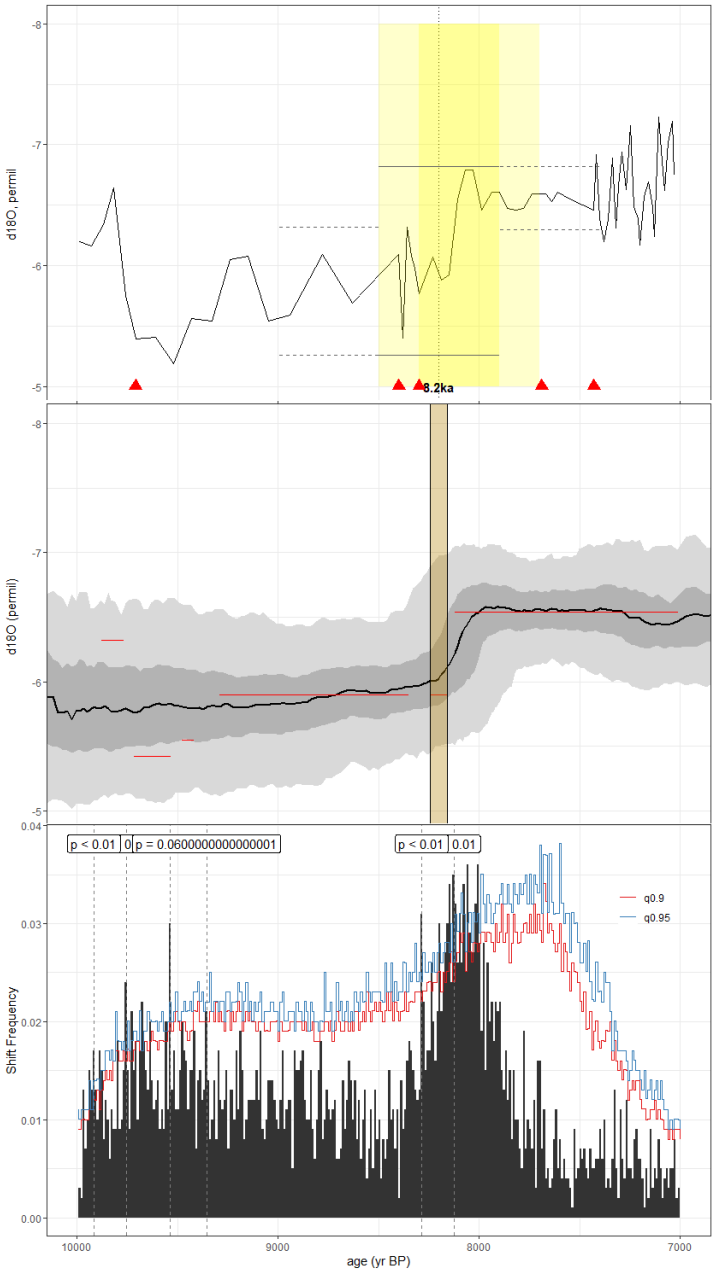

Figure C50. As in Fig. C1, but for the speleothem record of Cheng et al., 2013 (NARC). The published age model was constructed by linearly interpolating between radiometric dates, but here, we leverage the copRa ensemble from the SISALv2 dataset.

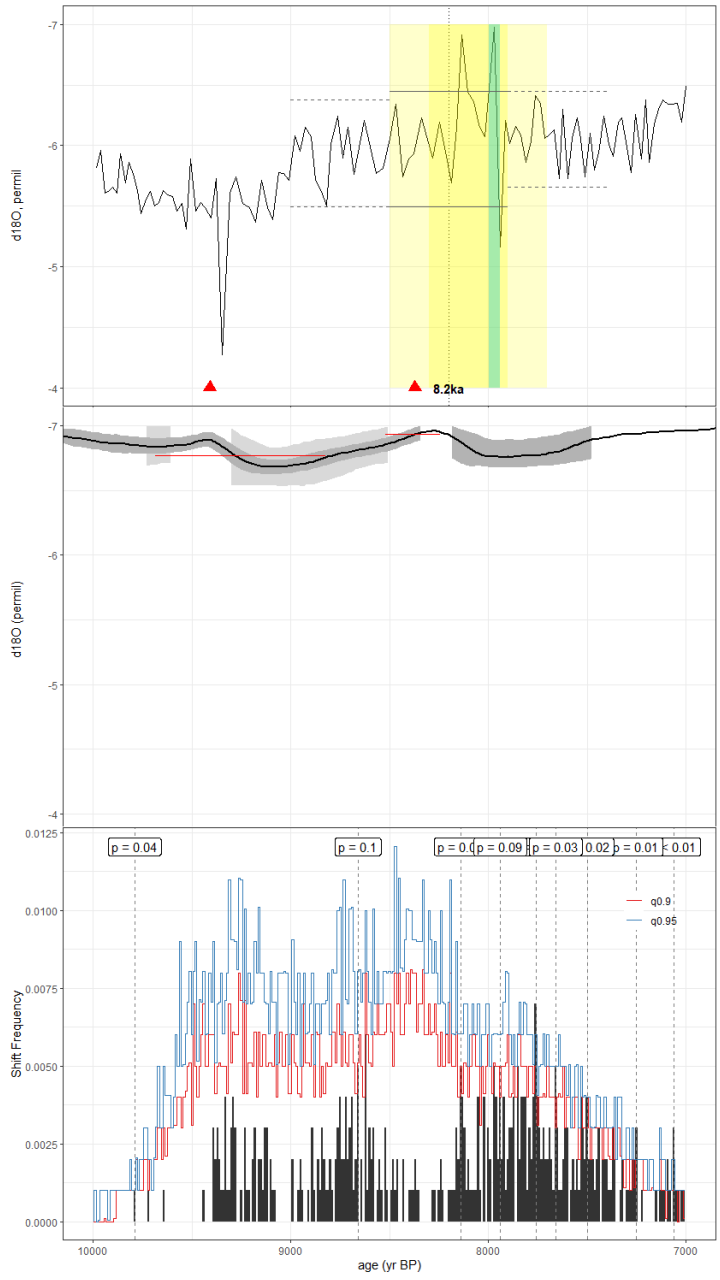

1585

Figure C51. As in Fig. C1, but for the speleothem record of van Breukelen et al., 2008 (NCB). Isoplot 3 was used to construct the published age model, however, we use the SISALv2 BACON age ensemble for our analyses.

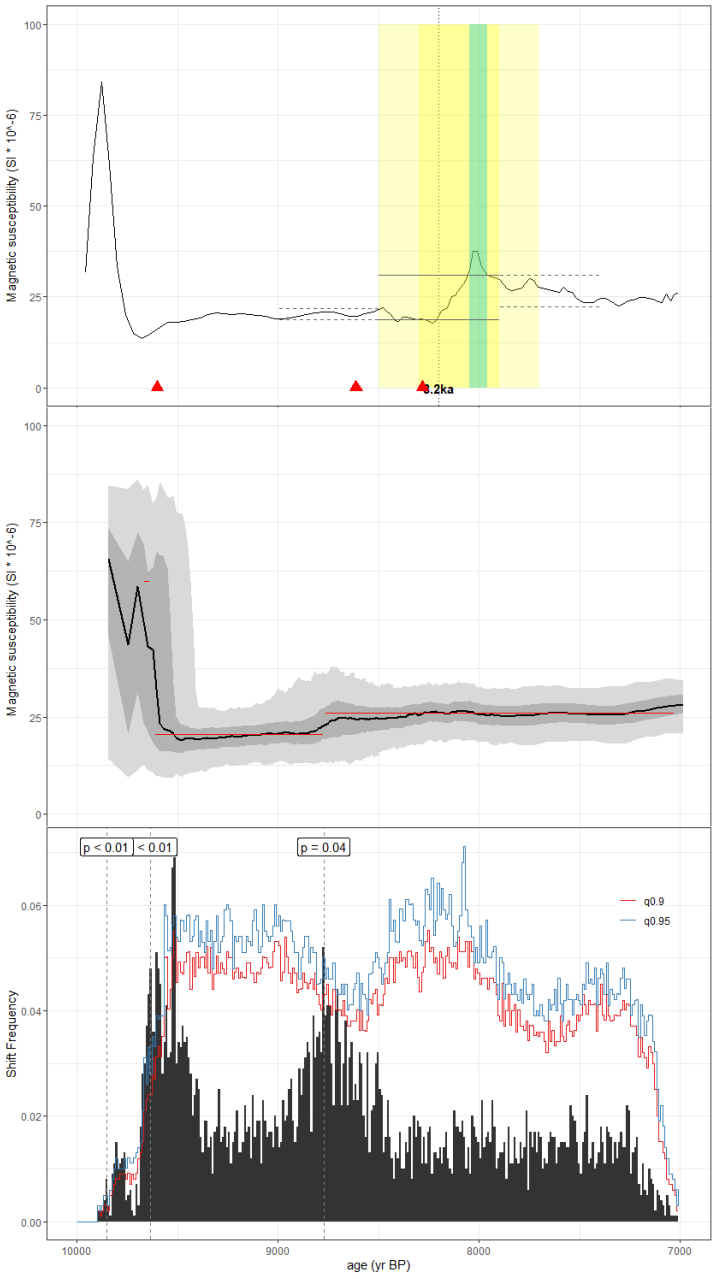

Figure C52. As in Fig. C1, but for the lake sediment magnetic susceptibility record of Escobar et al., 2012 (PET-PI6). The published age model was generated using the OxCal algorithm with IntCal09 calibration curve. Here, we show an age ensemble created using the BACON algorithm with IntCal20 calibration curve generated by geoChronR.

~~**Figure C51.** As in Fig. C1, but for the speleothem record of van Breukelen et al., 2008 (NCB). Isoplot 3 was used to construct the published age model, however, we use the SISALv2 BACON age ensemble for our analyses.~~

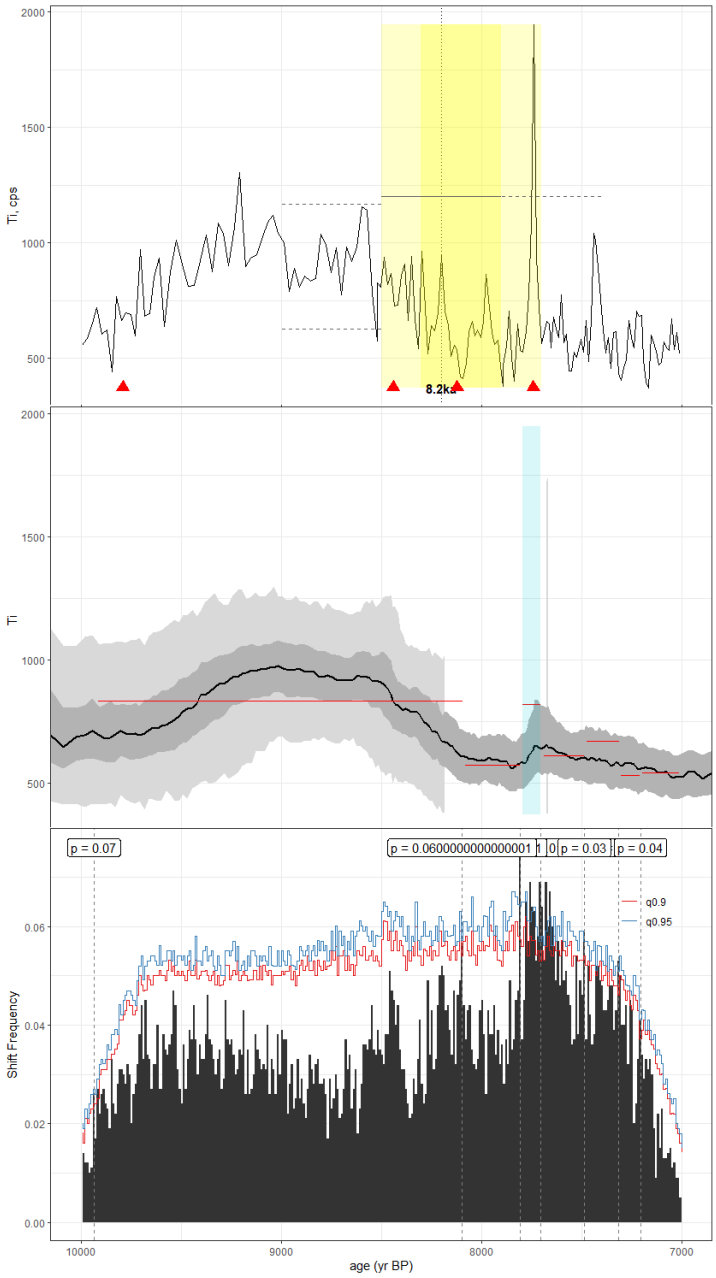

Figure C53. As in Fig. C1, but for the lake sediment titanium content record of Woods et al., 2020 (PLJJUN15). The published age model was created using the BACON algorithm with IntCal13 calibration curve. Here, we reconstruct a BACON ensemble using the IntCal20 curve in geoChronR.

Figure C52. As in Fig. C1, but for the lake sediment magnetic susceptibility record of Escobar et al., 2012 (PET-PI6). The published age model was generated using the OxCal algorithm with IntCal09 calibration curve. Here, we show an age ensemble created using the BACON algorithm with IntCal20 calibration curve generated by geoChronR.

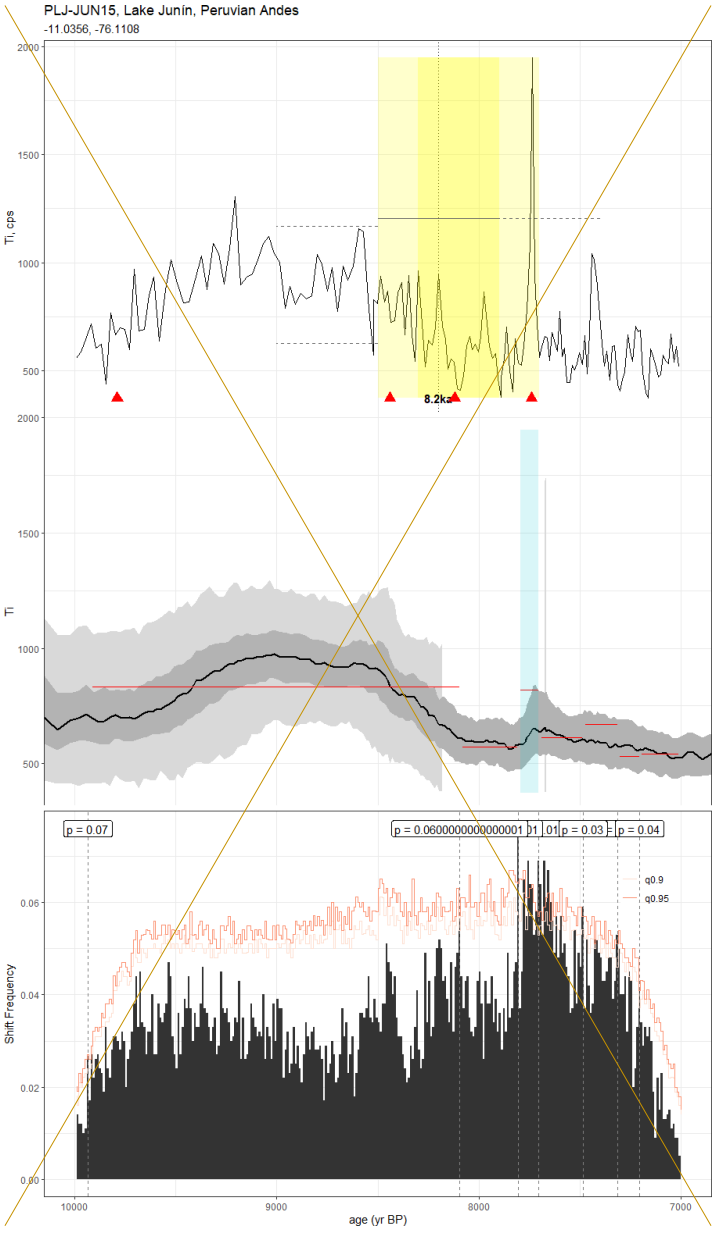

Figure C53. As in Fig. C1, but for the lake sediment titanium content record of Woods et al., 2020 (PLJJUN15). The published age model was created using the BACON algorithm with IntCal13 calibration curve. Here, we reconstruct a BACON ensemble using the IntCal20 curve in geoChronR.

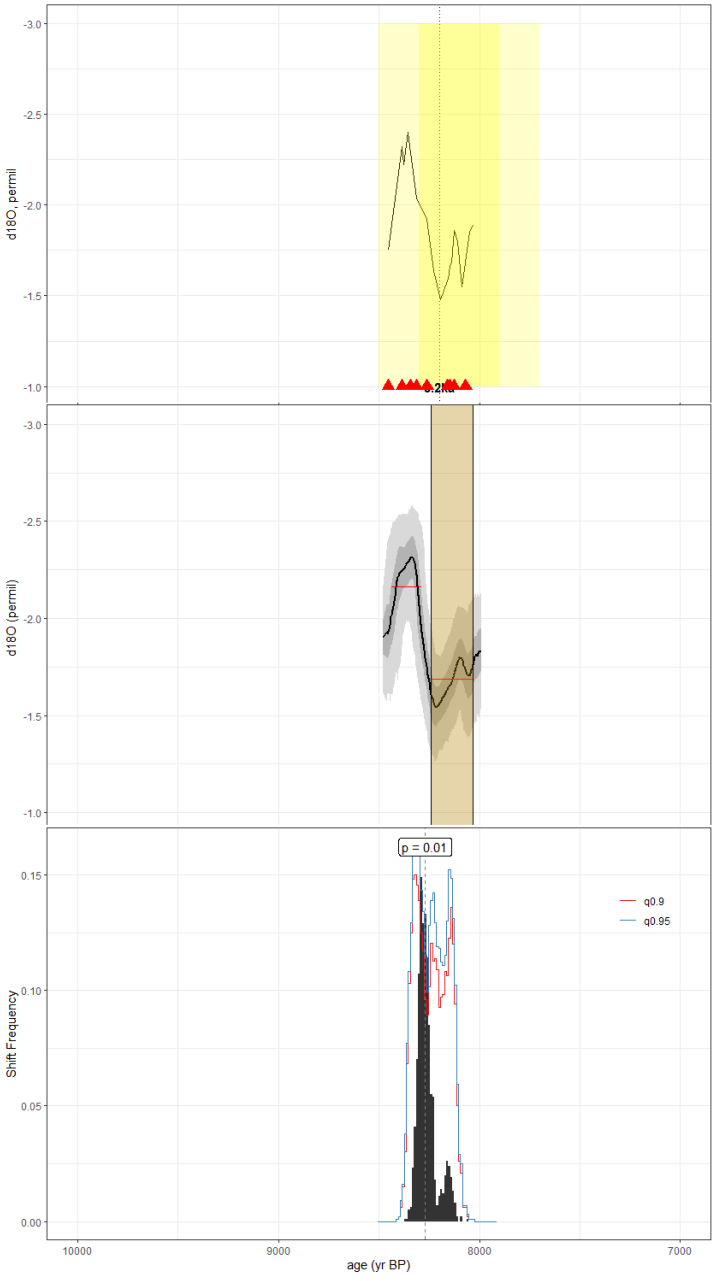

Figure C54. As in Fig. C1, but for the speleothem record of Cheng et al., 2009 (Q5Cheng). The method used in the construction of the published age model is unreported; here, we use BACON in geoChronR to generate our age ensemble.

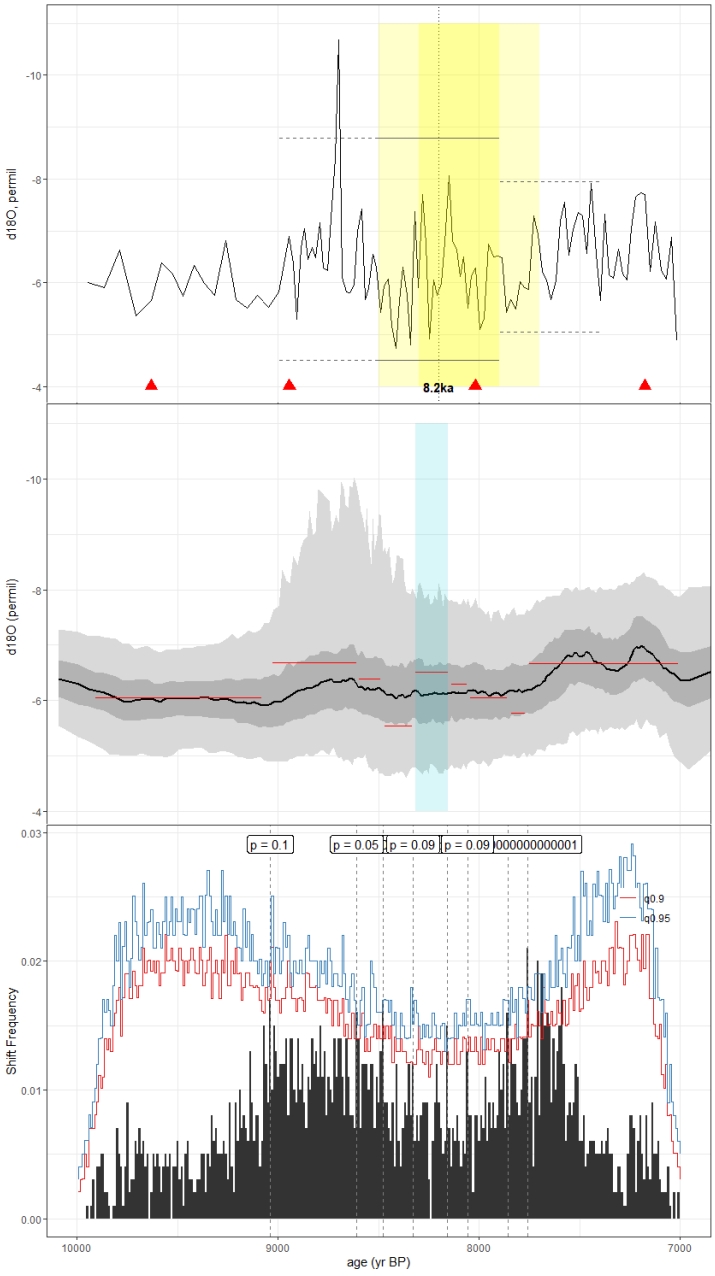

Figure C55. As in Fig. C1, but for the speleothem record of Cruz et al., 2009 (RN4). The method used in the construction of the published age model was unreported, but we leverage the Bchron ensemble supplied in version 2 of the SISAL database for our analyses.

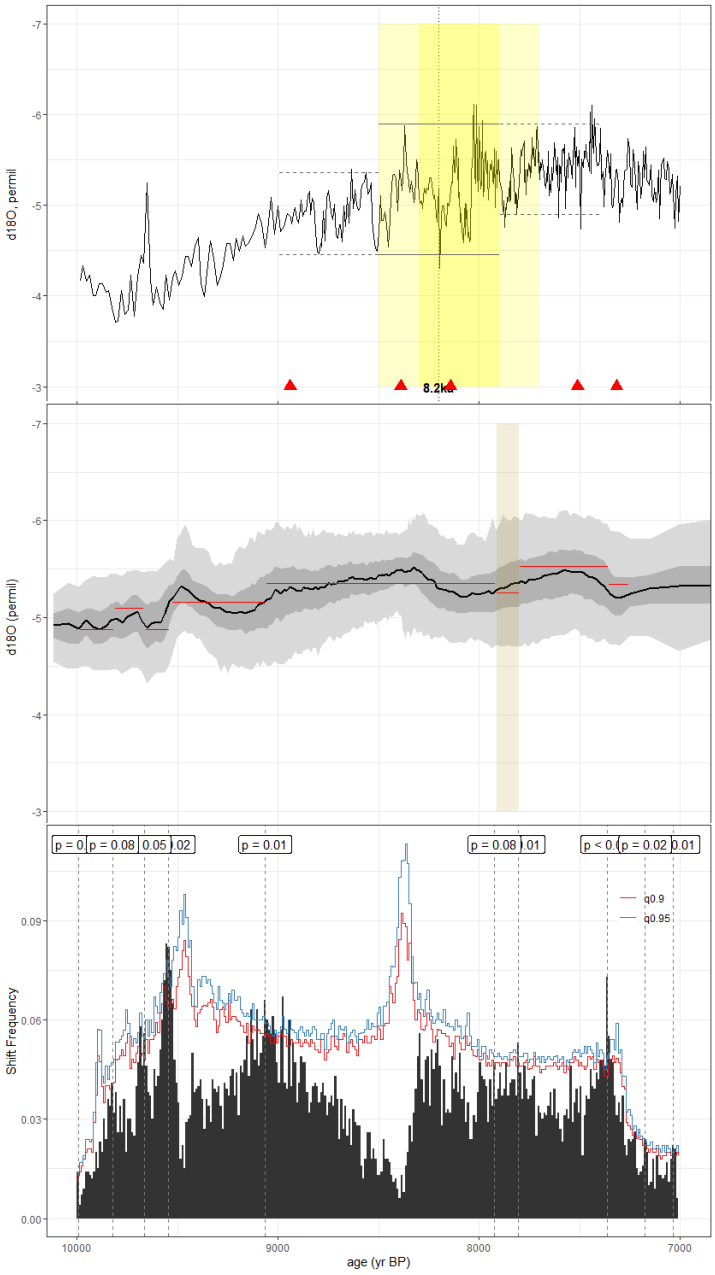

Figure C56. As in Fig. C1, but for the speleothem record of Bustamante et al., 2016 (Sha3). The published age model was developed using copRa. Here, we present the Bchron age ensemble generated for SISALv2.

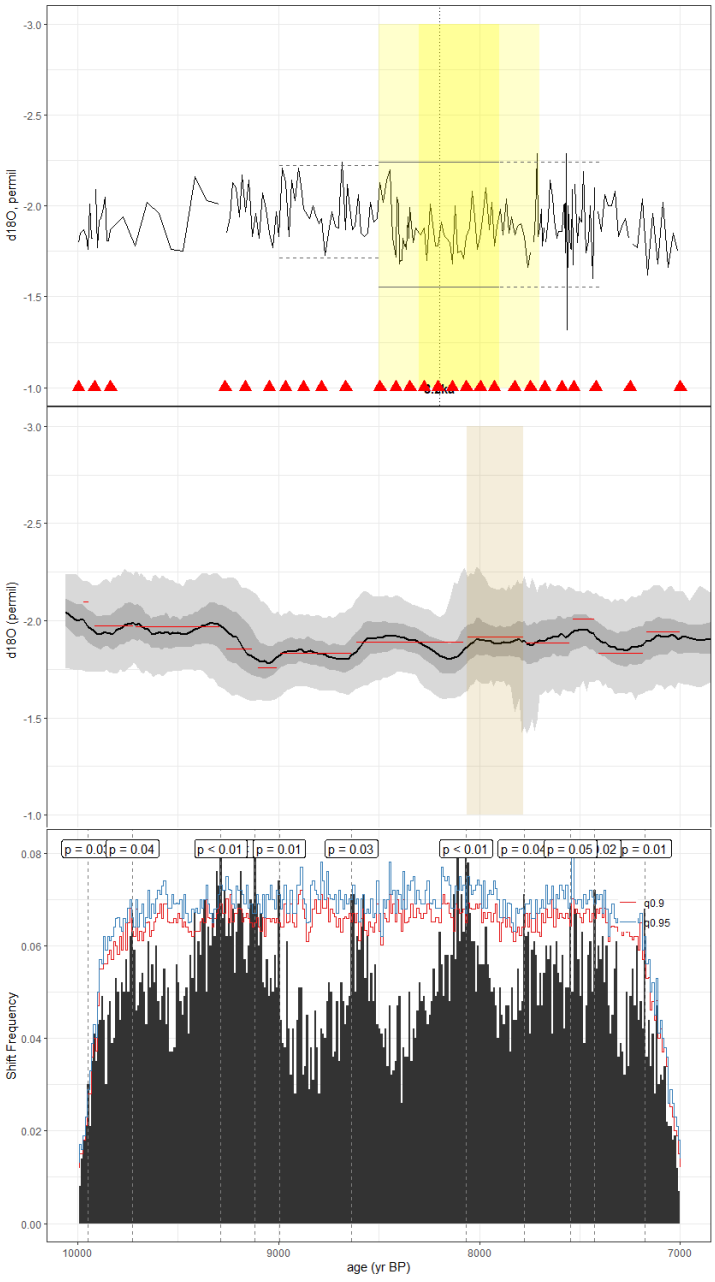

Figure C57. As in Fig. C1, but for the foraminifera record of Staubwasser et al., 2003 (Staubwasser63KA). The published age model was generated via a least-squares regression between 14C dates using the IntCal98 calibration curve. Here, we constructed our age ensemble using the BACON algorithm and IntCal20 calibration curve in geoChronR.

Figure C57. As in Fig. C1, but for the foraminifera record of Staubwasser et al., 2003 (Staubwasser63KA). The published age model was generated via a least-squares regression between 14C dates using the IntCal98 calibration curve. Here, we constructed our age ensemble using the BACON algorithm and IntCal20 calibration curve in geoChronR.

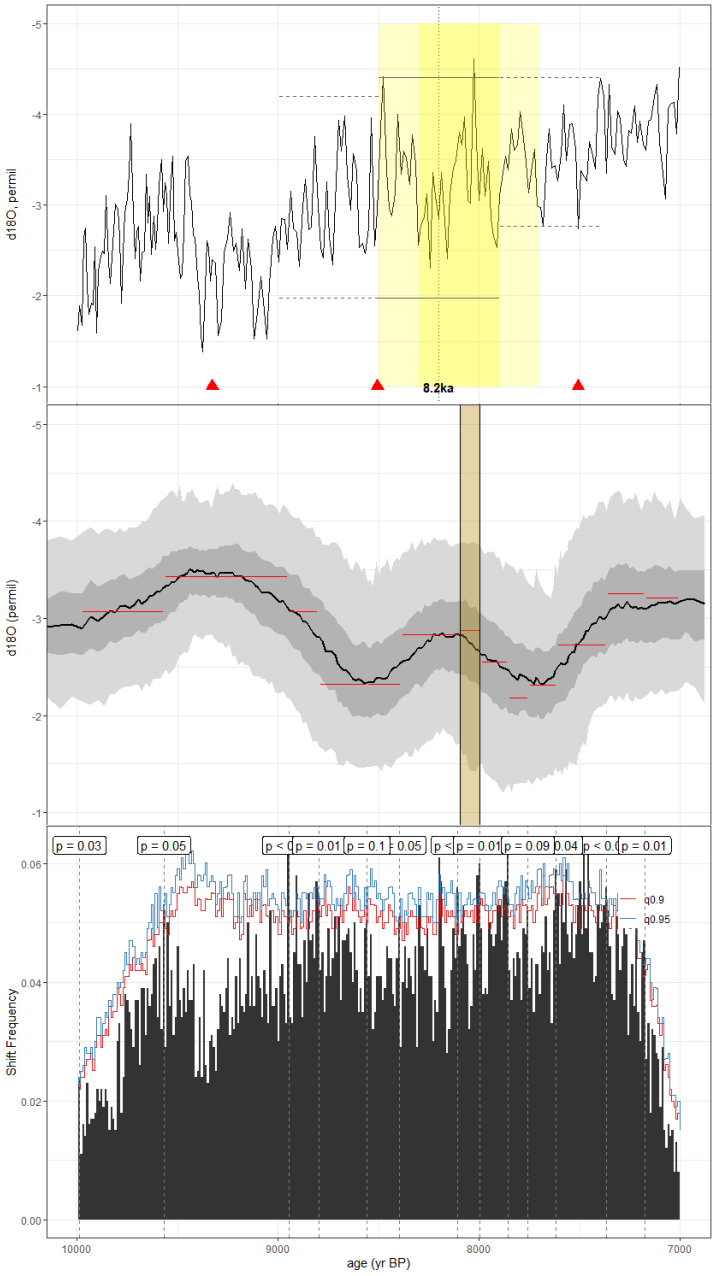

Figure C58. As in Fig. C1, but for the speleothem record of Holmgren et al., 2003 (T8). The published age model was constructed via linear interpolation between dates. Here, we construct our ensemble using the BACON age model algorithm in geoChronR.

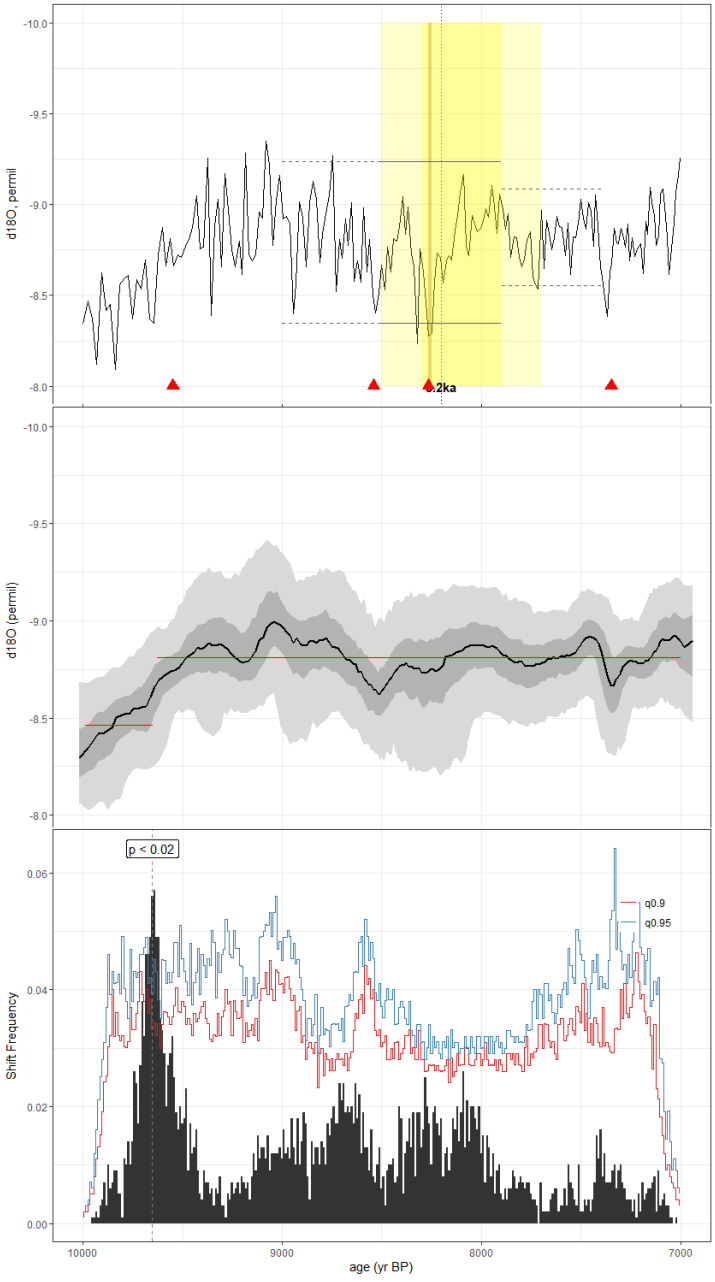

Figure C59. As in Fig. C1, but for the speleothem record of Wurtzel et al., 2018 (TA122). The published age model was constructed using the BACON algorithm. Here, we used the copRa ensemble generated for SISALv2.

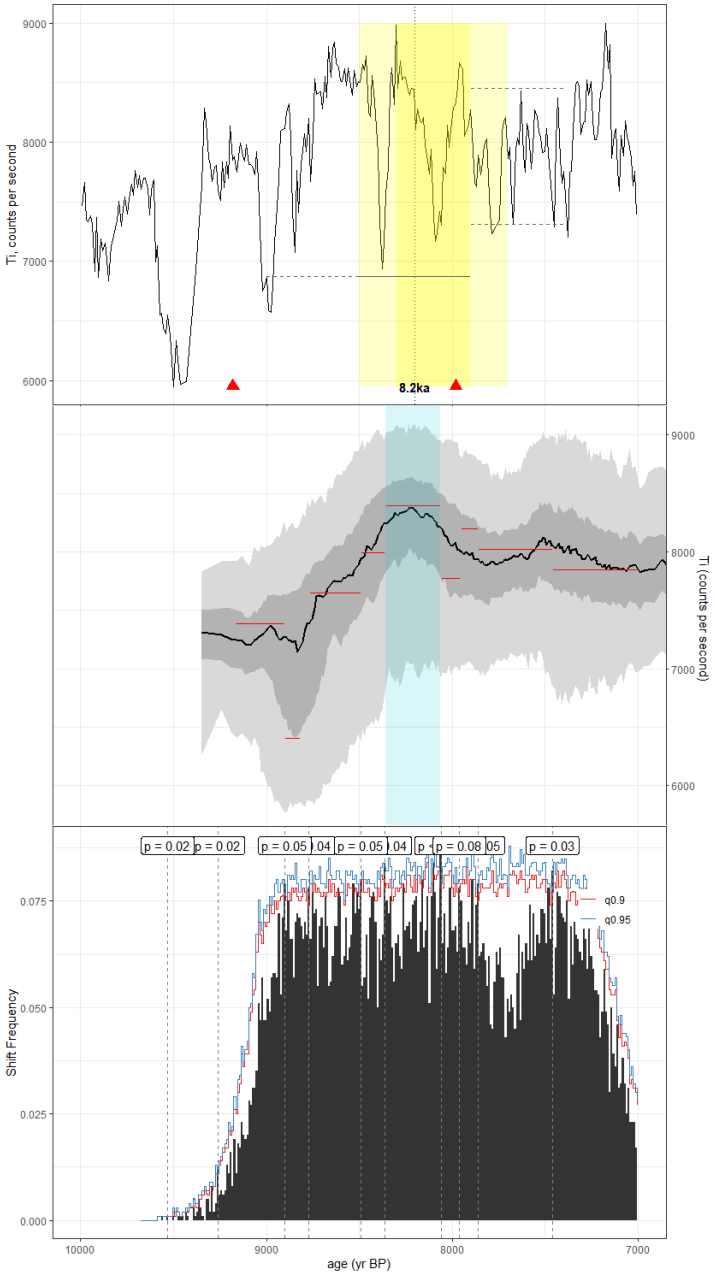

1645

Figure C60. As in Fig. C1, but for the lacustrine sediment record of Russell et al., 2014 (TOW109B). CALIB 6.0 was used to construct the published age model, though we leveraged the BACON algorithm included in geoChronR to generate our age ensemble.

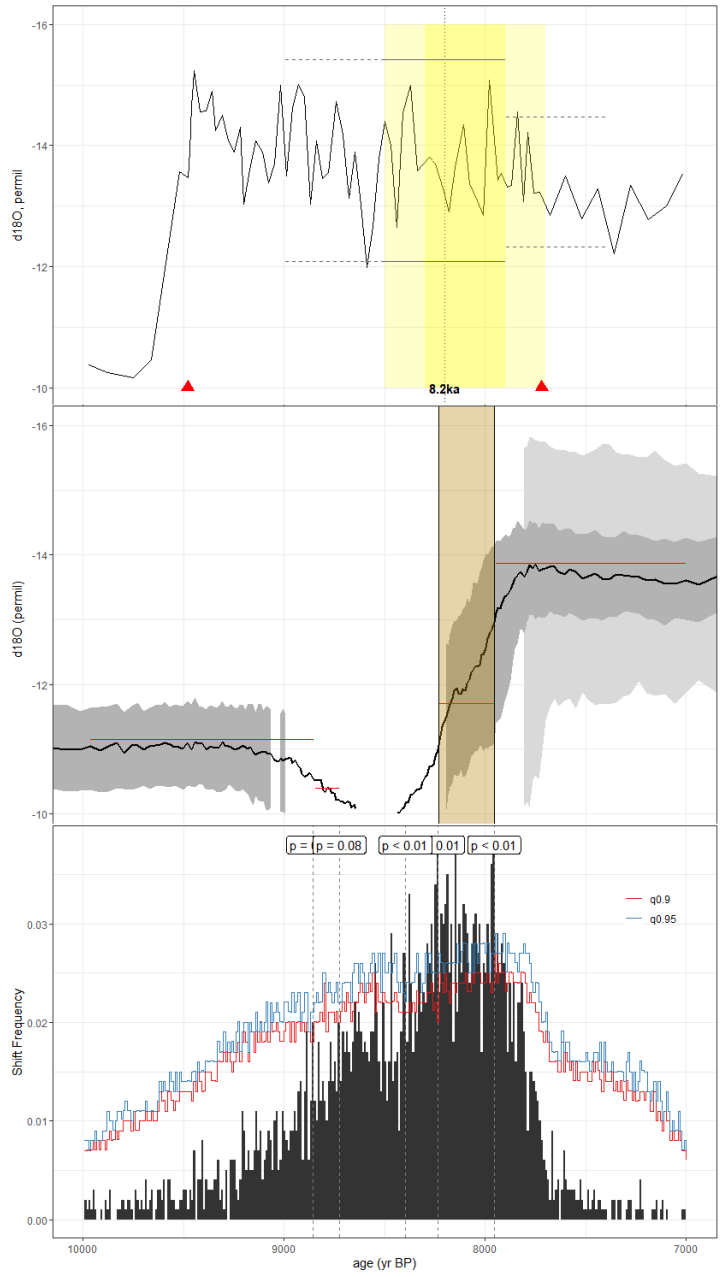

Figure C61. As in Fig. C1, but for the speleothem record of Cai et al., 2015 (XBL29). The published age model was derived from linear interpolation between radiometric dates. For our analyses, we leveraged the SISALv2 Bchron age ensemble.